Doctoral theses at NTNU, 2024:244

Stefan Weichert

Error Sources in Wave-Based Remote Sensing and Free-Surface Synthetic Schlieren

Doctoral thesis

NTNU
Norwegian University of Science and Technology
Thesis for the Degree of
Philosophiae Doctor
Faculty of Engineering
Department of Energy and Process Engineering

NTNU
Norwegian University of
Science and Technology

Stefan Weichert

Error Sources in Wave-Based Remote Sensing and Free-Surface Synthetic Schlieren

Thesis for the Degree of Philosophiae Doctor

Trondheim, June 2024

Norwegian University of Science and Technology
Faculty of Engineering
Department of Energy and Process Engineering

NTNU
Norwegian University of
Science and Technology

NTNU
Norwegian University of Science and Technology

Thesis for the Degree of Philosophiae Doctor

Faculty of Engineering
Department of Energy and Process Engineering

ISBN 978-82-326-8080-1 (printed ver.)
ISBN 978-82-326-8079-5 (electronic ver.)
ISSN 1503-8181 (printed ver.)
ISSN 2703-8084 (online ver.)

Doctoral theses at NTNU, 2024:244

Printed by NTNU Grafisk senter

Abstract

Physical processes at and under the water surface of oceans play a key role in the Earth's climate. For the models that are used to make predictions of temperature, gas contents, humidity, etc., we rely on data from laboratory experiments and field observations. This thesis presents numerical studies of error sources in two measurement techniques commonly used in the context of waves at the air-water interface. Findings include conditions under which results obtained from these methods become unreliable as well as mitigation strategies.

In laboratory studies, it is often desirable to obtain the surface topography in an area of interest. An appropriate technique in this context is the Free Surface Synthetic Schlieren (FS-SS) method. It utilizes the apparent distortions of a pattern seen through the surface due to refraction at the air-water interface, to infer the free-surface topography.

In the context of field observations of currents, remote sensing techniques are of appreciable interest due to their ability to cover large areas at low cost compared to *in-situ* methods. The second technique investigated in this work uses the wavenumber-frequency spectrum obtained from, e.g., airborne video footage, to measure Doppler shifts in the waves' frequencies due to a background current, from which the current can be inferred.

Both methods rely on certain assumptions or approximations that may not always be applicable. In order to test their limits, numerical schemes were developed that create ideal input data, which, when analyzed with the respective method, allow the isolation of error sources.

Systematic errors in the measured surface gradients obtained using the FS-SS method were investigated for two configurations. In the standard configuration, the camera is placed above the water surface and a pattern visualizing the distortions is placed underwater, typically at the bottom. In the "flipped" configuration, the camera is placed underneath the transparent water container and the pattern above the free surface. The errors found for

the standard geometry stay within a few percent for typical setups, whereas the flipped configuration shows errors that can be much larger, exceeding 50%. With proper adjustment of the setup, these can be reduced to below 10%, retaining the usability of this configuration.

For the investigation of biases in the effective Doppler shift extraction from wave elevation data, a framework was developed to generate synthetic surface wave "videos", where the background current can be both vertically and horizontally sheared. These were subsequently analyzed using the much-used Normalized Scalar Product method. The key findings of this part of the study include that both spectral leakage and horizontal shear can cause significant errors in the current measurements. Their severity was found to depend strongly on a range of parameters, most notably the wave spectrum shape in terms of angular spread and peakedness, and the current variation and direction. Knowledge of how the respective biases emerge enables the detection and mitigation of these errors, which are discussed in this thesis as well.

Preface

This thesis is submitted to the Norwegian University of Science and Technology (NTNU) for partial fulfilment of the requirements for the degree of philosophiae doctor. The doctoral work has been performed at the Department of Energy and Process Engineering (EPT) from August 2018 to March 2024. The work has been supervised by Professor Simen Å. Ellingsen and co-supervised by Professor R. Jason Hearst .

The research was funded by the Faculty of Engineering, NTNU.

The thesis consists of four chapters and three research articles. The first three chapters provide background and methodology for the articles summarized in Chapter 4 and given in full-text at the end of the thesis.

Article I

The influence of grid-generated turbulent flows on the gas transfer rate across an air-water interface
Pim Bullee, Stefan Weichert, Astri Nore, Leon Li, Simen Å. Ellingsen and R. Jason Hearst
Submitted to *Experiments in Fluids*

Contributions: P.B. and R.J.H. conceived the project. P.B., S.W. and R.J.H. designed the experimental methodology. In particular, S.W. adapted the Free Surface Synthetic Schlieren set-up for the free-surface measurements. P.B., A.N. and L.L. conducted the experiments and performed the formal analysis of bulk data. S.W. performed the formal analysis of surface elevation data. P.B., S.W., S.Å.E. and R.J.H. wrote the manuscript. S.Å.E. and R.J.H. reviewed the manuscript and provided guidance and supervision.

Article II

Biases from spectral leakage in remote sensing of near-surface currents
Stefan Weichert, Benjamin K. Smeltzer and Simen Å. Ellingsen
IEEE Transactions on Geoscience and Remote Sensing, vol. **61**, pp. 1-15, 2023, Art no. 4208515
doi: 10.1109/TGRS.2023.3321305

Contributions: S.W. and B.K.S. conceived the project. S.W. designed the methodology, conducted the numerical experiments and performed the formal data analysis. All authors contributed to writing and editing the manuscript. B.K.S. and S.Å.E. provided technical and editorial guidance. S.Å.E. supervised the project.

Article III

The effect of horizontal shear in extracting near-surface currents from wave data
Stefan Weichert, Benjamin K. Smeltzer and Simen Å. Ellingsen
Submitted to *IEEE Transactions on Geoscience and Remote Sensing*

Contributions: S.W. and B.K.S. conceived the project. S.W. designed the methodology, conducted the numerical experiments and performed the formal data analysis. S.W. and S.Å.E. wrote and edited the manuscript. B.K.S. and S.Å.E. provided technical and editorial guidance. S.Å.E. supervised the project.

Trondheim, March 2024

Stefan Weichert

Acknowledgements

The road towards a PhD is laden with obstacles and challenges. Overcoming these is a unique opportunity for growth, but the feat is one that can hardly be achieved alone. I count myself lucky to have met the right people, enabling me to cross the finishing line. To every one of these I wish to express my respect and gratitude.

First and foremost, I want to thank my supervisors. My main supervisor Simen Ellingsen supported me to a degree that I believe is above and beyond. On top of the countless discussions regarding research questions and ideas, and teaching me the tools of the trade, I knew that I could always ask for personal advice, too. I have deep respect for your dedication and I am grateful for having had the opportunity to work with you.
I want to also thank my co-supervisor Jason Hearst for all the helpful conversations and support during my PhD.

For the collaboration on the research presented in the articles in this thesis, I would like to extend my gratitude to Pim A. Bullee, Astri Nore, Leon Li and Benjamin K. Smeltzer. It has been a pleasure working with you.

My everyday student life has been colored by a myriad of smaller and larger interactions with other PhD students and postdocs in the surface flows research group that I am glad to have been a part of. Benjamin K. Smeltzer, Yan Li, Andreas H. Akselsen, Peter E. Maxwell, Jørgen R. Aarnes, Zibo Zhen, Omer M. Babiker, and Ali Semati, thank you all for the discussions, advice, lunchtime conversations, coffee breaks and evening activities.

As a PhD student, one enjoys a lot of freedom. However, it also comes with a lot of stress. I am certain that I would not have been able to withstand it without the moral support from my family in Halstenbek, my old friends in Germany, and the new friends I made here in Norway, as well as one special person that I can share this whole adventure with.

Contents

1

Introduction

More than 70% of the Earth's surface is covered by water, though the exact figure depends on whether ice and fresh water bodies are included (Kotwicki 2009). The relevance of this can hardly be overstated, as it is safe to say that all life on the planet depends on access to water, be it for intake, as a source of food, for habitation or transportation, etc. Humans and other land animals are also indirectly affected by the oceans, because the atmosphere, and hence the whole ecosystem, is strongly coupled to them. At the air-water interface, gases and heat are exchanged, and evaporation at the ocean surface is the main source of fresh water from rain.

The dynamics of the ocean and atmosphere, in terms of energy and mass flux, take place on length scales covering several magnitudes: from more than a thousand kilometers, observable from orbit, down to less than a millimeter (Taylor and Thompson 2023), requiring local measurements. On each scale one finds a variety of fascinating phenomena and processes, most of which are still the subject of ongoing research today. It is not the aim of this introduction to give a comprehensive account of the processes at all scales, the reader is instead referred to the brilliant article by Taylor and Thompson (2023) and the references found therein. On length scales ranging from tens of meters to tens of kilometers, called the submesoscale, dynamics are of particular interest due to their role in transferring energy between larger and smaller scales (McWilliams 2016), as well as the mixing

and transport in the upper ocean (e.g., Laxague et al. 2018, Thomas et al. 2008). The observation of currents at these scales is therefore a necessity for forecasts and the development of models describing the ocean-atmosphere system. Capturing the variability of near surface flows on the submesoscale is a challenge, however, as the flow structures are too small for orbital observation and too large to cover with buoys (Lund et al. 2018). One solution to this problem is to employ remote sensing techniques, such as the airborne high-resolution observation of wave-current interactions presented in VreĆica et al. (2022) and Lenain et al. (2023). Using such observations of waves enables the inference of both the depth-averaged current and the vertical current profile within the top-most layer (the depth depends on the wave spectrum present) of the ocean (e.g., Fernandez et al. 1996, Smeltzer et al. 2019, Stewart and Joy 1974). This is crucial for estimating a number of practical quantities, such as load on structures, oil film dispersion or operational safety (Lund et al. 2015).

Normally, accurate measurement of the vertical shear profile is challenging due to the motion of both the interface and the fluid below but recent developments in the inference of the current profile from wave observations allow the reconstruction of nearly arbitrary profiles (Smeltzer et al. 2019). The previously state-of-the-art method instead assumed a linear vertical profile (e.g., Fernandez et al. 1996), limiting the accuracy.

A crucial step in the development or adaptation of methods such as these requires testing in a controlled environment before they can be used for field data acquisition. For instance, profilometric techniques, able to capture the time-resolved surface topography of the air-water interface, are a suitable tool in this regard, as the so obtained surface elevation data is "clean", i.e. not influenced by lighting conditions, sun glint, white-caps, etc. The Free Surface Synthetic Schlieren method is one such candidate as shown by Smeltzer et al. (2019). Of course, to ensure that this "truth"-measurement of the surface topography is itself accurate, one has to have control over possible uncertainties and errors, as is the case with all laboratory measurements.

This work aims to contribute to the reliability of two commonly used measurement techniques by investigating sources of systematic errors; the Free Surface Synthetic Schlieren (see Section 1.1) method used in laboratory studies and a remote sensing technique for near-surface currents (see Section 1.2) used in the context of field observations.

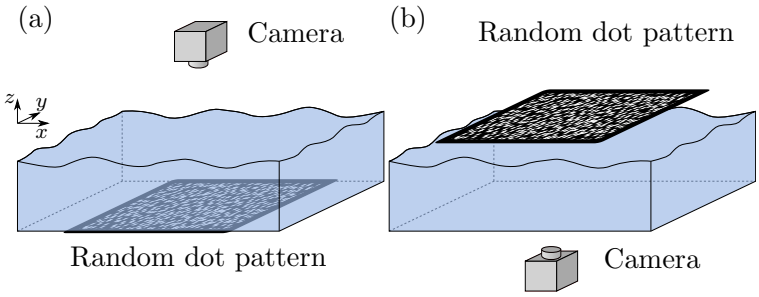

Figure 1.1: Illustration of the Free Surface Synthetic Schlieren method in configuration 1 (a) and configuration 2 (b).

1.1 Free Surface Synthetic Schlieren

When studying the interactions between turbulence, waves and currents, whether all three or in pairs, laboratory studies are a necessary part in the development of models. The parameters of interest can be controlled directly, which enables the isolation of single interactions, which is a common challenge when using field observations (e.g., Klaus and Vachon 2020).

A key element in every experiment are diagnostics that allow the distinction between different phenomena. Deformations of the water surface are typically attributed to two sources. Turbulence in the water column leads to a randomly rough surface with "wrinkles" (Savelsberg and Van de Water 2009), which are essentially advected with the mean (surface) flow, as stated by Taylor's frozen surface hypothesis. This is in contrast to what we refer to as surface waves, periodic surface deformations that can propagate on top of the advection by the current (Peregrine 1976). While this may be intuitively clear, separating waves from turbulent imprints in measurement data is a non trivial task. One way to achieve this is by analyzing the time-resolved surface topography, as the propagation of waves obeys the well-known dispersion relation for water waves (e.g., Peregrine 1976, Phillips 1980), i.e., a relation between wavelength λ and the propagation speed c_p of crests and troughs.

A commonly used method for measuring the surface topography of transparent media is the Free Surface Synthetic Schlieren (FS-SS) method due to Moisy et al. (2009). The idea behind this method is to use the refraction of light at the air-water interface. For an observer above the water surface, an object plane below will appear distorted. From the apparent shifts of points on that plane, relative to the quiescent water reference, the topography can then be inferred in principle.

A number of methods exist for obtaining the apparent displacements. The original and very common approach due to Moisy et al. (2009) is to place a random dot pattern at the bottom of the water tank, and a camera, viewing vertically downward, is placed above the free water surface and the displacements are found by using digital image correlation. Modifications include the use of a checkerboard pattern and analyzing the images using Fourier demodulation (Wildeman 2018), and using light sources of distinct wavelengths (e.g., blue and infrared) to improve the accuracy (Kolaas et al. 2018). How the surface topography can be retrieved from the apparent distortions of the dot pattern is discussed in more detail in Chapter 2. The standard setup, using a random dot pattern below, and a camera above the water surface, is depicted in Figure 1.1 (a) and is herein referred to as *configuration 1*.

The FS-SS method is very attractive due its low cost and small number of parts. In configuration 1 it has a major drawback, however. As described in Moisy et al. (2009), a combination of too strong surface deformations with a too large distance between the dot pattern and the free surface leads to the following problem: In addition to the apparent displacements, which are due to surface gradients, the pattern also appears magnified due to the curvature of the surface. Light rays originating from the camera cross at some distance below the surface. When this distance is smaller than (or close to) the distance between the water surface and the dot pattern, individual dots appear as streaks from which displacements cannot be obtained (see, e.g., Steinmann et al. 2018); this is illustrated in Figure 1.2. A solution to this issue is provided in Moisy et al. (2009). Instead of configuration 1, the setup can be inverted so that the camera is below the transparent bottom of the water tank and the dot pattern held above the free surface, allowing for an arbitrary pattern-surface distance; this is herein referred to as *configuration 2* and has been used in, e.g., Moisy et al. (2012). The relations connecting the surface topography to the pattern distortions in the paraxial approximation (effectively infinite surface-camera distance) can be found for both configuration 1 (Moisy et al. 2009) and configuration 2 (Moisy et al. 2012). However, for a finite (but large) surface-camera distance these are only given for configuration 1 and deriving the corresponding equations for configuration 2 is not as straight forward as the simple change in setup suggests (see Chapter 2 for details).

1.1.1 Goal

The Free Surface Synthetic Schlieren method is a powerful tool for obtaining the surface topography of transparent fluids. For applications in exper-

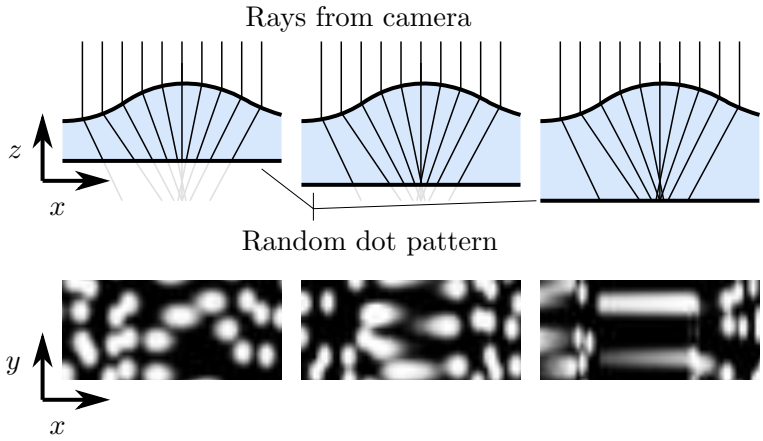

Figure 1.2: Illustration of the distortions of a dot pattern as seen by the camera. The surface distance is increased left to right, leading to rays originating at the camera to cross above the pattern, and thus to dots appearing as streaks. The surface cannot be reconstructed.

iments with relatively deep water, such as the large water channel at the fluid mechanics laboratory at NTNU (Jooss et al. 2021), its application is limited by caustics due to a too large pattern-surface distance. Moving the pattern closer to the surface obstructs the flow and is therefore not practical. A flipped geometry, with the camera below the transparent bottom of the water tank and the dot pattern above the free surface is more flexible in this regard. However, the equations for obtaining the surface topography from observed distortions in this configuration are only available in the parallax approximation. The errors introduced due to a finite distance between the camera and the free surface are unknown.

The first part of this work, therefore, is the derivation of said equations, as well as an analysis of the systematic errors introduced by approximations made in the derivation, both for configuration 1 and configuration 2. The error analysis is limited to parameter ranges (e.g., water depth, camera-surface distance, etc.) relevant for the large water channel mentioned above. An overview of the parameters is given in Table 2.1 in Chapter 2.

1.2 Remote Sensing and Shear

Knowledge of currents in oceans, rivers, and estuaries is of great scientific and practical importance. Various techniques for their measurement have been developed to this day, including subsurface drifters, acoustic Doppler profilers and stationary propellers, to name just a few. It is not the attempt

of the author to give a comprehensive overview over these methods and the reader is referred to Joseph (2013) instead.

They can be roughly divided into *in-situ* and *remote* techniques. In-situ measurements, though an invaluable tool, have a major drawback, in that they provide point measurements of the current, either stationary or along the trajectory of a vessel. Obtaining information about the current in a larger area is, thus, a costly and time-consuming endeavor. This problem is exacerbated further when the depth profile of the current is of interest as well.

Remote sensing techniques are able to collect information from large areas and within time frames much shorter than the time scale over which these currents vary (e.g., Lenain et al. 2023), which is crucial if the dynamics themselves are of interest. Many of these are based on the fact that the propagation of waves is influenced by the background current. The angular frequency ω and wavelength λ of a small amplitude plane wave are connected via the famous dispersion relation (DR) found in many textbooks (e.g., Peregrine 1976)

$$\omega_{\mathrm{DR},0}(k)^2 = \left(gk + \frac{\tau}{\rho}k^3\right)\tanh kh, \tag{1.1}$$

where $k = 2\pi/\lambda$ is the wavenumber or spatial frequency, g is the gravitational acceleration, τ the surface tension, ρ the fluid density, and h the water depth. When surface tension effects are neglected, and the water depth is sufficiently large, so that $\tanh(kh) \approx 1$, this becomes the simple relation, $\omega_{\mathrm{DR},0} = \sqrt{gk}$. Within this work, surface tension and finite water depth effects are neglected.

In the presence of a constant background current described by the two-dimensional vector $\mathbf{U}$, one obtains an additional term (Peregrine 1976)

$$\omega_{\mathrm{DR}} = \omega_{\mathrm{DR},0}(k) + \mathbf{U}\cdot\mathbf{k}, \tag{1.2}$$

where $\mathbf{k}$ is the wavevector in the (horizontal) x–y–plane and $k = |\mathbf{k}| = 2\pi/\lambda$. Figure 1.3 depicts the dispersion relation "cone" with and without a current. The current-induced change in frequency in Equation (1.2) depends both on the magnitude and direction of the wavevector $\mathbf{k}$. In principle, the measurement of the frequency (or phase velocity) at two non-parallel wavevectors is sufficient for the inference of $\mathbf{U}$ (see, e.g., Dugan and Piotrowski 2003, Hessner et al. 2014, Streßer et al. 2017, Young and Rosenthal 1985).

The task of inferring the background current becomes more complicated, however, when it is vertically sheared, i.e., when the current changes with

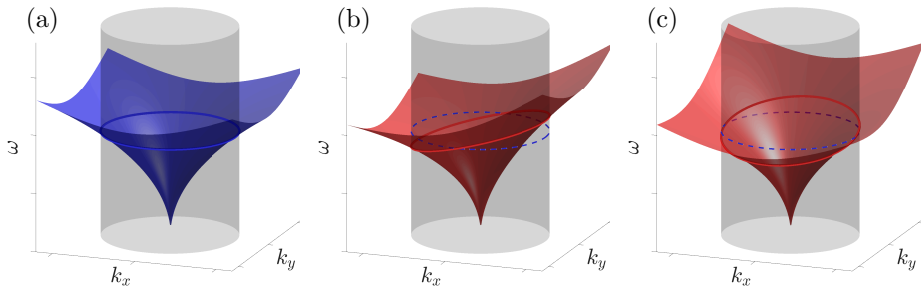

Figure 1.3: Dispersion cones without (a), and with a current $\mathbf{U} = (U, 0)$ (b) and $\mathbf{U} = (0, U)$ (c). The intersection with a cylinder surface is highlighted. The dashed line corresponds to the intersection for $U = 0$.

depth, $\mathbf{U} = \mathbf{U}(z)$, as depicted in Figure 1.4(a). The most common modification for the dispersion relation in Equation (1.2) that accounts for depth-dependent currents was derived in Stewart and Joy (1974), yielding the approximation for mild vertical shear in deep water[1]

$$\omega_{\mathrm{DR}} = \omega_{\mathrm{DR},0}(k) + \tilde{\mathbf{c}}(k) \cdot \mathbf{k}, \quad \text{with} \quad \tilde{\mathbf{c}} = 2k \int_{-\infty}^{0} \mathbf{U}(z) e^{2kz} \mathrm{d}z. \tag{1.3}$$

In the place of $\mathbf{U}$ now stands the more general, k–dependent $\tilde{\mathbf{c}}$, typically called Doppler shift velocity (DSV). An intuitive explanation for its k–dependence can be gained from the fact that, under a wave, the amplitude of the circular motion of fluid particles due to the wave decays exponentially with depth $\propto e^{kz}$. This is illustrated in Figure 1.4(b, c). It is intuitive that, at depths where the fluid motion due to waves is negligible, the influence of a background current on the surface wave can be expected to vanish as well. In other words, the waves "feel" currents only down to a certain depth. A rough estimate can be gained by considering the weighting factor of the integrand in Equation (1.3), e^{2kz}. For instance, one may set a threshold at $e^{2kz} < 1\%$ which corresponds to a depth of $z \approx \frac{1}{2}\lambda$.

It is therefore possible to infer the depth profile of a background current from the measurement of the wave dispersion relation by inverting Equation (1.3). This highly attractive principle has since been utilized to extract the vertical shear from field data obtained using HF radar (e.g., Fernandez et al. 1996, Stewart and Joy 1974) X-band radar (e.g., Lund et al. 2015) and optical methods (e.g., Lenain et al. 2023).

Typically, obtaining the vertical shear profile is a two-step process, con-

[1] An extension to finite water depth is available as well (Kirby and Chen 1989)

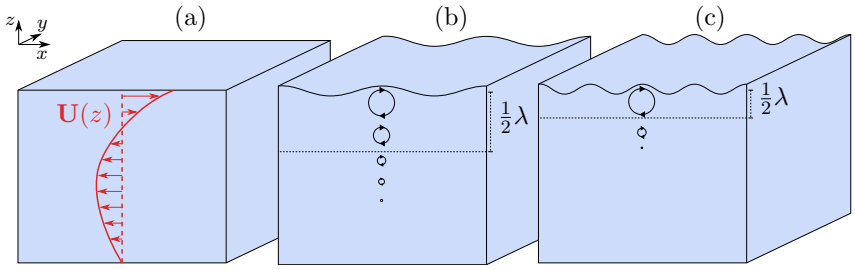

Figure 1.4: Depiction of a vertically varying current profile (a) and the circular fluid particle motion (b,c) for waves of different wavelength λ. Waves "feel" the current only in the top layer depending on λ.

sisting of the measurement of the DSVs $\tilde{\mathbf{c}}$ and subsequently inverting the integral in Equation (1.3) for $\mathbf{U}$, given $\tilde{\mathbf{c}}(k)$. The inference of the vertical velocity profile from the measured DSVs is a non-trivial task and an ongoing field of research (e.g., Campana et al. 2016, Lund et al. 2015, Smeltzer et al. 2019). This thesis focuses on the first part of the analysis step, i.e., the measurement of the DSVs $\tilde{\mathbf{c}}$ from wavevector-frequency spectra obtained from spatio-temporal surface data.

A variety of techniques have been employed to date to measure DSVs. Common are least-squares based methods (e.g., Gangeskar 2018, Senet et al. 2001, Young and Rosenthal 1985), the Polar current shell method (e.g., Huang et al. 2016) and Normalized Scalar Product (NSP) based methods (e.g., Huang and Gill 2012, Huang et al. 2016, Lenain et al. 2023, Serafino et al. 2010). Since the performance of these is comparable (Huang et al. 2016), and the NSP has seen recent use, the analysis in this thesis is restricted to the NSP method.

Refraction of waves due to a varying current is a well-studied phenomenon. The wavevector and frequency of an incident wave undergo changes as the wave propagates across regions with horizontal shear and temporal variation, respectively (e.g., Peregrine 1976). Spectral methods for measuring DSVs, such as the ones mentioned above, utilize wave-observations from areas of finite size and with finite duration. Of particular interest is the observation of near-surface currents and waves in regions where the current varies horizontally, e.g. near submesoscale fronts (VreĆica et al. 2022). To the knowledge of the author, all methods mentioned above rely on the (mostly implicit) assumption that the obtained DSVs reflect averages (spatial and temporal) of the underlying current. Though intuitive, it is not necessarily true, as this thesis aims to show. Biases in these methods, especially when they depend on factors that cannot be controlled during the

measurement (weather, wave spectrum, etc.), could call their dependability into question. Hence, the errors sources must be well understood and mitigating precautions should be taken where possible.

1.2.1 Goal

Remote measurement techniques for ocean currents have seen broad use in the past 50 years and as methods become more sophisticated and precise, the importance of control over systematic error sources grows.

The aim of the second part of this work, therefore, is to investigate systematic errors, or biases, in the DSV extraction via the commonly used NSP method. A major goal herein is to scrutinize the validity of the assumption that, in the presence of horizontal shear, DSV extraction returns the domain average of the background current. For this, a numerical framework is developed capable of generating synthetic surface elevation data of waves propagating atop horizontally and vertically sheared currents. The choice of scenarios is made such that different error sources can be identified and the effects of horizontal shear isolated, within realistic ranges for parameters such as spectral shape, shear strength, domain size, etc.

1.3 Thesis Outline

The topics of Free Surface Synthetic Schlieren and remote sensing introduced in Chapter 1 are somewhat distinct. Therefore, each topic is given a separate chapter, Chapter 2 and Chapter 3, respectively, wherein more detailed background, theory and methodology are discussed. The relevant research articles are summarized in Chapter 4 before concluding with a future outlook.

2

The Free Surface Synthetic Schlieren Method on its Head

The Free Surface Synthetic Schlieren (FS-SS) method is based on a simple principle. Due to refraction at an interface between two media of different refractive index n, objects behind the interface appear displaced and this displacement depends on the topography $h(x, y)$ of the interface. This is depicted in Figure 2.1 (a) for configuration 1.

Consider first a flat interface, i.e., h is constant. Light originating from an object point M in the $z = 0$ plane reaches the observer C at along a path that is affected by refraction (red line). For the observer M appears to be at the location M'. When the surface is deformed due to, e.g., waves, the surface normal vector $\hat{\mathbf{n}}$ has horizontal components determined by the surface gradient $\boldsymbol{\nabla} h$, which leads to a change of refraction angles (blue line). The point M then appears to be at a location M'' different from M'.

From the difference between M' and M'', i.e., the displacement vector $\overline{\mathsf{M'M''}}$, the surface gradient $\boldsymbol{\nabla} h$ can in principle be inferred. An approximate, linear relation between $\overline{\mathsf{M'M''}}$ and $\boldsymbol{\nabla} h$ at the point I was derived in Moisy et al. (2009).

This chapter begins with a brief review of the theory and key findings from Moisy et al. (2009). Then, an analogous equation for configuration 2, de-

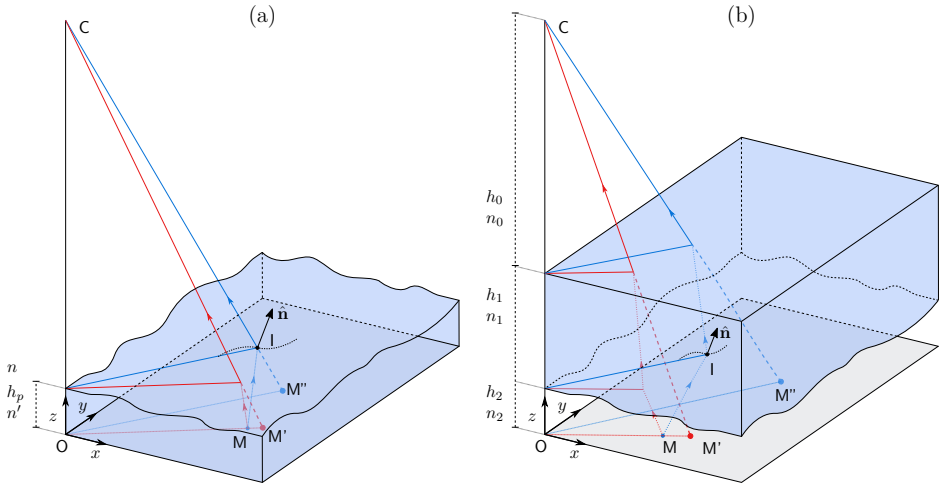

Figure 2.1: Illustration of the principle behind the Free Surface Synthetic Schlieren method for configuration 1 (a) and configuration 2 (b). Light from an object point M reaches the camera C along rays indicated by arrows. When the interface is flat, the red path is followed, leading to an image point appearing at M'. When the interface is deformed, indicated by the surface normal vector $\hat{\mathbf{n}}$ at I, the ray takes a different path, marked in blue, giving rise to the image point M". Thus, the vector $\overline{\mathbf{M'M"}}$ can be used to infer the surface normal vector and gradient.

picted in Figure 2.1 (b), is derived. This configuration differs from the first configuration in having an additional interface, i.e., change of refractive index, between the free surface of interest ($z = h$) and the camera C. The setup is in general described by the distances between the camera and the water bottom h_0, the water depth h_1, and the camera-surface distance h_2, together with the respective refractive indices n_0, n_1 and n_2, determined by the transparent materials, typically air, water, and air.

The second part of this chapter is an investigation of systematic errors emerging under certain circumstances, detailed in Section 2.2. This analysis is restricted to parameters typical for the large water channel at the fluid mechanics laboratory at NTNU (see Jooss et al. 2021) and Table 2.1 for details).

Note, that the analysis presented here deals only with the inference of the surface gradient $\boldsymbol{\nabla} h$ from measured displacements $\overline{\mathbf{M'M"}}$. For obtaining the displacements themselves, one can use, e.g., a Particle Image Velocimetry (PIV) procedure (see Moisy et al. 2009) using a random dot pattern at $z = 0$ for making the displacements measurable.

The contents of this chapter are relevant for the free surface analysis presen-

ted in *Article I*. Measurements therein were taken using the FS-SS method in configuration 2.

2.1 Theory

There are three key assumptions that the derivations given herein and in Moisy et al. (2009) are based on:

1. Surface deformations are small with respect to the distance between the surface and the dot pattern. Points on the surface are well approximated by setting their vertical coordinate to the pattern-surface distance h_p (configuration 1) or h_2 (configuration 2).
2. The surface steepness (or slope) is small, i.e., $\varepsilon = |\boldsymbol{\nabla} h| \ll 1$.
3. The camera pattern distance H is much larger than the dimension L of the observed square domain, so that $H \gg L\sqrt{2}/2$. View angles can therefore be assumed to be small.

2.1.1 Refraction

When a ray of light crosses the interface between two homogeneous media, labelled 1 and 2 it gets refracted, i.e., the transmitted ray propagates in a different direction than the incoming ray. This can be quantified by the well-known Snell-Descartes law

$$n_1 \sin \alpha_1 = n_2 \sin \alpha_2 \tag{2.1}$$

where α_1 and α_2 are the angles between the ray and the surface normal at the point of intersection on the respective sides of the interface. Accordingly, n_1 and n_2 are the refractive indices of the two materials. In general, the refractive index is a function of the light's wavelength, but within the visible range of about 400 to 800 nm, the effect is assumed negligible. The refractive index of water, for instance, varies between 1.34 and 1.33 (Hale and Querry 1973).

For the following, it is necessary to use a vectorial form of the Snell-Descartes law. Let the incoming and outgoing ray be denoted by the unit vectors $\hat{\mathbf{r}}_1$ and $\hat{\mathbf{r}}_2$ and the unit surface normal vector $\hat{\mathbf{n}}$. The equivalent of Equation (2.1) can be found in many basic optics text books, e.g., in Goodman (2010),

$$n_1(\hat{\mathbf{n}} \times \hat{\mathbf{r}}_1) = n_2(\hat{\mathbf{n}} \times \hat{\mathbf{r}}_2). \tag{2.2}$$

An explicit equation for $\hat{\mathbf{r}}_2 = \hat{\mathbf{r}}_2(\hat{\mathbf{r}}_1, \hat{\mathbf{n}}, n_1, n_2)$ can be obtained, but in the derivations found in the literature a crucial choice of sign is often left out. A sketch of a derivation is repeated here in order to avoid the ambiguity.

The special cases of $n_1 = n_2$ and $\hat{\mathbf{r}}_1 \parallel \hat{\mathbf{n}}$ are trivial, and therefore excluded. Since $\hat{\mathbf{n}}$, $\hat{\mathbf{r}}_1$ and $\hat{\mathbf{r}}_2$ lie within the same plane, $\hat{\mathbf{r}}_2$ can be constructed by linear combination

$$\hat{\mathbf{r}}_2 = a\hat{\mathbf{r}}_1 - b\hat{\mathbf{n}} \quad \text{with} \quad a, b \in \mathbb{R}. \tag{2.3}$$

From Equation (2.2) one obtains $a = n_1/n_2$. The constant b can then be determined from the requirement that $\hat{\mathbf{r}}_2$ be of unit length. One finds

$$b = a(\hat{\mathbf{n}} \cdot \hat{\mathbf{r}}_1) \pm \sqrt{1 - a^2(1 - (\hat{\mathbf{n}} \cdot \hat{\mathbf{r}}_1)^2)} \tag{2.4}$$

The choice of the sign of the root depends on whether $\hat{\mathbf{n}}$ points towards $\hat{\mathbf{r}}_1$, i.e., the sign of the scalar product $(\hat{\mathbf{n}} \cdot \hat{\mathbf{r}}_1)$. This can be seen by requiring that, in the limit of identical materials $a \to 1$, no refraction should occur, i.e., $\hat{\mathbf{r}}_2 \to \hat{\mathbf{r}}_1$. An unambiguous expression for b then is

$$b = a\,\hat{\mathbf{n}} \cdot \hat{\mathbf{r}}_1 - \operatorname{sign}(\hat{\mathbf{n}} \cdot \hat{\mathbf{r}}_1)\sqrt{1 - a^2(1 - (\hat{\mathbf{n}} \cdot \hat{\mathbf{r}}_1)^2)}. \tag{2.5}$$

Thus, Equation (2.3) becomes

$$\hat{\mathbf{r}}_2 = \frac{n_1}{n_2}\hat{\mathbf{r}}_1 - \hat{\mathbf{n}}\left[\frac{n_1}{n_2}\hat{\mathbf{n}} \cdot \hat{\mathbf{r}}_1 - \operatorname{sign}(\hat{\mathbf{n}} \cdot \hat{\mathbf{r}}_1)\sqrt{1 - \left(\frac{n_1}{n_2}\right)^2(1 - (\hat{\mathbf{n}} \cdot \hat{\mathbf{r}}_1)^2)}\right]. \tag{2.6}$$

2.1.2 Review of Configuration 1

Figure 1.1 (a) shows the setup for configuration 1, where the camera is located above the free surface and a random dot pattern is placed below.

Let the origin O of the coordinate system lie on the pattern and the z-axis be perpendicular to it. A camera, or observer, is located on the z-axis at $z = H$, denoted by the point C. The free surface is described by $z = h(x, y)$, where h_p denotes the surface location in the absence of deformations, i.e., h_p is the average distance between the dot pattern and the free surface.

Conventionally, the refractive indices above and below the free surface are n $(z > h)$ and n' $(z < h)$, respectively. It is useful to collect these in the material constant $\alpha = 1 - n/n'$.

Under the assumptions mentioned above, Moisy et al. (2009) use this setup to derive an approximate equation linking the apparent displacement $\delta\mathbf{x} = \overline{\mathbf{M'M''}}$ of points on the dot pattern to the surface gradient $\boldsymbol{\nabla} h$ causing it. Using slightly different notation, the result is

$$\boldsymbol{\nabla} h \approx -\frac{\delta\mathbf{x}}{h_M^*}, \quad \text{where} \quad \frac{1}{h_M^*} = \frac{1}{\alpha h_p} - \frac{1}{H}. \tag{2.7}$$

Note, that a subscript M has been added to h^* to clearly differentiate this result from the following derivation for configuration 2.

An additional step for obtaining the gradient field is then required, which corrects for parallax errors due to a finite camera-pattern distance H. This step attributes each $\boldsymbol{\nabla} h$ obtained through Equation (2.7) to their respective horizontal coordinate $\mathbf{x} = (x, y)$, i.e., the point I, through the exact relation

$$\mathbf{x} = \left(1 - \frac{h_p}{H}\right) \overline{\mathsf{OM''}}. \tag{2.8}$$

In their work, Moisy et al. (2009) also describe how the surface topography $h(x, y)$ is calculated from $\boldsymbol{\nabla} h(x, y)$, but as this is independent of the setup configuration, it is not discussed here.

2.1.3 Derivation for Configuration 2

Setup and Notation

The setup for the FS-SS method in configuration 2 is depicted in Figure 1.1 (b). It is practical to return to a coordinate system like that for configuration 1, as shown in Figure 2.1 (b), with gravity acting along the positive z-direction.

As in configuration 1, let H be the total distance from the camera to the random dot pattern. This distance is now divided into the pattern-surface distance $h_p \equiv h_2$, the water depth h_1 and the distance between the camera and the bottom of the tank h_0. In the experimental setup, for which this derivation is dedicated, there is air above and below the water. It is useful, however, to let the refractive indices of the three sections be arbitrary. From $z = H$ to $z = 0$, let them be denoted by n_0, n_1 and n_2.

Procedure

The derivation of Equation (2.7) given in Moisy et al. (2009), makes use of a plane containing the points M, $\mathsf{M''}$, I and C. Within this plane, the Snell-Descartes law in the form of Equation (2.1) can be applied directly, as it contains the surface normal vector $\hat{\mathbf{n}}$. Such a plane cannot, however, be constructed in configuration 2 because of the additional refraction of light rays at the interface at $z = H - h_0$.

Hence, a different approach is chosen[2]. The idea is to find the position of M, denoted in the following by $\mathbf{x}_0$, as a function of the virtual point $\mathsf{M''}$,

[2] An additional reason is, that the later conducted error analysis made the forward

specifically, the azimuth β_0 and polar angle ϕ_0 under which the camera sees it. To this end the direction of the ray, originating from the camera within each material (see Figure 2.2) is calculated. This exact relation can then be approximated to find an analytical expression for the inverse relation. A similar procedure is applied to the point M'.

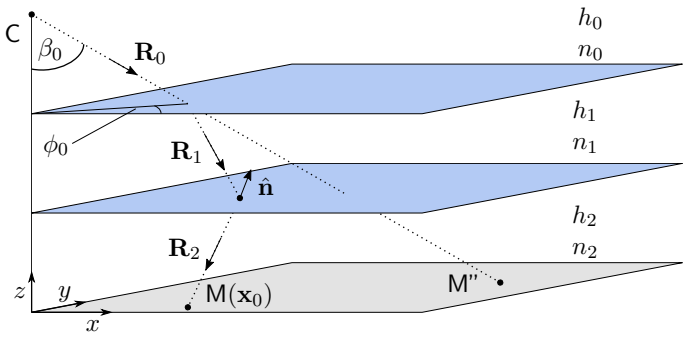

Figure 2.2: Illustration of ray paths starting at the camera C, defined by the angles β_0 and ϕ_0, for configuration 2 (see Figure 2.1 (b)). The ray is refracted at the two upper interfaces. The vectors $\mathbf{R}_i$ denote the ray propagation direction inside the respective materials. At $z = 0$, in the point M, or its position $\mathbf{x}_0$, denotes where the ray intersects the dot pattern. This point appears for the observer C at M''.

It is important to note, that the positions of the objects M of the images M' and M'' are not necessarily the same within this procedure, because the input variable is the position of the image rather than the object itself. This will be remedied in the last step of the following derivation.

Derivation

Consider a light ray starting at the camera C, $z = H$, with an initial direction defined by a polar angle β_0 between the ray and the vertical, and the azimuth angle ϕ_0. These are determined by the position of M'', as $\tan\beta_0 = |\overline{\mathsf{OM''}}|/H$ and $\tan\phi_0 = \overline{\mathsf{OM''}}_y/\overline{\mathsf{OM''}}_x$. Upon refraction at the first (flat) interface, the polar angle of the ray becomes $\beta_1 = \arcsin(n_0/n_1 \sin\beta_0)$, while the azimuth angle is conserved $\phi_1 = \phi_0$. The direction of the ray can therefore be expressed as

$$\mathbf{R}_i = \begin{pmatrix} \cos\phi_0 \sin\beta_i \\ \sin\phi_0 \sin\beta_i \\ -\cos\beta_i \end{pmatrix} \quad \text{for} \quad i = 0, 1. \tag{2.9}$$

propagation of rays from the camera necessary, thus lending itself as a starting point for the derivation of an approximation as well.

Let the surface normal vector at the point where the ray intersects the second interface at $z = h_2$ be

$$\hat{\mathbf{n}} = \begin{pmatrix} \cos\phi_{\hat{\mathbf{n}}} \sin\gamma \\ \sin\phi_{\hat{\mathbf{n}}} \sin\gamma \\ \cos\gamma \end{pmatrix} \quad \text{with} \quad \tan\gamma = |\boldsymbol{\nabla} h|. \tag{2.10}$$

Equation (2.6) can then be used to find the direction of the ray $\mathbf{R}_2$ for $0 < z < h_2$.

With $\mathbf{R}_0$, $\mathbf{R}_1$ and $\mathbf{R}_2$ known, the point M, where the ray crosses the $z = 0$ plane, is then given by

$$\mathbf{x}_0 = \sum_{i=0}^{2} \tilde{\mathbf{R}}_i \left| \frac{h_i}{(\mathbf{R}_i)_z} \right|, \quad \text{where} \quad \tilde{\mathbf{R}}_i = \begin{pmatrix} (\mathbf{R}_i)_x \\ (\mathbf{R}_i)_y \end{pmatrix}. \tag{2.11}$$

Through Equation (2.9) and Equation (2.6), Equation (2.11) provides an explicit function for the position of the object M, $\mathbf{x}_0(\phi_0, \beta_0, \phi_{\hat{\mathbf{n}}}, \gamma)$.

The procedure described above is applicable in the case of no surface gradient (denoted by a hat), but it is useful to use a simpler relation between a point $\hat{\mathbf{x}}_0$ and the view angles $(\hat{\beta}_0, \hat{\phi}_0)$ under which it is seen by the camera. Here, the azimuth angle of the ray is conserved, i.e., the ray stays in the same vertical plane. Therefore Equation (2.1) can be applied directly to find

$$|\hat{\mathbf{x}}_0| = \sum_{i=0}^{2} h_i \tan\hat{\beta}_i, \quad \text{where} \quad \hat{\beta}_i = \arcsin\left(\frac{n_0}{n_i} \sin\hat{\beta}_0\right), \tag{2.12}$$

and $\hat{\mathbf{x}}_0 = (|\hat{\mathbf{x}}_0| \cos\hat{\phi}_0, |\hat{\mathbf{x}}_0| \sin\hat{\phi}_0)$.

If $\hat{\mathbf{x}}_0 = \mathbf{x}_0$, then the apparent displacement is

$$\delta\mathbf{x} = \overline{\mathsf{M'M''}} = H \tan\beta_0 \begin{pmatrix} \cos\phi_0 \\ \sin\phi_0 \end{pmatrix} - H \tan\hat{\beta}_0 \begin{pmatrix} \cos\hat{\phi}_0 \\ \sin\hat{\phi}_0 \end{pmatrix}. \tag{2.13}$$

Now, to obtain an approximate relation for Equation (2.13), the Taylor expansions of Equation (2.11) and Equation (2.12) are calculated in the small angles β_0 and γ, and $\hat{\beta}_0$, respectively. Only terms of order one are kept, resulting in

$$\mathbf{x}_0 \approx \left(h_0 + \frac{n_0}{n_1}\left(h_1 + h_2 \frac{n_1}{n_2}\right)\right)\beta_0 \begin{pmatrix} \cos\phi_0 \\ \sin\phi_0 \end{pmatrix} - h_2\left(1 - \frac{n_1}{n_2}\right)\gamma \begin{pmatrix} \cos\phi_{\hat{\mathbf{n}}} \\ \sin\phi_{\hat{\mathbf{n}}} \end{pmatrix} \tag{2.14}$$

and

$$\hat{\mathbf{x}}_0 \approx \left(h_0 + \frac{n_0}{n_1}\left(h_1 + h_2\frac{n_1}{n_2}\right)\right)\hat{\beta}_0\begin{pmatrix}\cos\hat{\phi}_0\\ \sin\hat{\phi}_0\end{pmatrix}. \tag{2.15}$$

Note, that within the small slope approximation $\gamma \ll 1$, this is proportional to the negative surface gradient, i.e., $\gamma(\cos\phi_{\hat{\mathbf{n}}}, \sin\phi_{\hat{\mathbf{n}}}) \approx -\boldsymbol{\nabla}h$. Assume, now, that the images M' and M'' originate from the same object point M, i.e., $\mathbf{x}_0 = \hat{\mathbf{x}}_0$. Rearranging Equation (2.14) and Equation (2.15) for the terms $\tan\beta_0(\cos\phi_0, \sin\phi_0)$ and $\tan\hat{\beta}_0(\cos\hat{\phi}_0, \sin\hat{\phi}_0)$, respectively, and inserting these into Equation (2.13) one finds

$$\delta\mathbf{x} \approx H\frac{h_2\left(1-\frac{n_1}{n_2}\right)}{h_0 + \frac{n_0}{n_1}\left(h_1 + h_2\frac{n_1}{n_2}\right)}(-\boldsymbol{\nabla}h). \tag{2.16}$$

In order to obtain an expression similar to the result from Moisy et al. (2009), Equation (2.7), the constants $\alpha_{i,j} = 1 - n_i/n_j$ are defined and, using $H = h_0 + h_1 + h_2$, Equation (2.16) is rearranged to yield

$$\boldsymbol{\nabla}h \approx -\frac{\delta\mathbf{x}}{h^*} \tag{2.17}$$

where

$$\frac{1}{h^*} = \frac{1}{h_2\,\alpha_{1,2}} - \frac{1}{H}\left(\frac{h_1}{h_2}\frac{\alpha_{0,1}}{\alpha_{1,2}} + \frac{\alpha_{0,2}}{\alpha_{1,2}}\right). \tag{2.18}$$

For the special case $n_0 = n_1$, i.e., configuration 1, $\alpha_{0,1}$ vanishes and $\alpha_{0,2} = \alpha_{1,2}$, thus restoring Equation (2.7). The second term vanishes in the paraxial limit $H \to \infty$, and the relation used in Moisy et al. (2012) is obtained. For finite H, neglecting the term introduces an error in h^* that depends largely on the relative water depth h_1/H. For instance, if $H \approx 3\,\mathrm{m}$ and $h_1 = 1\,\mathrm{m}$, the additional error is about 10 %. Including the second term in Equation (2.18) comes at no additional cost and is therefore advisable.

2.2 Error analysis

When using a diagnostic it is important to be aware of its inherent limitations. The assumptions which the FS-SS is based on can be violated easily, e.g., by choosing too small distances H and h_2, or waves of significant steepness ε. The following is an investigation of errors in the retrieved surface gradient $\boldsymbol{\nabla}h$ that emerge due to finite slope $|\boldsymbol{\nabla}h|$, pattern-camera distance H, and surface elevation h, as well as parallax distortions. The parameter ranges (see Table 2.1) are based on the experimental setup at the large water

channel at the fluid mechanics laboratory at NTNU (see Jooss et al. 2021). Accordingly, results are presented in dimensional form. Where applicable, the analysis is performed for both configuration 1 and configuration 2.

Refractive index	n_0	1.0
	n_1	1.33
	n_2	1.0
Layer Thickness	h_0	1 - 4 m
	h_1	0.2 - 1.0 m
	h_2	5 - 15 cm
Pattern size	L	up to 1 m
Wave slope	ε	0.0 - 0.4

Table 2.1: Overview of parameter ranges typical for the FS-SS setup in configuration 2 when used at the large water channel at the fluid mechanics laboratory at NTNU.

2.2.1 Approximation Errors

As mentioned, the derivation of Equation (2.17) is based on the Taylor expansion of Equation (2.11) and Equation (2.12) and keeping only first order terms in the surface slope angle γ and the azimuthal camera view angles β_0 and $\hat{\beta}_0$. The expected error due to discarding higher order terms is investigated in the following by "simulating" the apparent displacements as seen by the camera and comparing the retrieved surface gradient with the prescribed one.

The simulation of the apparent displacement $\delta\mathbf{x} = \overline{\mathsf{M'M''}}$ consists of numerically finding the positions of M' and M'' for a given position $\mathbf{x}$, i.e., a point M. This is done by minimizing the distances $|\hat{\mathbf{x}}_0 - \mathbf{x}|$ and $|\mathbf{x}_0 - \mathbf{x}|$, using Equation (2.11) and Equation (2.12), respectively. This yields the correct view angles $(\hat{\beta}_0, \hat{\phi}_0)$ and (β_0, ϕ_0) and hence the observable apparent displacement $\delta\mathbf{x}$ via Equation (2.13).

The prescribed surface gradient is set to have only an x-component, i.e., $\boldsymbol{\nabla} h = (\tan\gamma, 0)$, and the position $\mathbf{x}$ of M is varied along the positive x- and y-axis as well as the diagonal $x = y$, parameterized by r. This covers almost all possible combinations of position $\mathbf{x}$ and surface gradient direction and is therefore deemed sufficient for the analysis.

The error in the approximate surface gradient obtained from Equation (2.17) using $\delta\mathbf{x}$ is divided into the error in magnitude, $|\boldsymbol{\nabla} h|$, and the direction of $\boldsymbol{\nabla} h$. Figure 2.3 (conf1) and Figure 2.4 (conf2) show contour plots of the

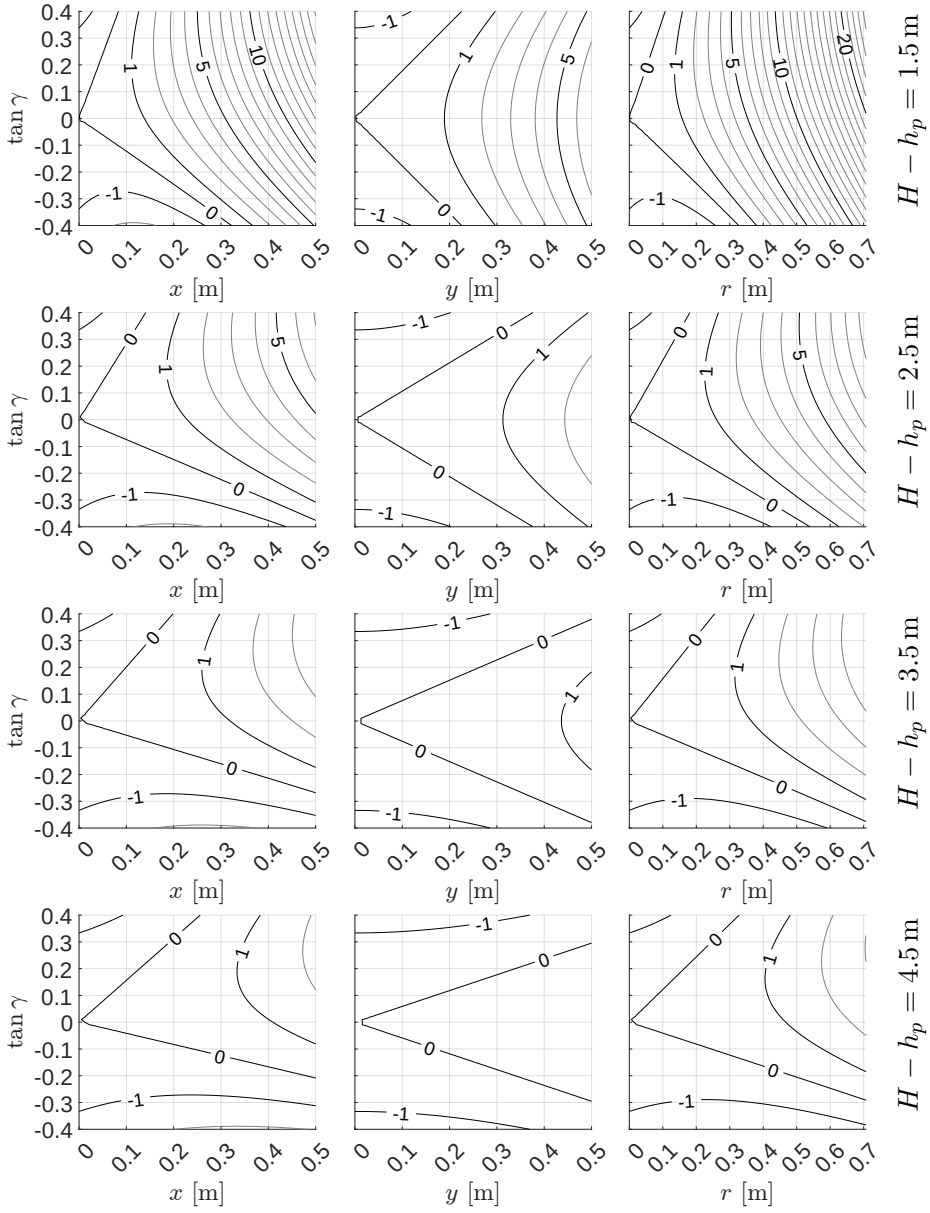

Figure 2.3: Relative error in the retrieved surface gradient $|\boldsymbol{\nabla} h|$ in percent, for configuration 1. The prescribed gradient is $\boldsymbol{\nabla} h = (\tan\gamma, 0)$. Columns 1-3: The object point M, $\mathbf{x}_0$, lies on $y = 0$, $x = 0$ and $x = y$, respectively. Rows 1-4: , $H - h_p = 1.5,\ 2.5,\ 3.5, 4.5\,\mathrm{m}$, $h_p = 5\,\mathrm{cm}$.

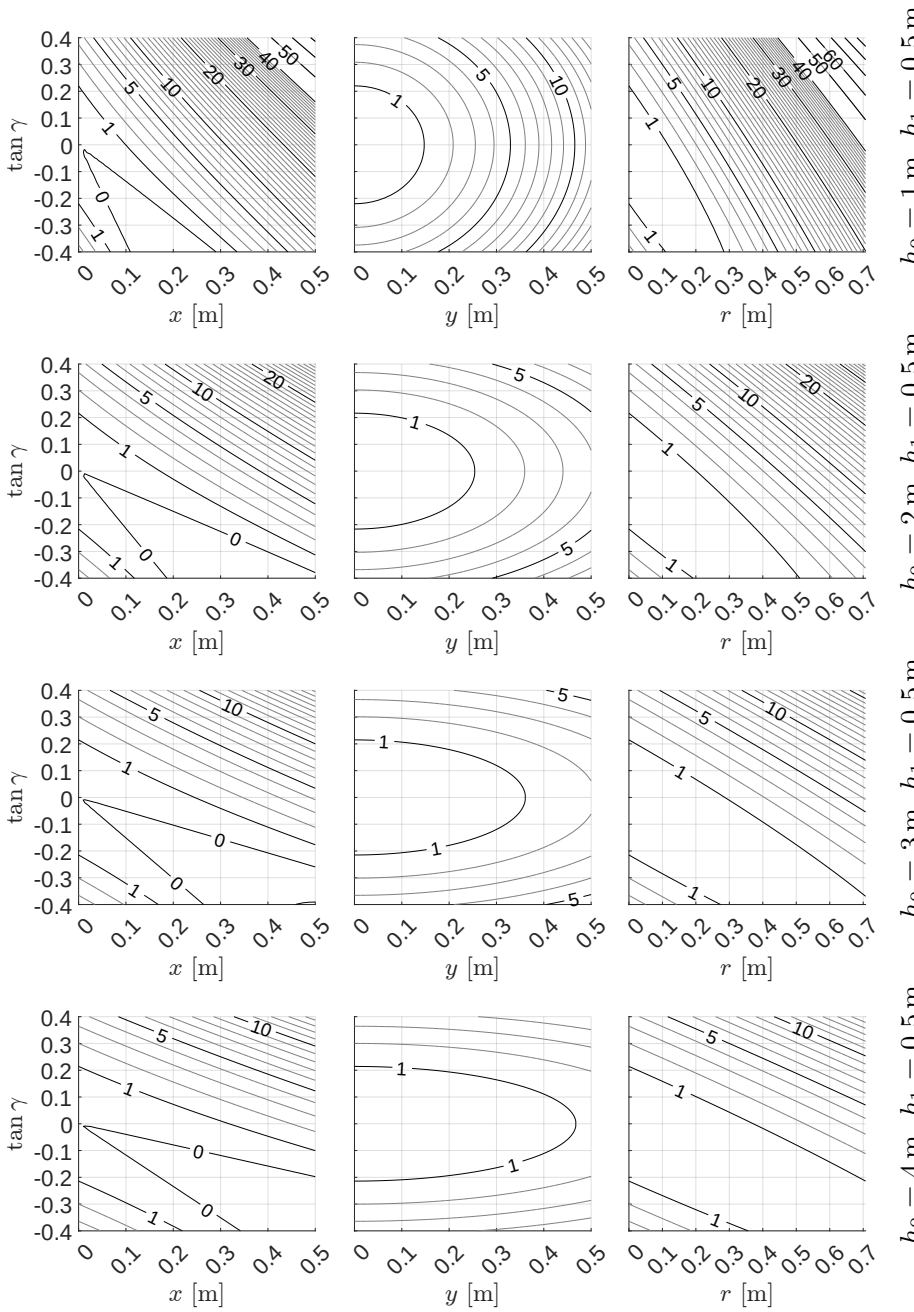

Figure 2.4: Same as Figure 2.3, but for configuration 2, with the same camera pattern distances H. Rows 1-4: $h_0 = 1,\ 2,\ 3, 4\,\text{m}$, $h_1 = 0.5\,\text{m}$, $h_2 = 5\,\text{cm}$.

relative errors in slope, $|\boldsymbol{\nabla} h_{\text{approx}}|/|\tan\gamma| - 1$, as a function of x, y, and r, and $\tan\gamma$. Errors in the surface gradient direction $\phi \approx \phi_{\hat{\mathbf{n}}}$ showed only small errors of $< 4°$ if the error in $|\boldsymbol{\nabla} h|$ was less than 20 %. Thus, for acceptable errors in the gradient, the direction of $\boldsymbol{\nabla} h$ is reliable as well.

Graphs of different pattern-surface distance and water depth were omitted as their influence on the results was not significant. Increasing h_p (or h_2) slightly decreases errors by a few percent points relative to the results shown.

In both configurations a strong asymmetry can be seen between errors for points along x and y. This becomes relevant when significant errors are expected, as such an asymmetry would lead to, e.g., skewed wave crests. Compared to configuration 1, configuration 2 is much more prone to exhibit systematic errors in general, especially for strong wave slopes and large $r = |\overline{\mathsf{OM'}}|$, where they are higher by a factor of 4-5. From the results it is clear, that a small camera distance of less than $h_2 = 2m$ ($H \sim 2.5L$) is to be avoided, as errors reach 20 % even for small surface slopes. If errors of less than 10 % are required, while finite surface slopes are expected in the experiment, the camera-pattern distance must be increased drastically. For instance, if $|\boldsymbol{\nabla} h| \leq 0.3$ a distance $h_2 > 4\,\text{m}$ ($H \sim 4.5L$) is necessary.

2.2.2 Errors from Wrong Remapping/Parallax

The surface gradient obtained via Equation (2.17) has to be attributed to the horizontal position of the point on the surface that lead to the displacement, i.e., point I (see Figure 2.1). To find a relation for the horizontal coordinates of I, it can be used that the points O, C, M" and I lie in the same plane shown in Figure 2.5.

Let J be the vertical projection of I onto the $z = 0$ plane. The distance $|\overline{\mathsf{OJ}}|$ between the origin and J can be expressed in terms of the angles β_0 and β_1

$$|\overline{\mathsf{OJ}}| = h_0 \tan\beta_0 + h_1 \tan\beta_1 = |\overline{\mathsf{OM"}}|\frac{h_0}{H} + h_1 \frac{\sin\beta_1}{\sqrt{1-\sin^2\beta_1}}. \tag{2.19}$$

Using the Snell-Descartes law, Equation (2.1) relating β_1 and β_0,

$$\sin\beta_1 = \frac{n_0}{n_1}\frac{\tan\beta_0}{\sqrt{1+\tan^2\beta_0}} = \frac{n_0}{n_1}\frac{\frac{|\overline{\mathsf{OM"}}|}{H}}{\sqrt{1+\left(\frac{|\overline{\mathsf{OM"}}|}{H}\right)^2}}. \tag{2.20}$$

Equation (2.19) and Equation (2.20) can be combined to obtain

$$\frac{|\overline{\mathsf{OJ}}|}{|\overline{\mathsf{OM"}}|} = \frac{h_0}{H} + \frac{h_1}{H}\sqrt{\left(\frac{n_1}{n_0}\right)^2 - \left(\frac{|\overline{\mathsf{OM"}}|}{H}\right)^2\left(1-\left(\frac{n_1}{n_0}\right)^2\right)^{-1}}. \tag{2.21}$$

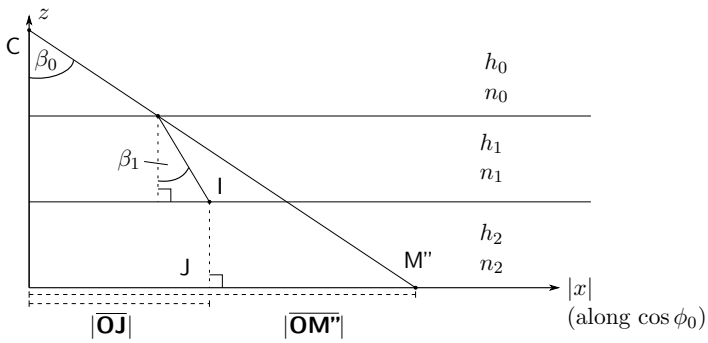

Figure 2.5: Illustration of parallax due to finite camera-pattern distance H. The surface gradient obtained from the displacement $\overline{\mathsf{M'M"}}$ must be ascribed to point I, or its vertical projection J. The figure shows the vertical plane containing M" obtained by rotating the x-z-plane by ϕ_0. Note that the light ray below I (reaching M) is omitted, since it points out of the plane.

The second term under the root can be neglected in the small angle approximation, which introduces errors of less than a percent for the parameters considered herein. Then, using $H = h_0 + h_1 + h_2$, it can be rearranged to match Equation (2.8) in form

$$\frac{|\overline{\mathsf{OJ}}|}{|\overline{\mathsf{OM"}}|} = 1 - \frac{h_2}{H} + \frac{h_1}{H}\left(1 - \frac{n_0}{n_1}\right). \tag{2.22}$$

One may be tempted to think that the remapping step is insensitive to whether $\overline{\mathsf{OM'}}$ or $\overline{\mathsf{OM"}}$ is used in Equation (2.22). Figure 2.6 shows the retrieved surface slope of a sinusoidal wave for typical parameters, without remapping and with remapping using both $\overline{\mathsf{OM"}}$ and $\overline{\mathsf{OM'}}$. The latter shows a severely skewed gradient profile, which increases with wave steepness, highlighting the importance of correct usage of Equation (2.22).

2.2.3 Finite Wave Height

The FS-SS setup in configuration 2 has more flexibility in the choice of the pattern-surface distance h_2, compared to configuration 1. Reducing it decreases sensitivity, which also increases the maximum allowed curvature of the surface before caustics render a measurement of displacements impossible, putting an upper bound on h_2. However, by reducing h_2, the assumption of negligible surface elevation $h/h_2 \approx 1$ can be violated, setting a lower bound for h_2.

The retrievability of displacements $\delta\mathbf{x}$ from the observed distortions of the dot pattern is discussed in detail in Moisy et al. (2009). Even before caustics

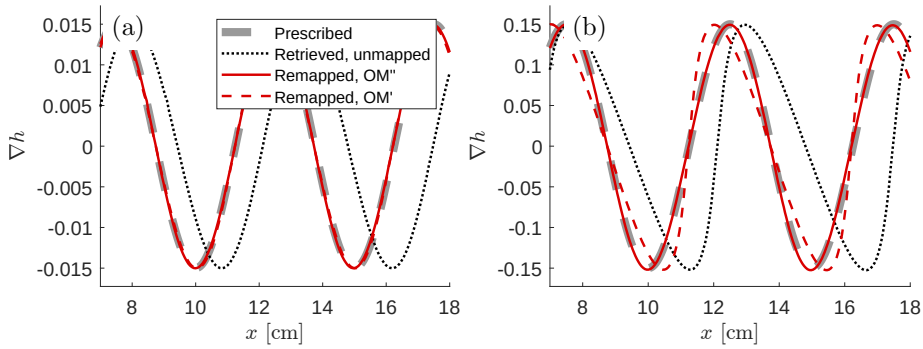

Figure 2.6: Example of recovered surface gradients obtained with and without the remapping procedure (see Equation (2.22)) for a waves of different steepness $\varepsilon = 0.015$ (a) and $\varepsilon = 0.15$ (b). Without remapping (dotted line) an x-dependent phase shift is observable, as reported in Moisy et al. (2009), and using $\overline{\mathsf{OM'}}$ (red dashed) instead of $\overline{\mathsf{OM''}}$ (red solid) for remapping leads to a skewed gradient field which increases with ε.

render the retrieval theoretically impossible, lensing effects due to the surface curvature stretch the dots too much for reliable measurements of $\delta\mathbf{x}$. A criterion is set by defining the strain σ as the change of the apparent displacement $\delta\mathbf{x}$ along $\overline{\mathsf{OM'}}$ with position M'. It is found therein, that a practical upper bound for the strain is $\sigma < 0.7$. For a plane wave of wavelength λ and amplitude a, the expected strain $\sigma(x)$ can be found using Equation (2.17) and is approximately

$$\sigma \approx \max\left|\frac{\partial \delta x}{\partial x}\right| = \max\left|h^* \frac{\partial^2}{\partial x^2} a \sin\left(\frac{2\pi}{\lambda}x\right)\right| \approx \frac{\varepsilon|\alpha_2|h_2 2\pi}{\lambda} \approx 2\frac{h_2}{\lambda}\varepsilon \quad (2.23)$$

where $H \gg h_2$, and $(n_0, n_1, n_2) = (1, 1.33, 1)$ were assumed. Thus, an upper bound for the surface pattern distance is $h_{2\max} \approx 0.35\lambda/\varepsilon$.

By moving the pattern closer to the surface, the small amplitude assumption $h(x,y)/h_2 \approx 1$ may not hold anymore. To show the effects of a finite surface displacement $h(x)$ and to find an appropriate value for h_2, the exact apparent displacement is simulated similar to the approach described in Section 2.2.1. To simplify the analysis, the surface is assumed to vary with x, and only $y = 0$ is considered, i.e., $h = h(x)$.

For a given point M at $z = 0$, the positions of M' and M'' are found numerically through ray propagation, and the distance between them gives the apparent displacement δx, from which the surface gradient is calculated via Equation (2.17). The gradient field is then obtained by remapping the

positions M″ via Equation (2.22). The additional step required in the ray propagation is the finding of the intersection of the ray with the surface $(x_{\text{intersect}}, h(x_{\text{intersect}}))$, after which the surface normal $\hat{\mathbf{n}}(x_{\text{intersect}})$ vector at that point is used to find the ray vector below the surface via Equation (2.6). Other than that, the procedure is unchanged.

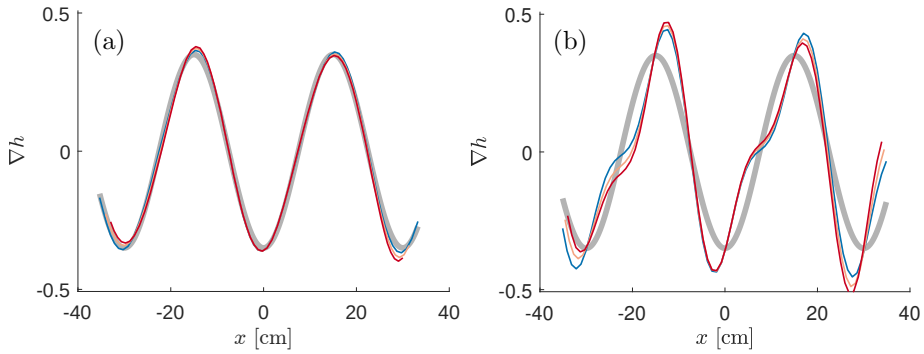

Figure 2.7: Example of recovered surface gradient of a plane wave for different surface-pattern distances h_2. (a) $a/h_2 = 0.01$, (b) $a/h_2 = 0.85$. The thick grey line shows the gradient of the prescribed wave. The distance between the water bottom and the camera varies between 1.5 m (red) and 10.5 m (blue).

Figure 2.7 shows an example of the obtained gradient field for a wave of both small and significant relative wave height $a/h_2 = 0.02$. The result is that the surface gradient is generally overestimated near the extrema, in addition to a slight overall skewness that can be reduced by increasing h_0.

A measure of this error can be defined in terms of the root mean square (rms) of the recovered gradient field relative to the exact rms, measured over the same domain,

$$\epsilon_{\text{rms}} = \frac{\text{rms}(\boldsymbol{\nabla} h_{\text{approx}})}{\text{rms}(\boldsymbol{\nabla} h_{\text{exact}})} - 1. \tag{2.24}$$

This error was calculated for a range of surface-pattern distances and waves of different wavelengths λ and steepness ε. The results shown in Figure 2.8 were obtained for configuration 2 with a camera-pattern distance of $h_0 = 10.5$ m and a water depth of $h_1 = 0.5$ m. No data is shown for cases where the expected strain σ exceeds 0.8 at lower λ, as the displacement field would be irretrievable. Similarly, no data is shown where the wave amplitude exceeds h_2, i.e., where the dot pattern is in contact with the water surface. Calculations for different values of h_0 and h_1 within the limits of the setup of the large water channel were also performed. The differences are mostly insignificant, i.e., about 2 %. The asymmetry, or skewness due to a reduction

in h_0 (see Figure 2.7 (b)) causes an increase of the small oscillations on the curves in Figure 2.8, which are due to extrema being moved outside the domain when increasing λ. Since the trend of the curves is not affected, however, these graphs are not shown.

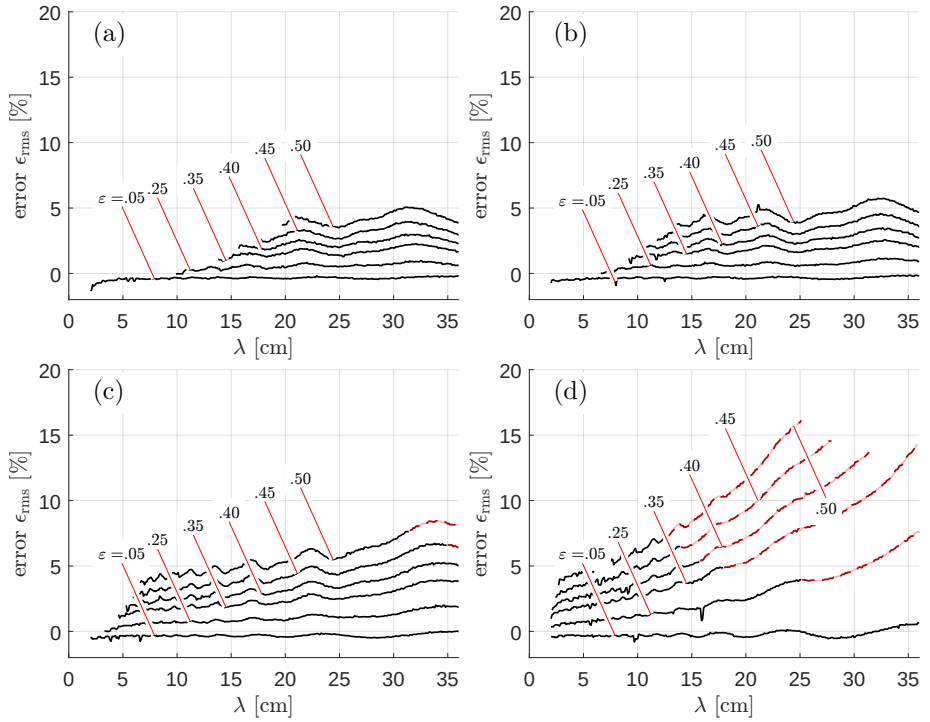

Figure 2.8: Error in the rms (see Equation (2.24)) of retrieved surface gradients for plane waves of various wavelengths λ, and steepness ε (indicated), for pattern-surface distances h_2 of (a) 15 cm, (b) 10 cm, (c) 5 cm and (d) 2 cm. The domain length is $L = 70\,\text{cm}$. To avoid parallax errors, the camera-pattern distance is chosen large, $h_0 + h_1 = 11\,\text{m}$. Each line begins at a lower wavelength determined by an upper bound for the maximum strain (see Equation (2.23)) $\sigma < 0.8$. Some lines have an additional bound at higher wavelengths due to the wave amplitude a exceeding the pattern-surface distance, i.e., $a \leq h_2$. The red, dashed parts of graphs represent parameter ranges where the pattern-surface distance h_2 is less than twice the wave amplitude a, $a/h_2 \geq \frac{1}{2}$.

Figure 2.8 reveals a limitation of the FS-SS at larger steepness values. If, for instance, steep waves with $\varepsilon = 0.5$ of both small $\lambda = 5\,\text{cm}$ and large wavelength $\lambda = 20\,\text{cm}$ are present, $h_2 \approx 2\,\text{cm}$ is required, but this introduces large errors for the measurements of longer waves. On the other hand, the errors do not exceed 20 %, so that a first estimate of the surface elevation can

be obtained by moving the pattern as close to water surface as is necessary to avoid too large image strain σ. The analyzed data can then be used to find the range of wavelengths and hence the expected magnitude of errors due to the reduction in h_2.

3

Systematic Errors in Doppler Shifts Extracted from Wave Spectra

The present work concerns systematic errors in the measurement of Doppler shift velocities (DSVs) from spatiotemporal surface data. In particular, the influence of horizontal shear is of central interest. In order to have control over the large number of free parameters, a numerical framework is developed, in which synthetic surface elevation data is generated, herein termed "simulation", and subsequently analyzed using the normalized scalar product (NSP) method. In this chapter, the theory and numerical scheme for the simulation are presented, and the choice of technical parameters of the simulation and the NSP method are discussed. This excludes scenario defining quantities such as the shape of the spectrum, current direction, etc., which are presented in detail in *Article II* and *Article III*.

Dimensional Basis

In the following, dimensional quantities will be denoted with an asterisk, e.g., L^* [m], T^* [s] and $g^* = 9.81\,\mathrm{m/s^2}$. The basis for the non-dimensionalization of all quantities herein is given by a length scale l^*_{ref} and time scale t^*_{ref}, defined by a reference wavenumber k^*_{ref} and its angular frequency $\omega^*_{\mathrm{ref}} =$

$\sqrt{g^* k^*_{\mathrm{ref}}}$ in quiescent water

$$l^*_{\mathrm{ref}} = \frac{2\pi}{k^*_{\mathrm{ref}}} \quad \text{and} \quad t^*_{\mathrm{ref}} = \frac{2\pi}{\omega^*_{\mathrm{ref}}} = \frac{2\pi}{\sqrt{g^* k^*_{\mathrm{ref}}}}. \tag{3.1}$$

An advantage of this choice is that all velocities, e.g., a background current U^*, are given as fractions of the reference wavenumber's quiescent water phase velocity, i.e., $U = U^* t^*_{\mathrm{ref}}/l^*_{\mathrm{ref}} = U^*/c^*_{p,0}(k^*_{\mathrm{ref}})$ with $c^*_{p,0} = \sqrt{g^*/k^*}$.

Additionally, angular frequencies and wavenumbers are normalized directly using ω^*_{ref} and k^*_{ref}, instead of using the defined time and length scales t^*_{ref} and l^*_{ref}. This normalizes all phases by 2π, which will be denoted in the same way, i.e., a phase of ϕ^* and a non-dimensional phase $\phi = \phi^*/2\pi$. Within this system, care must be taken when re-introducing dimensions. For instance, if a resolution is given by $\delta\omega = \frac{1}{T}$, then,

$$\delta\omega = \frac{1}{T} \iff \frac{\delta\omega^*}{\omega^*_{\mathrm{ref}}} = \frac{1}{T^*/t^*_{\mathrm{ref}}} \iff \delta\omega^* = \frac{2\pi}{T^*}. \tag{3.2}$$

The same can be obtained by reintroducing the time scale t^*_{ref} via multiplication (both sides) with $1/t^*_{\mathrm{ref}}$ and multiplying only the right–hand side by 2π. The latter procedure appears arbitrary, but the factor 2π can be understood to restore radians[3]. Where non-dimensional and dimensional equations differ in form, clarification will be provided.

3.1 Theory

For the simulation and analysis of surface waves in this thesis, the description of water waves atop a varying current is pivotal. To isolate and focus on the effects due to a background current, with focus on remote sensing applications, the following simplifying assumptions are made:

1. The fluid is inviscid, incompressible and its properties are homogeneous and constant.
2. Fluid motion due to waves is affected by a prescribed background current, but not vice versa, i.e., the interaction is unidirectional.
3. Surface tension and finite water depth effects are negligible.
4. The slope, or steepness, $\varepsilon \ll 1$ of waves is small.
5. Background currents are stationary $\mathbf{U} \neq \mathbf{U}(t)$.

[3] It is possible to keep track of radians formally with a reference phase 2π rad; this would necessitate the introduction of powers of rad into almost all well-established equations, which is impractical. For instance, the "velocity" $\tilde{\mathbf{c}}$ in Equation (1.3) would have units rad m/s, when it should only be m/s.

6. The vertical shear of the background current is moderate in the sense described in Ellingsen and Li (2017).
7. The horizontal shear of the background current is small compared to the wave's frequency (see Section 3.1.2).
8. Background currents are separable in terms of vertical and horizontal coordinates, i.e., $\mathbf{U}(\mathbf{x}, z) = \mathbf{U}_h(\mathbf{x})f(z)$.

3.1.1 Dispersion Relation

The surface elevation ζ of a wave with infinitesimal amplitude a at the air-water interface is described by a cosine in time and space, i.e., $\zeta(\mathbf{x}, t) = a\cos(2\pi(\mathbf{k}\cdot\mathbf{x} - \omega t))$. The wave's wavevector $\mathbf{k}$ (or wavenumber $k = |\mathbf{k}|$ in 1D) and its frequency ω are linked by the dispersion relation $\omega_{\mathrm{DR}}(\mathbf{k})$. From the dispersion relation one obtains the propagation speed of wave crests and troughs, the phase speed $c_p = \omega/k$. Energy carried by the wave, on the other hand, moves at the group velocity $\mathbf{c}_g = \boldsymbol{\nabla}_{\mathbf{k}}\omega$ (see, e.g., Peregrine 1976), where $\boldsymbol{\nabla}_{\mathbf{k}} = (\partial/\partial k_x, \partial/\partial k_y)$.

Under the assumptions 1, 2, 3 and 4 and in the presence of a uniform current, the dispersion relation can be derived to give Equation (1.2) (see, e.g., Peregrine 1976), which is non-dimensionalized to

$$\omega_{\mathrm{DR}}(\mathbf{k}) = \sqrt{k} + \mathbf{U}\cdot\mathbf{k}. \tag{3.3}$$

For a moderately vertically sheared background current $\mathbf{U}(z)$, the dispersion relation becomes (Stewart and Joy 1974)

$$\omega_{\mathrm{DR}}(\mathbf{k}) = \sqrt{k} + \mathbf{k}\cdot\tilde{\mathbf{c}}(k) \quad \text{where} \quad \tilde{\mathbf{c}}(k) = 4\pi k\int_{-\infty}^{0}\mathbf{U}e^{4\pi k z}\,\mathrm{d}z\,. \tag{3.4}$$

For this approximation to hold, it is required that the depth averaged vertical shear is small (Ellingsen and Li 2017) relative to the quiescent water phase velocity, i.e.

$$\delta(\mathbf{k}) = \frac{1}{c_p}\int_{-\infty}^{0}\frac{\mathbf{k}}{k}\cdot\frac{\partial\mathbf{U}}{\partial z}e^{4\pi k z}\,\mathrm{d}z \ll 1. \tag{3.5}$$

Ellingsen and Li (2017) show that even for moderate vertical shear, where $\delta = 0.35$, Equation (1.3) gives reliable results. For Stronger vertical shear they provide an alternative approximation, which could be implemented here as well. (Factors of $2\pi = l^*_{\mathrm{ref}}k^*_{\mathrm{ref}}$ appear in Equation (3.4) and Equation (3.5) due to non-dimensionalization of $k^*\,\mathrm{d}z^*$ and k^*z^*.)

In the absence of vertical shear $\tilde{\mathbf{c}} = \mathbf{U} = \text{const.}$, the group velocity evaluates to

$$\mathbf{c}_g = \hat{\mathbf{e}}_\mathbf{k} \frac{1}{2\sqrt{k}} + \mathbf{U} = \mathbf{c}_{g,0} + \mathbf{U}, \tag{3.6}$$

where $\hat{\mathbf{e}}_\mathbf{k} = \mathbf{k}/k$. For a vertically sheared current, however, the group velocity cannot be obtained by replacing $\mathbf{U}$ with $\tilde{\mathbf{c}}(k)$, because taking the derivatives with respect to k produces additional terms from the integrand of Equation (3.4) (Banihashemi and Kirby 2019). One obtains

$$\mathbf{c}_g = \mathbf{c}_{g,0} + 4\pi \int_{-\infty}^{0} [k\mathbf{U} + \hat{\mathbf{e}}_\mathbf{k}(\mathbf{k}\cdot\mathbf{U}) + 4\pi k z\, \hat{\mathbf{e}}_\mathbf{k}(\mathbf{k}\cdot\mathbf{U})] e^{4\pi k z}\, \mathrm{d}z\,. \tag{3.7}$$

The integral can be solved analytically for a range of profiles, particularly under assumption 8, that $\mathbf{U}$ is separable. An example will be given in the next section.

3.1.2 Horizontally Varying Current

When the background current is a function of the horizontal coordinates $\mathbf{U} = \mathbf{U}(\mathbf{x})$, the description of the propagation of waves depends on the scale on which the current varies. On one end of the scale is a step-change in the current, which can be viewed as an approximation to a gradual transition, when it occurs over a length much smaller than the wavelength of a wave. Solutions to this problem are readily available but not the focus of this work. On the other end of the scale are currents where the change is slow enough to be considered constant on the scale of a wave's wavelength, assumption 7. This is the regime of geometrical optics (see, e.g., Peregrine 1976, Voronovich 1976). The slow variation of $\mathbf{U}$ allows for the definition of a local dispersion relation using the local value of the background current. Following the formalism given in, e.g., Whitham (1999), Gerber (1993) and White and Fornberg (1998), it is

$$\Omega(\mathbf{k};\mathbf{x}) = \omega_{\mathrm{DR}}(\mathbf{k};\mathbf{x}) = \sqrt{k} + \mathbf{k}\cdot\mathbf{U}(\mathbf{x}), \tag{3.8}$$

leading to locally defined phase and group velocities as well. How this is used in the propagation of waves to obtain the surface elevation is discussed in Section 3.1.4.

The numerical framework developed in the present work allows for horizontal and vertical shear, with the restriction that the current is separable, i.e., $\mathbf{U} = \mathbf{U}_h(\mathbf{x}) f(z)$, so that Equation (3.4) becomes approximately

$$\Omega(\mathbf{k};\mathbf{x}) = \sqrt{k} + \mathbf{k}\cdot\mathbf{U}_h(\mathbf{x}) \left[4\pi k \int_{-\infty}^{0} f(z) e^{4\pi k z}\, \mathrm{d}z \right]. \tag{3.9}$$

Note that $\mathbf{U}_h$ represents the surface current only if $f(0) = 1$. For comparisons of scenarios with and without shear it is advisable to define f such that the quantity in parentheses is on the order of one for wavenumbers in consideration.

Similarly, the horizontal component of the current profile can be factored out in Equation (3.7). The equations for the dispersion relation and group velocity in the presence of horizontal shear and vertical shear thus become

$$\Omega(\mathbf{k};\mathbf{x}) = \sqrt{k} + \mathbf{k}\cdot\mathbf{U}_h(\mathbf{x})I_1[k;f] \tag{3.10}$$

and

$$\mathbf{c}_g = \boldsymbol{\nabla}_\mathbf{k}\Omega = \mathbf{c}_{g,0} + \mathbf{U}_h\, I_1[k;f] + \hat{\mathbf{e}}_\mathbf{k}(\hat{\mathbf{e}}_\mathbf{k}\cdot\mathbf{U}_h)\,(I_1[k;f] + I_2[k,f]), \tag{3.11}$$

where I_1 and I_2 are k-dependent depth-integrals of $f(z)$

$$I_1[k;f] = 4\pi k\int_{-\infty}^{0} f(z)e^{4\pi kz}\,\mathrm{d}z \tag{3.12}$$

and

$$I_2[k;f] = (4\pi k)^2\int_{-\infty}^{0} zf(z)e^{4\pi kz}\,\mathrm{d}z\,. \tag{3.13}$$

For the numerical implementation it is useful to obtain an analytical expression for the integrals, which is readily obtained for a variety of functions $f(z)$. A fairly general family of profiles is given by the exponential polynomial

$$f(z) = \sum_{n=0}^{\infty} b_n z^n e^{2\pi\alpha_n z} \qquad b_n, \alpha_n \in \mathbb{R}. \tag{3.14}$$

Given this profile, the integrals I_1 and I_2 evaluate to

$$I_1 = \sum_{n=0}^{\infty} b_n \frac{2k}{(2k+\alpha_n)^{n+1}}\left(\frac{-1}{2\pi}\right)^n n! \tag{3.15}$$

and

$$I_2 = \sum_{n=0}^{\infty} -b_n \frac{(2k)^2}{(2k+\alpha_n)^{n+2}}\left(\frac{-1}{2\pi}\right)^n (n+1)!. \tag{3.16}$$

Note, that $I_1 = -I_2$ for a vertically uniform profile $b_n = 0\,\forall\, n > 0$, leading to the third term in Equation (3.11) to vanish.

If the vertical profile is given in terms of dimensional variables b_n^* and α_n^*, then the dimensionless quantities for the equations above are $b_n = b_n^*(2\pi)^n$ and $\alpha_n = \alpha_n^*/k_{\mathrm{ref}}^*$.

3.1.3 Linear Superposition

A random sea state is typically comprised of waves with a range of frequencies (or wavenumbers) and a range of propagation directions (see, e.g., Pierson 1955). In the absence of horizontal shear, the surface elevation can be modelled by superposition of $N_{\mathbf{k}}$ individual waves of amplitude $a_{i_{\mathbf{k}}}$ (see, e.g., Socquet-Juglard et al. 2005)

$$\zeta(\mathbf{x},t) = \sum_{i_{\mathbf{k}}} a_{i_{\mathbf{k}}} \cos\left[2\pi(\mathbf{k}_{i_{\mathbf{k}}} \cdot \mathbf{x} - \omega_{\mathrm{DR}}(\mathbf{k}_{i_{\mathbf{k}}})t + \phi_{0,i_{\mathbf{k}}})\right], \tag{3.17}$$

where $\phi_{0,i_{\mathbf{k}}}$ is a random phase between 0 and 1, and $i_{\mathbf{k}} = \{1, 2, .., N_{\mathbf{k}}\}$. In general terms, the argument of the cosine is given as the phase $\phi(\mathbf{x}, t)$,

$$\zeta(\mathbf{x},t) = \sum_{i_{\mathbf{k}}} a_{i_{\mathbf{k}}} \cos(2\pi\phi_{i_{\mathbf{k}}}(\mathbf{x},t)) = \sum_{i_{\mathbf{k}}} \zeta_{i_{\mathbf{k}}}(\mathbf{x},t), \tag{3.18}$$

where the local frequency and wavevector are $\omega = -\partial\phi/\partial t$ and $\mathbf{k} = \boldsymbol{\nabla}\phi$, respectively. In the presence of horizontal shear, these are locally defined quantities and must fulfill the dispersion relation $\omega = \omega_{\mathrm{DR}}(\mathbf{k}; \mathbf{x})$ everywhere. Furthermore, for a time-independent current, the frequency of a wave-component is constant $\omega = \text{const.}$ (Peregrine 1976), so that the phase separates into a spatial and temporal part

$$\phi_{i_{\mathbf{k}}}(\mathbf{x},t) = \hat{\phi}_{i_{\mathbf{k}}}(\mathbf{x}) - \omega_{i_{\mathbf{k}}} t + \phi_{0,i_{\mathbf{k}}}, \tag{3.19}$$

where the constant $\phi_{0,i_{\mathbf{k}}}$ has been added for convenience. Note, that wave action conservation dictates that the amplitudes $a_{i_{\mathbf{k}}}$ are functions of $\mathbf{x}$ as well (see, e.g., Voronovich 1976). This is neglected in this work to simplify the interpretation of results.

3.1.4 Ray Tracing Equations

For a stationary current, slowly varying current, the phase field $\hat{\phi}_{i_{\mathbf{k}}}(\mathbf{x})$ of each wave component (see Equation (3.18)) is determined by the dispersion relation through

$$\omega_{i_{\mathbf{k}}} = \Omega(\mathbf{k}_{i_{\mathbf{k}}}(\mathbf{x}); \mathbf{x}) = \Omega(\boldsymbol{\nabla}\hat{\phi}_{i_{\mathbf{k}}}(\mathbf{x}); \mathbf{x}). \tag{3.20}$$

This is a first order nonlinear partial differential equation for the $\hat{\phi}_{i_{\mathbf{k}}}(\mathbf{x})$ and can be reduced to an ordinary differential equation using the method of characteristics (see, e.g., Gerber 1993, Voronovich 1976, White and Fornberg 1998). The following considerations are independent of the index $i_{\mathbf{k}}$, which is dropped for brevity.

Using the method of characteristics, one finds the coupled set of ODEs

$$\frac{\partial}{\partial t'}\begin{pmatrix}\mathbf{r}(t';s)\\ \hat{\phi}(t';s)\\ \mathbf{k}(t';s)\end{pmatrix} = \begin{pmatrix}\boldsymbol{\nabla}_{\mathbf{k}}\Omega\\ \mathbf{k}\cdot\boldsymbol{\nabla}_{\mathbf{k}}\Omega\\ -\boldsymbol{\nabla}\Omega\end{pmatrix}\Bigg|_{\mathbf{r}(t';s)}, \tag{3.21}$$

where t' parameterizes each ray $\mathbf{r}$, and s is a parameter (see details below). The initial conditions, denoted by a subscript 0, are

$$\begin{pmatrix}\mathbf{r}_0(s)\\ \hat{\phi}_0(s)\\ \mathbf{k}_0(s)\end{pmatrix} = \begin{pmatrix}\mathbf{r}(0;s)\\ \hat{\phi}(0;s)\\ \mathbf{k}(0;s)\end{pmatrix} = \begin{pmatrix}\mathbf{r}_0(s)\\ \hat{\phi}(\mathbf{r}_0(s))\\ \mathbf{k}(\mathbf{r}_0(s))\end{pmatrix}, \tag{3.22}$$

which must fulfill the additional conditions

$$\Omega(\mathbf{r}_0(s),\mathbf{k}_0(s)) = \omega \quad \text{and} \quad \frac{\partial\hat{\phi}_0(s)}{\partial s} = \frac{\partial\mathbf{r}_0(s)}{\partial s}\cdot\mathbf{k}_0(s). \tag{3.23}$$

The starting point for finding the phase field $\hat{\phi}(\mathbf{x})$ is Equation (3.22). The phase $\hat{\phi}_0(s)$ and wavevector $\mathbf{k}_0(s)$ of, e.g., an incoming wave, are prescribed along a line $\mathbf{r}_0(s)$, parameterized by $s \in [0,1]$. Solving the ODE in Equation (3.21) for one value of s provides $\hat{\phi}$ and $\mathbf{k}$ on the ray $\mathbf{r}(t';s)$, which follows the group velocity $\boldsymbol{\nabla}_{\mathbf{k}}\Omega$. Thus, by solving the ODE for all $s \in [0,1]$, the solution to the PDE is found for the area spanned by the union of the ray positions $\mathbf{r}(t';s)$.

In the present work, scenarios are considered where a monomodal spectrum propagates through the domain from one side. Therefore, the initial conditions are set at the bottom of the domain $\mathbf{r}_0(s) = (x_0(s), y_{\min})$. Assuming, furthermore, that the current profile is constant along $\mathbf{r}_0(s)$, the initial conditions for the phase and wavevector simplify to

$$\mathbf{k}_0(s) = \text{const.} \quad \text{and} \quad \hat{\phi}_0(s) = \hat{\phi}_0(0) + k_{x,0}\,(x_0(s) - x_0(0)). \tag{3.24}$$

The procedure described above assumes that the solution exists, which is not generally the case for all initial conditions. Specifically, when neighboring rays cross, the solution becomes multivalued and is not valid anymore. Physically, the crossing of rays means convergence of energy, leading to diverging amplitudes (see, e.g., Gerber 1993, McKee 1974), similar to the focusing of light by magnifying glass. At these points linear wave theory breaks down and requires more sophisticated treatment.

If and where caustics (ray crossings) appear is difficult to predict in general. The simplest approach is to solve the ray equation and check for ray crossings afterward.

3.2 Simulation

The implementation for calculating Equation (3.18) developed in this work consists of four major steps. First, the scenario to simulate is set up in terms of domain, background current, resolutions and wave spectrum. Second, the waves' phase $\hat{\phi}_{i_\mathbf{k}}$ for each input wavevector is found along rays by using the method of characteristics described in Section 3.1.4. Third, that phase is interpolated onto a Cartesian grid, and in the last step the surface elevation is calculated by superposition according to Equation (3.18) for each time step. The procedure is illustrated in Figure 3.1 and details for each step are given below.

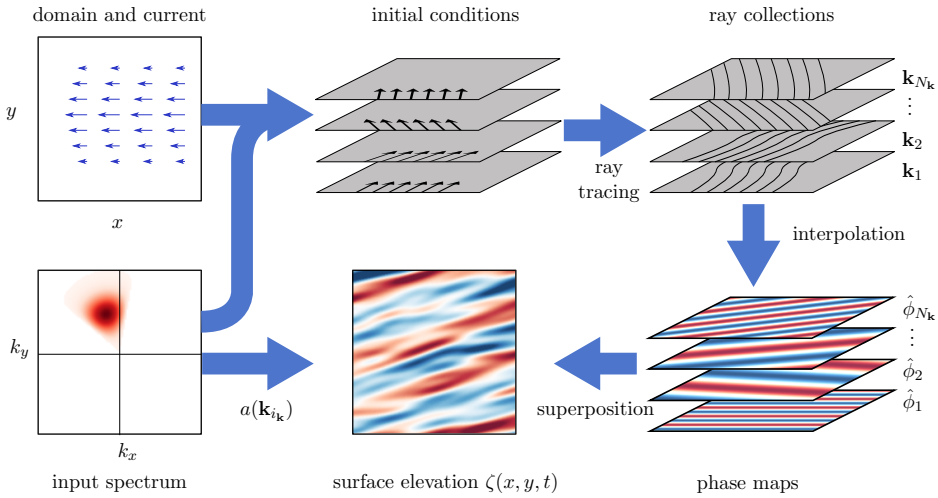

Figure 3.1: Scheme used for generating synthetic surface elevation data: For a specified domain, current and input spectrum, the initial conditions for waves propagating through the domain are determined and the phase field $\hat{\phi}$ along rays is then found using ray tracing and subsequently interpolated onto a Cartesian grid. In the last step, the individual wave components are superposed to obtain the surface elevation ζ.

3.2.1 Setup

The spatial domain is specified in terms of domain lengths L_x and L_y and uniform spatial resolutions δx and δy. Typically, a square domain is considered with $L_x = L_y = L$ and $\delta x = \delta y$. Similarly, the time domain of the video is set by duration T and constant time step δt. To sufficiently sample waves of the highest input wavenumber k_max and frequency ω_max, end hence avoid aliasing, the resolutions are set such that there are at least seven sample points per wavelength λ_min and period τ_min, i.e., $\delta x = \lambda_\text{min}/7$,

$\delta t = \tau_{\min}/7$.

For the input wavevectors and the corresponding amplitudes, an amplitude spectrum function $a(\mathbf{k})$ is defined and evaluated on an evenly spaced k_x-k_y-grid, with resolution δk_{in}. Only the $N_{\mathbf{k}}$ wavevectors $\mathbf{k}$ for which $a(\mathbf{k}) \neq 0$ and their corresponding amplitudes are stored in a list $(k_{i_{\mathbf{k}}}, a_{i_{\mathbf{k}}})$ with $i_{\mathbf{k}} = \{1, 2, .., N_{\mathbf{k}}\}$. (if $L_x \neq L_y$, separate resolutions $\delta k_x \neq \delta k_y$ can be set). To ensure that a continuous spectrum is emulated, different values for the resolution were tested. Convergence in the extracted DSVs was reached at about $\delta k_{\text{in}} \approx 0.35/L$ ($\delta k^*_{\text{in}} \approx 2\pi\, 0.35/L^*$). All subsequent calculations were performed using $\delta k_{\text{in}} = 0.3366/L$.

The right–hand side of Equation (3.21) requires the evaluation of the derivatives $\boldsymbol{\nabla}\Omega$ and $\boldsymbol{\nabla}_{\mathbf{k}}\Omega$ at each iteration of the ray tracing step. The velocity profile is prescribed as $\mathbf{U} = \mathbf{U}_h(\mathbf{x})f(z)$, with f being of the form of Equation (3.14) defined by parameter pairs (b_n, α_n). Using this form, the Integrals I_1 and I_2, that appear in the expressions for $\boldsymbol{\nabla}\Omega$ and $\boldsymbol{\nabla}_{\mathbf{k}}\Omega$ (see Equation (3.10) and Equation (3.11)), are evaluated analytically according to Equation (3.15) and Equation (3.16), avoiding costly numerical integration. To also avoid numerical differentiation, the horizontally varying part $\mathbf{U}_h$ is defined in terms of explicit functions for both $\mathbf{U}_h$ itself and its derivatives $\partial\mathbf{U}_h/\partial x$ and $\partial\mathbf{U}_h/\partial y$.

3.2.2 Ray Tracing

The first step in finding the phase field $\hat{\phi}(\mathbf{x})$ for each input wavevector $\mathbf{k}$ (the index $i_{\mathbf{k}}$ is dropped for brevity) is solving Equation (3.21) such that the domain of interest is covered by rays. Clearly the coverage is determined by the choice of the initial conditions for ray coordinates $\mathbf{r}_0(s)$ and wavevectors $\mathbf{k}_0(s)$. Using the additional assumption that the current does not change along the lower edge of the domain ($y = -L/2$), the initial conditions are set using Equation (3.24). A preliminary ray tracing run is carried out with two rays originating at the start and end point of the initial condition line, i.e., $x_0(0)$ and $x_0(1)$. If the rays lie entirely or partially inside the domain, it can be inferred that the union of all rays from $x_0(s)$ do not suffice for full coverage, and $x_0(s)$ must be extended. This is iterated until coverage is guaranteed. The initial condition line is then discretized with constant spacing $\Delta x = \delta x\, k_0/k_{0,y}$, i.e., δx-spacing perpendicular to $\mathbf{k}_0$, to obtain sufficiently dense coverage of the domain. For each initial point, a ray is then found by solving Equation (3.21) using the Dormand-Prince algorithm (Dormand and Prince 1980).

To ensure that only valid ray collections are used in the subsequent inter-

polation step, each ray collection is examined for caustics by finding the intersections of initially neighboring rays. If any points of intersection lie within the domain, the respective wave component $\mathbf{k}$ is flagged and excluded from subsequent calculations, since the phase $\hat{\phi}$ becomes multivalued. The scenarios considered in *Article II* and *Article III* were chosen such that no caustics appear.

A common test case for the ray tracing step is the annular current studied in Gerber (1993) and White and Fornberg (1998). The velocity field is of the form $\mathbf{U} = U(r)\hat{\mathbf{e}}_\theta$, where $U(r)$ a parabolic radial profile with maximum $U_{\max}$

$$U(r) = -4\frac{U_{\max}}{(R_{\text{out}} - R_{\text{in}})^2}(r - R_{\text{out}})(r - R_{\text{in}}), \tag{3.25}$$

for radii in the range $R_{\text{in}} < r < R_{\text{out}}$; outside that range the velocity is zero. Using the same parameters $R^*_{\text{in}} = 40\,\text{km}$, $R^*_{\text{out}} = 160\,\text{km}$ and $U^*_{\max} = 2\,\text{m/s}$,

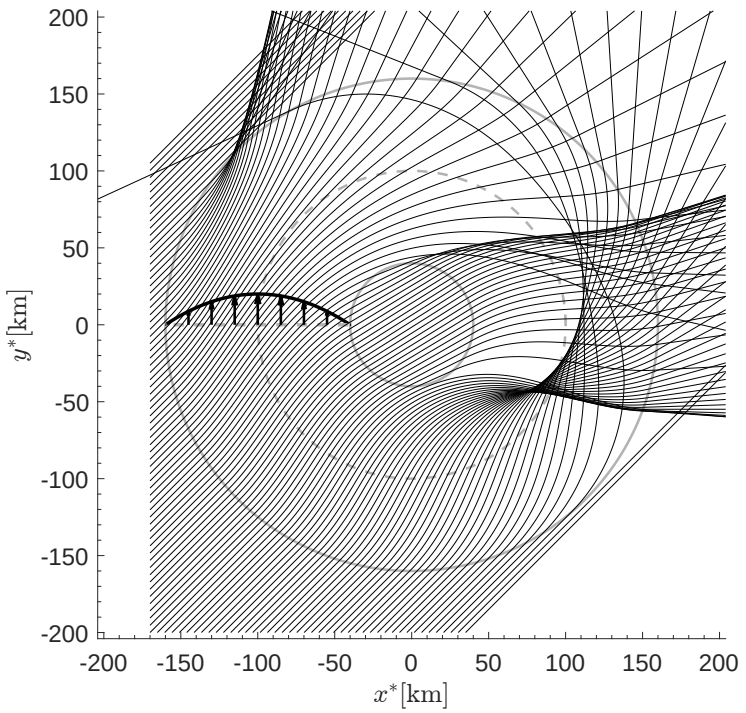

Figure 3.2: Ray tracing result for an annular current. The parameters for this test case are taken from Gerber (1993).

incident waves with a period of $T^* = 10\,\text{s}$ are propagated through the domain from the bottom left corner of the domain, where the initial wavevector

direction is 45° from the x-axis. The resulting rays are shown in Figure 3.2, visually indistinguishable from Figure 16 in Gerber (1993). When making a similar comparison with Figure 5 in White and Fornberg (1998), small deviations in the outgoing ray directions can be observed, even for rays not passing through the region of current. A likely explanation for this is, that the current therein was not represented by an analytic expression, unlike in Gerber (1993), but an interpolation scheme using rastered current information (obtained using the same analytic expression).

3.2.3 Interpolation

For the superposition of the individual wave components $\zeta_{i_\mathbf{k}}$, the phase $\hat{\phi}_{i_\mathbf{k}}(\mathbf{x})$ is required on a Cartesian grid spanning the domain. To obtain it from the results of the ray tracing step, first, the position and phase $(\mathbf{r}, \hat{\phi}(\mathbf{r}))$ along the rays is collected from all rays, and values lying outside the domain are discarded. The interpolation of the so obtained scattered phase data is achieved using a linear 2D Delaunay scheme (Amidror 2002), with query points defined by the domain size L and resolution δx. The linear interpolation method was deemed sufficient based on the density of data points from the ray collections; the initial distance between rays and the evaluation steps along each ray were chosen such that the distance between points is approximately δx, which in turn was set to ensure > 7 data points per wavelength.

3.2.4 Video Assembly

The last step in the simulation is the superposition of the surface elevation $\zeta_{i_\mathbf{k}}(\mathbf{x}, t)$ of individual wave components $\mathbf{k}_{i_\mathbf{k}}$.

The summation in Equation (3.18) is performed for each time t on the evenly δt-spaced interval $[0, T]$. First, the phase $\phi_{i_\mathbf{k}}(\mathbf{x}, t)$ of each wave component is determined using Equation (3.19), where each phase offset $\phi_{0,i_\mathbf{k}}$ is taken from a uniform distribution in order to obtain a random sea state. Then the wave amplitudes $\zeta_{i_\mathbf{k}}(\mathbf{x}, t) = a_{i_\mathbf{k}} \cos(2\pi\, \phi_{i_\mathbf{k}}(\mathbf{x}, t))$ are calculated and superposed[4]. (Note that the phase offset $\phi_{0,i_\mathbf{k}}$ is not re-randomized when repeating the calculation for a different time t).

This process is repeated to obtain several (typically 100) realizations of the same scenario, with different sets of phase offsets $\phi_{0,i_\mathbf{k}}$.

[4]Since the superposition procedure consists of pointwise multiplication, addition and summation of matrices, which are highly parallelizable, utilization of a GPU instead of a CPU yielded a significant reduction in computation time. The computations were performed on a desktop PC (Intel Core i9-12900, 64GB DDR5 RAM, NVIDIA GeForce RTX 3070).

3.3 Doppler Shift Velocity Extraction

3.3.1 Normalized Scalar Product Method

To obtain the wavenumber dependent DSVs $\tilde{\mathbf{c}}(k)$ from spatiotemporal surface elevation data $\zeta(\mathbf{x}, t)$ for a list of wavenumbers $k \in \{k_1, k_2, ..., k_j, ...k_M\}$, the approach given in Smeltzer et al. (2019) is used. It is based on the NSP method (see, e.g., Huang and Gill 2012, Huang et al. 2016, Serafino et al. 2010), where the overlap (in terms of a normalized scalar product) of measured spectral intensity and a fitting function, representing the dispersion relation, is optimized. The implementation of the DSV extraction in this thesis is based on the code found in Smeltzer (2022), with minor modifications improving computation speed.

From the surface elevation data $\zeta(\mathbf{x}, t)$, with $x, y \in [0, L]$ and $t \in [0, T]$, the $\mathbf{k}$-ω spectrum $P(\mathbf{k}, \omega)$ is obtained via a fast Fourier transform (FFT) $P = |\mathcal{F}\{\zeta\}|^2$. To obtain the DSV at a given wavenumber k_j, the spectrum is first masked to contain only data from wavenumbers in a small range around k_j, giving

$$F_j(\mathbf{k}, \omega) = \begin{cases} \sqrt{P(\mathbf{k}, \omega)} & \text{for} \quad |k - k_j| \leq \tilde{\Delta} k \\ 0 & \text{else} \end{cases}, \tag{3.26}$$

whereby a cylinder shell of thickness $2\tilde{\Delta}k$ is cut from the measured spectrum, centered around the ω-axis. If $\tilde{\Delta}k$ is chosen appropriately, the DSV is practically constant $\tilde{\mathbf{c}}(k) \approx \tilde{\mathbf{c}}(k_j)$ within the cylinder shell, labelled $\tilde{\mathbf{c}}_j$. In order to retrieve $\tilde{\mathbf{c}}_j$ from the masked spectrum using the dispersion relation Equation (3.4), a characteristic function is defined

$$G_j(\mathbf{k}, \omega; \tilde{\mathbf{c}}_j) = G_j^+(\mathbf{k}, \omega; \tilde{\mathbf{c}}_j) + G_j^-(\mathbf{k}, \omega; \tilde{\mathbf{c}}_j), \tag{3.27}$$

with[5]

$$G_j^{\pm}(\mathbf{k}, \omega; \tilde{\mathbf{c}}_j) = \exp\left[-2\left(\frac{\pm\omega_{\mathrm{DR}}(\pm\mathbf{k}, \tilde{\mathbf{c}}_j) - \omega}{a_\omega}\right)^2\right]. \tag{3.28}$$

G can be understood as the dispersion cone ω_{DR} for a background current $\tilde{\mathbf{c}}_j$, broadened in the ω-direction with a width factor a_ω (a normalization constant is not required). Finally, the overlap between the characteristic

[5] The definition for $G^{\pm}$ given in *Article II* contains a sign error. However, it only affects G at negative frequencies, which were excluded from the DSV extraction step, since that part of the spectrum is redundant. Therefore, the sign error in G took no effect. In *Article III* the correct definition for $G^{\pm}$ is given.

function G_j and the masked spectral data F_j is quantified in terms of the NSP $N_j(\tilde{\mathbf{c}})$

$$N_j(\tilde{\mathbf{c}}) = \frac{\langle G_j F_j \rangle}{\langle G_j \rangle \langle F_j \rangle}, \tag{3.29}$$

where

$$\langle f \rangle = \iiint f(\mathbf{k}, \omega) \, \mathrm{d}\omega \, \mathrm{d}^2 k \,. \tag{3.30}$$

From maximizing N_j by varying $\tilde{\mathbf{c}}$, the best fit is found and $\tilde{\mathbf{c}}_j$ is obtained.

Numerically, the integrals are calculated as full summations of the 3D arrays, where G_j is evaluated on the $\mathbf{k}$-ω-grid on which the spectrum F is known, and the product $G_j F_j$ is the pointwise multiplication of the corresponding arrays. For the optimization procedure maximizing $N_j(\tilde{\mathbf{c}})$ a Nelder-Mead simplex algorithm (Lagarias et al. 1998) is used, which is included in the function library of most common programming and data analysis tools.

3.3.2 Spectral Leakage

When obtaining the spectrum from a measurement using a discrete Fourier transformation (DFT), most spectral components will exhibit spectral leakage (Lyon 2009). It is a consequence of the finite sample size, say, the duration T, as this truncation of the underlying "real" time series of infinite duration is effectively a multiplication with a top hat function of length T. In Fourier space this is equivalent to a convolution of the real signal's spectrum with a sinc function $\mathrm{sinc}(fT) = \sin(fT\pi)/(fT\pi)$, causing the spectral intensity from one frequency component to appear at other frequencies as well.

The effect of this "leakage" can be divided into two components. First, the most leakage appears in a small range around the real frequency, within a range determined by the first root of the sinc function, usually referred to as the central lobe. For a top hat function, or window, the width of the central lobe is $\Delta f = 2/T$. The larger issue from spectral leakage, however, comes from the second component. At frequencies multiple central lobe widths Δf away, the magnitude of spurious spectral intensity is still significant, since the sinc function decays only as $1/f$.

To mitigate the long–range effect of spectral leakage, the measurement data can be multiplied with a window function $w(t)$ prior to any subsequent analysis. This effectively replaces the top-hat with the window of choice, thus replacing the sinc Fourier space with the Fourier transform of $w(t)$. Depending on the precise window $w(t)$, a faster decay of spurious spectral intensity at large f can be achieved, at the cost of an increase in the central lobe

width Δf (see, e.g., Nuttall 1981). Thus, the choice of the window function depends on the application at hand; it is typically a trade-off between long-range and short-range spectral leakage.

In the data analysis reported in *Article III*, a Hann window was used, as it is a very common choice and has a reasonably narrow central lobe while providing good long-range leakage suppression. A more detailed discussion regarding the influence of spectral leakage on the extraction of DSVs can be found in *Article II*.

3.3.3 DSV Extraction Parameters

For reliable results, it is important to choose appropriate width parameters $\tilde{\Delta}k$ and a_ω. Small widths typically increase the susceptibility to noise, while large widths tend to smooth over these influences.

From a test case with waves on quiescent water it was found that the wavenumber bin width $\tilde{\Delta}k$ effectively acts as the width of a moving average, smoothing the extracted DSVs $\tilde{\mathbf{c}}(k)$ as expected. This is desirable if the measure spectrum is noisy. A reasonable compromise was found to be $\tilde{\Delta}k = 2\delta k$, where δk is the wavenumber resolution.

In contrast, the second parameter a_ω can have a more complex impact on the resulting DSVs. Ideally a_ω should be set such that G (see Equation (3.28)) approximates the ω-distribution of the measured spectral intensity. A larger width makes the NSP insensitive to changes in $\tilde{\mathbf{c}}$, increasing the influence of spurious spectral intensity at frequencies distant from the dispersion relation. However, reducing a_ω can result in the optimization procedure finding a local maximum within the range where spectral intensity is expected, instead of the center of gravity thereof. This can lead to strong fluctuations in the extracted DSVs when the spectrum is noisy.

The choice of a_ω for the studies presented in *Article II* and *Article III* is based on different considerations. Since *Article II* is a study on the effect of spectral leakage, a_ω is set such that the characteristic function G well encompasses the central lobe of the applied window function's Fourier transform. *Article III* is a study on the effect of horizontal shear, which leads to broadening typically larger than that due to spectral leakage. Therefore, a_ω is set such that G encompasses the maximum frequency spread expected within the domain; it is estimated using the current spread ΔU and the highest input wavenumber, $\Delta\omega \sim k_{\max}\Delta U$.

3.3.4 DSV Statistics and Visualization

It is worth considering how to visualize the statistics of the extracted DSV vectors $\tilde{\mathbf{c}}$. A straightforward approach is to plot the mean $\langle ... \rangle$ and standard deviation σ, e.g., using error bars, for the components of $\tilde{\mathbf{c}}$ separately. These are calculated across realizations (indicated by subscript r) as follows. Let N_r be the number of realizations and $i_r = \{1, 2, .., N_r\}$, then

$$\langle \mathrm{X} \rangle = \frac{1}{N_r} \sum_{i_r=1}^{N_r} \mathrm{X}_{i_r} \quad \text{and} \quad \sigma^2[\mathrm{X}] = \frac{1}{N_r - 1} \sum_{i_r=1}^{N_r} (\mathrm{X}_{i_r} - \langle \mathrm{X} \rangle)^2, \tag{3.31}$$

where X is either $\tilde{c}_x$ or $\tilde{c}_y$, the respective x- and y-component of $\tilde{\mathbf{c}}$. The wavenumber index j is suppressed for brevity; the mean and standard deviation are understood to be calculated for each j.

An alternative is to show the statistics of $\tilde{c}$ in terms of $\langle \tilde{c} \rangle = \langle |\tilde{\mathbf{c}}| \rangle$ and $\sigma[\tilde{c}]$ instead. In addition, information about the direction $\vartheta_{\tilde{c}}$ of $\tilde{\mathbf{c}}$ must be provided. The angle $\vartheta_{\tilde{c}}$ is obtained as the direction of the average DSV (not the average of directions)

$$\vartheta_{\tilde{c}} = \arg\left(\langle \tilde{\mathbf{c}} \rangle\right) \qquad \left(\neq \langle \arg(\tilde{\mathbf{c}}) \rangle \right). \tag{3.32}$$

This approach requires more panels to show the magnitude and direction of the DSV, but significantly improves their readability, especially when results for different scenarios — especially current directions — are shown in the same figure for comparison. To showcase the advantage of the second method of visualization, the DSVs extracted for waves atop a current with directions $\theta_U = -90°,\ 0°, 90°$ are shown in Figure 3.3. The second method of plotting clearly facilitates the comparison of results. It is used for the presentation of data in *Article II* and *Article III*.

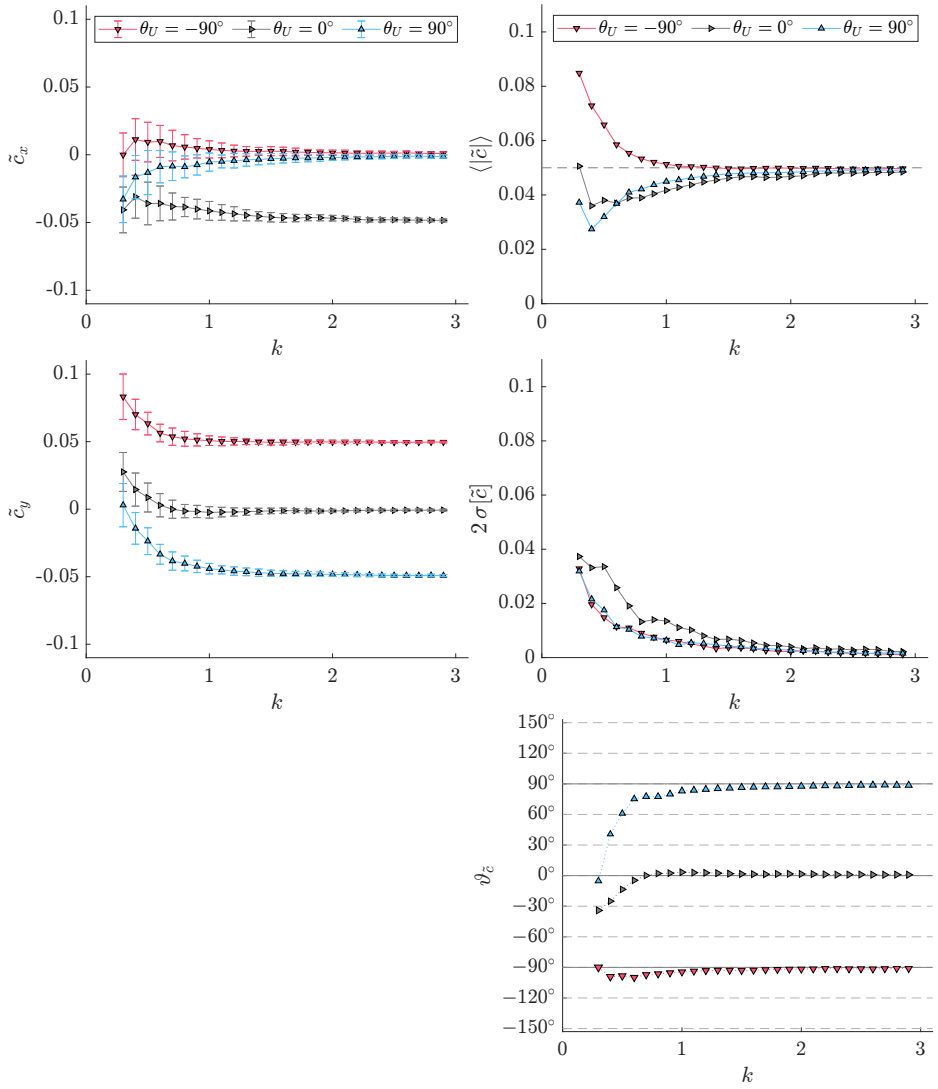

Figure 3.3: DSVs of waves atop a constant current background of strength $U = 0.05$ directions $\theta_U = -90°,\ 0°, 90°$ (indicated by color and marker). The two panels on the left show the Cartesian components of the DSV $\tilde{\mathbf{c}} = (\tilde{c}_x, \tilde{c}_y)$ in terms of the statistical mean (line) and standard deviation (error bar). The three panels on the right show the same results in terms of the statistical mean (top) of the magnitude of $\tilde{\mathbf{c}}$, its standard deviation (middle) and the average direction $\vartheta_{\tilde{c}}$ (bottom). Note how the right panels highlight biases in $\langle|\tilde{\mathbf{c}}|\rangle$ and $\vartheta_{\tilde{c}}$ for $k \to 0$.

4

Summary of Research Articles and Outlook

In this chapter the research articles included in this thesis are summarized and suggestions for future studies based on the findings of this thesis are given. The focus of this work is the investigation of systematic errors or biases in two measurement techniques commonly employed in the context of free water surface dynamics.

The first is the free surface synthetic schlieren (FS-SS) method due to Moisy et al. (2009), used mainly in laboratory experiments for measuring the water surface topography from camera images. In the standard setup (configuration 1), the camera is placed above the water surface and a random dot pattern below. From observed distortions of this pattern, the surface gradient, and hence the topography, can be reconstructed. This configuration has certain limitations that can be overcome with a different setup (configuration 2), where the camera is placed below the (transparent) bottom of the water container and the dot pattern above the surface. In Chapter 2 the relation between the surface gradient and the observed deformations of the dot pattern is derived for configuration 2, an equation similar in form to the one provided in Moisy et al. (2009) for configuration 1. Both derivations are based on first order approximations that assume small view angles and surface slopes as well as negligible surface elevations. Testing the limits of

these restrictions (see Section 2.2) it was found that the systematic errors in the recovered surface gradient are generally much higher in configuration 2, by up to an order of magnitude. However, by increasing the camera-pattern distance, the errors can be reduced to below 10%, even for a significant surface steepness of up to $\varepsilon \approx 0.3$. Errors stemming from a finite wave height were found to be less severe, exceeding 10% only for waves with amplitudes approaching half the pattern surface distance, clearly violating the small amplitude assumption.
For the surface measurements reported in *Article I*, the FS-SS was used in configuration 2, with distances $h_0 = 0.5\,\mathrm{m}$ (camera to bottom), $h_1 = 0.17\,\mathrm{m}$ (bottom to surface) and $h_2 = 0.17\,\mathrm{m}$ (surface to pattern), covering an area of $165\,\mathrm{mm} \times 165\,\mathrm{mm}$. The observed surface features were measured to have a maximum surface steepness of ~ 0.3 and surface elevation of $\sim 1\,\mathrm{cm}$. Consulting Figure 2.4 at $[h_0, h_1] = [1\,\mathrm{m}, 0.5\,\mathrm{m}]$, a maximum systematic error of less than 10 % in the calculated surface gradient is expected.

The second measurement technique is the Doppler shift velocity (DSV) extraction based on the normalized scalar product (NSP), used to infer subsurface flow speeds from spatiotemporal measurements of the surface elevation. It is based on the fact that for waves propagating atop a vertically sheared current, the frequencies have wavenumber dependent deviations from their quiescent water values. The goal of this part of the thesis is to investigate systematic errors in the extracted DSVs due to violation of the assumption that the background current is horizontally uniform. For a variety of scenarios, synthetic surface elevation data is generated and the DSVs extracted, as described in Chapter 3. Even in the absence of horizontal shear the extracted DSVs exhibit biases due to spectral leakage, as reported in *Article II*. With this knowledge, the biases due to horizontal shear are then identified, as shown in *Article III*.

Article I

The influence of grid-generated turbulent flows on the gas transfer rate across an air-water interface
Pim Bullee, Stefan Weichert, Astri Nore, Leon Li, Simen Å. Ellingsen and R. Jason Hearst
Submitted to *Experiments in Fluids*
A previous version of the article was accepted for publication in a peer-reviewed conference proceedings, but withdrawn due to excessive publication delays. The data analysis — mainly Section 3.1 — and writing in general have been improved and updated for the submission to Experiments in Fluids.

In this article, an experimental study of the transfer of oxygen through the air-water interface is presented, and an increase due to turbulence is quantified by varying the amount of turbulence generated using an active grid. To isolate the effect from turbulence in the water column, the surface elevation was recorded as well, using the FS-SS method in configuration 2. From the obtained surface gradient data, the wavevector-frequency spectra were calculated and an increase of spectral intensity representing surface waves was observed and attributed to up-stream generation. Their influence on the gas transfer rate was ruled out, however, because the increase in the interface's surface area was negligible.

Article II

Biases from spectral leakage in remote sensing of near-surface currents
Stefan Weichert, Benjamin K. Smeltzer and Simen Å. Ellingsen
IEEE Transactions on Geoscience and Remote Sensing, vol. **61**, pp. 1-15, 2023, Art no. 4208515

Article II lays the foundation for analyzing the effects of horizontal shear on the extraction of DSVs using the NSP method. Therein it is shown that for realistic scenarios without shear, spectral leakage can lead to false current "measurements" far exceeding resolution-based limits. Several factors have a big influence on the magnitude and wavenumber dependence of these biases: the wave spectrum's shape in terms of peakedness and angular spread, the background current strength and direction relative to the mean propagation direction of waves, and the spectral resolutions.

Finally, recommendations for identifying and reducing spectral leakage effects are given. Most notably, the application of a Hann window prior to the data analysis drastically reduces the errors. Additionally, sacrificing

frequency resolution for wavenumber resolution was found to be beneficial in most cases.

Article III

The effect of horizontal shear in extracting near-surface currents from wave data

Stefan Weichert, Benjamin K. Smeltzer and Simen Å. Ellingsen
Submitted to *IEEE Transactions on Geoscience and Remote Sensing*

In this article, biases due to horizontal shear are investigated. The background current varies linearly in strength and has constant direction. As in *Article II*, sea states of different mean propagation direction and angular spread are considered. For highly directional wave spectra the biases in the extracted DSVs can reach 100% of the expected domain average, depending strongly on the relative direction between waves, current and current gradient, as well as the amount by which the current changes within the field of view.

A mitigation strategy, involving the following steps, is given. First, the directionality of the wave spectrum is determined. A very narrow angular spread of less than 40° (full width) indicates the possibility of biases due to horizontal shear. Second, the data analysis is repeated with a reduced domain size, which likely leads to a smaller range of currents in the domain, the main factor for these kind of biases. If the resulting DSVs differ from the those obtained with the full-size domain, it is advisable to look more closely at the spectra at constant wavenumber to inspect how well the fits of the dispersion relation matches the spectral data.

Concluding Remarks

The FS-SS method gives access to the time resolved surface topography of the air-water interface in laboratory experiments. Therefore, it can be used for validating modifications of, or new remote current sensing techniques, as demonstrated by Smeltzer et al. (2019). Hence, it may play an important role in the ecosystem of developing measurement techniques in the future. In this context, as well as in other experimental studies of interactions between sheared currents, waves and turbulence, one may require water depths that render the FS-SS unusable in the standard configuration, due to too large distortions of the dot pattern at the water bottom. In the flipped geometry, the sensitivity is tunable due to the the variable distance between the dot pattern and the free surface, which restores its applicability. This increased flexibility comes at the cost of larger errors stemming from the added refracting surface at the bottom of the tank. In the paraxial limit, the errors in both configurations vanish, but in practice the assumptions that the method is based on may be fulfilled only to a certain degree. Errors from partially fulfilling, or even violating these assumptions are controllable, but care must be taken to avoid them. The method's applicability is broader than initially expected and only very strongly sloped surfaces pose an issue that cannot be overcome with changes to the setup.

For measuring near-surface currents on scales up to the submesoscale, remote sensing has become an indispensable tool. The spectral analysis of optical footage from airborne observations is especially attractive due to the speed at which data can be obtained from large areas. Additionally, other quantities can be measured at the same time, e.g. the sea-surface-temperature (Lenain et al. 2023, Romero et al. 2017), increasing the potential value of this approach further. Of particular interest are areas of rapid changes in the ocean currents, such as fronts and eddies. It is such regions, however, where biases from horizontal shear must be expected. Furthermore, the directional wave spectrum changes, e.g., across submesoscale fronts VreĆica et al. (2022) or due to internal gravity waves Lenain and Pizzo (2021). This may exacerbate the biases, as they depend strongly on the wave spectrum (mostly angular spread), and the relative direction between wave propagation, current and the current's gradient.

It should be noted that the biases investigated in this work appear mostly for very narrow spectral spread, or long-crested waves. Thus, in most cases, the method is reliable, but it is recommended to always monitor the wave spectrum.

Future Work

As with essentially all research, the work presented in this thesis leaves some questions open and raises new ones. Further attention to the topics given below would provide valuable additional insight.

1 **Short distance FS-SS:** A violation of the small angle approximation leads to large systematic errors, particularly in configuration 2. When restrictions of the experimental setup do not allow for moving the camera further away, a higher order relation between the surface gradient and measured displacements that reduces these errors would certainly prove useful. If such a relation cannot be found analytically, one can use the simulation approach presented herein to find an empirical polynomial which minimizes expected errors for the setup at hand.

2 **Adaptive NSP parameters for subsurface current measurements:** Long range spectral leakage effects on the DSV extraction using the NSP method are effectively removed by tapering the surface elevation data with a Hann window. Influences from short range leakage, on the other hand, continue to cause biases in the DSVs at small wavenumbers. A mitigation strategy would be to use adaptive parameters in the NSP method that take into account the effective broadening of the spectrum signal in frequency, due to leakage in the wavenumber direction, strongest at low wavenumbers. Similarly, when horizontal current ranges can be estimated from preliminary measurements, the NSP parameters can be adapted to accommodate for the frequency broadening due to shear, strongest at high wavenumbers.

3 **Additional case studies:** The biases due to spectral leakage and horizontal shear presented in this thesis were investigated under certain simplifying assumptions. Relaxing these may give rise to additional effects, for instance, from a bimodal input spectrum or a background current that changes direction either horizontally or vertically. Additionally, the so far directly used surface elevation data could be converted into more realistic image sequences with proper lighting and shadows.

4 **Wave reflection effects:** For certain combinations of the wave spectrum and background current, caustics emerge for part of the spectrum, which cannot be handled by the simulation code of this work. Such cases may lead to interesting results. For instance, whether a wave is reflected by the current depends strongly on the wave's propagation direction. Then, in one part of the domain, waves from the full input spectrum are present, while only a reduced spectrum is measurable in another part.

Bibliography

I. Amidror. Scattered data interpolation methods for electronic imaging systems: a survey. *Journal of Electronic Imaging*, 11(2):157 – 176, 2002. doi: 10.1117/1.1455013.

S. Banihashemi and J. T. Kirby. Approximation of wave action conservation in vertically sheared mean flows. *Ocean Modelling*, 143:101460, 2019. ISSN 1463-5003. doi: 10.1016/j.ocemod.2019.101460.

J. Campana, E. J. Terrill, and T. de Paolo. The development of an inversion technique to extract vertical current profiles from X-band radar observations. *J. Atmos. Oceanic Technol.*, 33:2015–2028, 2016. doi: 10.1029/JC086iC07p06481.

J. R. Dormand and P. J. Prince. A family of embedded Runge-Kutta formulae. *J. Comput. Appl. Math.*, 6(1):19–26, 1980. doi: 10.1016/0771-050X(80)90013-3.

J. P. Dugan and C. C. Piotrowski. Surface current measurements using airborne visible image time series. *Remote Sens. Environ.*, 84:309–319, 2003. doi: 10.1016/S0034-4257(02)00116-5.

S. Å. Ellingsen and Y. Li. Approximate dispersion relations for waves on arbitrary shear flows. *Journal of Geophysical Research: Oceans*, 122(12): 9889–9905, 2017. doi: 10.1002/2017JC012994.

D. M. Fernandez, J. F. Vesecky, and C. Teague. Measurements of upper ocean surface current shear with high-frequency radar. *J. Geophys. Res.*, 101(C12):28,615–28,625, 1996. doi: 10.1029/96JC03108.

R. Gangeskar. Verifying high-accuracy ocean surface current measurements by X-band radar for fixed and moving installations. *IEEE Transactions on Geoscience and Remote Sensing*, 56(8):4845–4855, 2018. ISSN 0196-2892 1558-0644. doi: 10.1109/tgrs.2018.2840133.

M. Gerber. The interaction of deep-water gravity waves and an annular current: linear theory. *Journal of Fluid Mechanics*, 248:153–172, 1993. doi: 10.1017/S0022112093000722.

D. S. Goodman. *General Principle of Geometrical Optics*. Handbook of Optics: Volume I - Geometrical and Physical Optics, Polarized Light, Components and Instruments. McGraw-Hill Education, New York, 3rd edition edition, 2010. ISBN 9780071498890.

G. M. Hale and M. R. Querry. Optical constants of water in the 200-nm to 200-μm wavelength region. *Appl. Opt.*, 12(3):555–563, Mar 1973. doi: 10.1364/AO.12.000555.

K. Hessner, K. Reichert, J. C. N. Borge, C. L. Stevens, and M. J. Smith. High-resolution X-Band radar measurements of currents, bathymetry and sea state in highly inhomogeneous coastal areas. *Ocean Dyn.*, 64:989–998, July 2014. doi: 10.1007/s10236-014-0724-7.

W. Huang and E. Gill. Surface current measurment under low sea state using dual polarized X-band nautical radar. *IEEE J. Sel. Topics Appl. Earth Observ. in Remote Sens.*, 5:1868–1873, 2012. doi: 10.1109/JSTARS.2012.2208179.

W. Huang, R. Carrasco, C. Shen, E. W. Gill, and J. Horstmann. Surface current measurements using x-band marine radar with vertical polarization. *IEEE Transactions on Geoscience and Remote Sensing*, 54(5):2988–2997, 2016. doi: 10.1109/TGRS.2015.2509781.

Y. Jooss, L. Li, T. Bracchi, and R. J. Hearst. Spatial development of a turbulent boundary layer subjected to freestream turbulence. *Journal of Fluid Mechanics*, 911:A4, 2021. doi: 10.1017/jfm.2020.967.

A. Joseph. *Measuring ocean currents: tools, technologies, and data*. Newnes, 2013. ISBN 9780123914286.

J. T. Kirby and T.-M. Chen. Surface waves on vertically sheared flows: Approximate dispersion relations. *Journal of Geophysical Research: Oceans*, 94(C1):1013–1027, 1989. doi: 10.1029/JC094iC01p01013.

M. Klaus and D. Vachon. Challenges of predicting gas transfer velocity from wind measurements over global lakes. *Aquat. Sci.*, 82:53, 2020. doi: 10.1007/s00027-020-00729-9.

J. Kolaas, B. H. Riise, K. Sveen, and A. Jensen. Bichromatic synthetic schlieren applied to surface wave measurements. *Experiments in Fluids*, 59(8):128, Jul 2018. ISSN 1432-1114. doi: 10.1007/s00348-018-2580-6.

V. Kotwicki. Water balance of earth / bilan hydrologique de la terre. *Hydrological Sciences Journal*, 54(5):829–840, 2009. doi: 10.1623/hysj.54.5.829.

J. C. Lagarias, J. A. Reeds, M. H. Wright, and P. E. Wright. Convergence properties of the nelder-mead simplex method in low dimensions. *SIAM J. Optim.*, 9:112–147, 1998. doi: 10.1137/S1052623496303470.

N. J. M. Laxague, T. M. Özgökmen, B. K. Haus, G. Novelli, A. Shcherbina, P. Sutherland, C. M. Guigand, B. Lund, S. Mehta, M. Alday, and J. Molemaker. Observations of near-surface current shear help describe oceanic oil and plastic transport. *Geophysical Research Letters*, 45(1): 245–249, 2018. doi: doi.org/10.1002/2017GL075891.

L. Lenain and N. Pizzo. Modulation of surface gravity waves by internal waves. *Journal of Physical Oceanography*, 51(9):2735 – 2748, 2021. doi: 10.1175/JPO-D-20-0302.1. URL https://journals.ametsoc.org/view/journals/phoc/51/9/JPO-D-20-0302.1.xml.

L. Lenain, B. K. Smeltzer, N. Pizzo, M. Freilich, L. Colosi, S. Å. Ellingsen, L. Grare, H. Peyriere, and N. Statom. Airborne remote sensing of upper-ocean and surface properties, currents and their gradients from meso to submesoscales. *Geophysical Research Letters*, 50(8):e2022GL102468, 2023. doi: 10.1029/2022GL102468.

B. Lund, H. C. Graber, H. Tamura, C. O. Collins III, and S. M. Varlamov. A new technique for the retrieval of near-surface vertical current shear from marine X-band radar images. *J. Geophys. Res.*, 120:8466–8484, 2015. doi: 10.1002/2015JC010961.

B. Lund, B. K. Haus, J. Horstmann, H. C. Graber, R. Carrasco, N. J. M. Laxague, G. Novelli, C. M. Guigand, and T. M. Özgökmen. Near-surface current mapping by shipboard marine X-band radar: a validation. *J. Atmos. Oceanic Technol.*, 35:1077–1090, 2018. doi: 10.1175/JTECH-D-17-0154.1.

D. A. Lyon. The discrete Fourier transform, part 4: spectral leakage. *Journal of object technology*, 8(7), 2009. doi: 10.5381/jot.2009.8.7.c2.

W. D. McKee. Waves on a shearing current: a uniformly valid asymptotic solution. *Mathematical Proceedings of the Cambridge Philosophical Society*, 75(2):295–301, 1974. doi: 10.1017/S0305004100048490.

J. C. McWilliams. Submesoscale currents in the ocean. *Proceedings of the Royal Society A: Mathematical, Physical and Engineering Sciences*, 472 (2189):20160117, 2016. doi: 10.1098/rspa.2016.0117.

F. Moisy, M. Rabaud, and K. Salsac. A synthetic schlieren method for the measurement of the topography of a liquid interface. *Experiments in Fluids*, 46(6):1021–1036, Jun 2009. ISSN 1432-1114. doi: 10.1007/s00348-008-0608-z.

F. Moisy, G.-J. Michon, M. Rabaud, and E. Sultan. Cross-waves induced by the vertical oscillation of a fully immersed vertical plate. *Physics of Fluids*, 24(2):022110, 02 2012. ISSN 1070-6631. doi: 10.1063/1.3686696.

A. Nuttall. Some windows with very good sidelobe behavior. *IEEE Transactions on Acoustics, Speech, and Signal Processing*, 29(1):84–91, 1981. doi: 10.1109/TASSP.1981.1163506.

D. Peregrine. Interaction of water waves and currents. volume 16 of *Advances in Applied Mechanics*, pages 9–117. Elsevier, 1976. doi: 10.1016/S0065-2156(08)70087-5.

O. Phillips. *The Dynamics of the Upper Ocean*. Cambridge Monographs on Mechanics. Cambridge University Press, 1980. ISBN 9780521298018.

W. J. Pierson. Wind generated gravity waves. volume 2 of *Advances in Geophysics*, pages 93–178. Elsevier, 1955. doi: 10.1016/S0065-2687(08)60312-X.

L. Romero, L. Lenain, and W. K. Melville. Observations of surface wave–current interaction. *Journal of Physical Oceanography*, 47(3):615 – 632, 2017. doi: 10.1175/JPO-D-16-0108.1. URL https://journals.ametsoc.org/view/journals/phoc/47/3/jpo-d-16-0108.1.xml.

R. Savelsberg and W. Van de Water. Experiments on free-surface turbulence. *Journal of Fluid Mechanics*, 619:95–125, 2009. doi: 10.1017/S0022112008004369.

C. M. Senet, J. Seeman, and F. Ziemer. The near-surface current velocity determined from image sequences of the sea surface. *IEEE Trans. Geosci. Remote Sens.*, 39(3):492–505, 2001. doi: 10.1109/36.911108.

F. Serafino, C. Lugni, and F. Soldovieri. A novel strategy for the surface current determination from marine x-band radar data. *IEEE Geoscience and Remote Sensing Letters*, 7(2):231–235, 2010. doi: 10.1109/LGRS.2009.2031878.

B. K. Smeltzer. Current_inversion_ntnu, 2022. URL https://github.com/bsmeltzer/Current_Inversion_NTNU.

B. K. Smeltzer, E. Æsøy, A. Ådnøy, and S. Å. Ellingsen. An improved method for determining near-surface currents from wave dispersion measurements. *Journal of Geophysical Research: Oceans*, 124(12):8832–8851, 2019. doi: 10.1029/2019JC015202.

H. Socquet-Juglard, K. Dysthe, K. Trulsen, H. E. Krogstad, and J. Liu. Probability distributions of surface gravity waves during spectral changes. *Journal of Fluid Mechanics*, 542:195–216, 2005. doi: 10.1017/S0022112005006312.

T. Steinmann, M. Arutkin, P. Cochard, E. Raphaël, J. Casas, and M. Benzaquen. Unsteady wave pattern generation by water-striders. *Journal of Fluid Mechanics*, 848:370–387, 2018. doi: 10.1017/jfm.2018.365.

R. H. Stewart and J. W. Joy. Hf radio measurements of surface currents. *Deep Sea Research and Oceanographic Abstracts*, 21(12):1039–1049, 1974. ISSN 0011-7471. doi: 10.1016/0011-7471(74)90066-7.

M. Streßer, R. Carrasco, and J. Horstmann. Video-based estimation of surface currents using a low-cost quadcopter. *IEEE Geoscience and Remote Sensing Letters*, 14(11):2027–2031, 2017. ISSN 1545-598X. doi: 10.1109/LGRS.2017.2749120.

J. R. Taylor and A. F. Thompson. Submesoscale dynamics in the upper ocean. *Annual Review of Fluid Mechanics*, 55:103–127, 2023. ISSN 1545-4479.

L. N. Thomas, A. Tandon, and A. Mahadevan. *Submesoscale Processes and Dynamics*, pages 17–38. American Geophysical Union (AGU), 2008. ISBN 9781118666432. doi: doi.org/10.1029/177GM04.

A. Voronovich. Close propagation of internal and surface gravity waves in the approximation of geometrical optics. *Izv. Atmos. Ocean. Phys*, 12: 850–857, 1976.

T. VreĆica, N. Pizzo, and L. Lenain. Observations of Strongly Modulated Surface Wave and Wave Breaking Statistics at a Submesoscale Front. *Journal of Physical Oceanography*, 52(2):289–304, Feb. 2022. doi: 10.1175/JPO-D-21-0125.1.

S. Weichert, B. K. Smeltzer, and S. Å. Ellingsen. Biases from spectral leakage in remote sensing of near-surface currents. *IEEE Transactions on Geoscience and Remote Sensing*, 61:1–15, 2023. doi: 10.1109/TGRS.2023.3321305.

B. S. White and B. Fornberg. On the chance of freak waves at sea. *Journal of Fluid Mechanics*, 355:113–138, 1998. doi: 10.1017/S0022112097007751.

G. B. Whitham. *Water Waves*, chapter 13, pages 431–484. John Wiley and Sons, Ltd, 1999. ISBN 9781118032954. doi: 10.1002/9781118032954.ch13.

S. Wildeman. Real-time quantitative schlieren imaging by fast fourier demodulation of a checkered backdrop. *Experiments in Fluids*, 59(6):97, May 2018. ISSN 1432-1114. doi: 10.1007/s00348-018-2553-9.

I. R. Young and W. Rosenthal. A three-dimensional analysis of marine radar images for the determination of ocean wave directionality and surface currents. *J. Geophys. Res.*, 90:1049–1059, 1985. doi: 10.1029/JC090iC01p01049.

Article I

The influence of grid-generated turbulent flows on the gas transfer rate across an air-water interface

Pim Bullee, Stefan Weichert, Astri Nore, Leon Li, Simen Å. Ellingsen and R. Jason Hearst

Submitted to
Experiments in Fluids

This paper is submitted for publication and is therefore not included.

Article II

Biases from spectral leakage in remote sensing of near-surface currents

Stefan Weichert, Benjamin K. Smeltzer and Simen Å. Ellingsen

Accepted manuscript

Stefan Weichert, Benjamin K. Smeltzer and Simen Å. Ellingsen. Biases from spectral leakage in remote sensing of near-surface currents, *IEEE Transactions on Geoscience and Remote Sensing*, vol. **61**, pp. 1-15, 2023, Art no. 4208515, doi: 10.1109/TGRS.2023.3321305

Biases from spectral leakage in remote sensing of near-surface currents

Stefan Weichert, Benjamin K. Smeltzer, Simen Å. Ellingsen

***Abstract*—Remotely measuring subsurface water currents from imagery of the wave field has become a much-used technique. We study the biases and errors in such measurements due to spectral leakage, and suggest mitigating procedures. Deviations between peak values in the three-dimensional wave spectrum and the known dispersion relation in quiescent water are extracted and interpreted as current-induced Doppler shifts, from which the sub-surface current is inferred. The use of discrete Fourier transforms, however, introduces spectral leakage between nearby frequency bins. Analysing synthetically generated wave data adhering to realistic input spectra we show that although no current is in fact present, spurious currents can be "measured" which can amount to a significant fraction of the phase speed at the spectral peak. We analyse the effects of data tapering, method of Doppler shift extraction, limited wavenumber and frequency resolution, peakedness and angular width of the input spectrum, and average misalignment between waves and Doppler shift velocity direction. The narrower the input wave spectrum in frequency and/or direction, the greater the biases become. The use of a window function reduces the severity in nearly all cases, yet mitigates the effects of limited resolution more effectively in space than in time. When a current is present the absolute biases remain essentially unchanged, when waves and currents are roughly aligned, whereas in the case of a cross-current, biases remain significant even for tapered data.**

I. Introduction

The prospect of measuring currents near the sea surface remotely from above is a highly attractive one. Measuring depth-varying currents *in situ* by penetrating the surface requires the use of e.g. buoys, ships, gliders or fixed instruments, all relatively expensive and able to measure a single point or trajectory at a time, and often struggle to capture currents in the top few metres. In comparison, remote measurement from above can be performed with inexpensive equipment mounted on airborne platforms able to cover larger areas in a short time (see, e.g., [1]).

By far the most common source of wave data has been measurements using HF or X-band radar [2]–[16], primarily mounted on ships. Only observation of the wave phase variation in time and space is required, however, meaning other methods are equally applicable; the use of infrared [17] and polarimetric [18], [19] imaging has been demonstrated, as has regular optical measurements (video) with cameras mounted on quadcopter drones [20], and aircraft [21]–[24].

A current varying with depth will affect the wave phase velocity differently for different wavelengths, resulting in a measurable effective Doppler shift which depends on wavenumber [2] and appears as a shift in the waves' spectral dispersion curve from that observed in quiescent water. Ever more advanced methods have been developed in recent years for inferring the depth profile of the sub-surface currents from such measured Doppler shifts [12], [25], [26], yet the task of obtaining these shifts from an observation of the spatiotemporal wave field, by reconstructing the current-modified dispersion surface in the frequency-wavenumber spectrum, is itself a nontrivial task. Typically, the spectrum is divided into wavenumber magnitude bins, whereby the Doppler shifts are found for each bin separately. Perhaps the most frequently employed are least-squares-based methods (e.g. [4], [8], [27]), whereas the alternative Normalized Scalar Product (NSP) method is also in regular use (e.g. [10], [13], [28]). We compare these methods herein finding NSP to be unequivocally favourable. A further method which we shall not consider here is the so-called Polar Current Shell method (e.g. [13]), recently adapted for this purpose [26], which has similar performance as NSP, but favourable in some circumstances.

One should note that the same questions we seek to answer here, also apply to bathymetry retrieval from the measured wave spectra (see e.g. [29] and references therein). The extraction of the water depth from the measured spectrum requires spectral intensity at low wavenumbers, which can be strongly influenced by spectral leakage, as we will show. Since a finite water depth enters the dispersion relation in a direction-independent and multiplicative way in contrast to the additive and anisotropic term due to a current, it is not obvious how the issues discussed herein affect the bathymetry retrieval quantitatively, a question of potential importance which requires further investigation.

A. Outline

In this work we consider the effects of a strong spectral energy peak and the corresponding effect it has on the extraction of Doppler shifts for wavenumbers in the vicinity of the peak. The energy peak results in spectral leakage to adjacent wavevectors in the wave spectrum and may cause errors in the extracted Doppler shifts — as perhaps the clearest example we show that in realistic seastates, spectral leakage can cause a significant spurious current to be "measured" when none is in fact present.

The work of S. Å. Ellingsen was supported in part by the European Union (ERC, WaTurSheD, project 101045299) and the Research Council of Norway (project 325114). Views and opinions expressed are however those of the authors only and do not necessarily reflect those of the European Union or the European Research Council. Neither the European Union nor the granting authority can be held responsible for them.

S. Weichert and S. Å. Ellingsen are with the Department of Energy and Process Engineering, Norwegian University of Science and Technology, 7491 Trondheim, Norway.

B. K. Smeltzer is with SINTEF Ocean, Marinteknisk senter, 7052 Trondheim, Norway

The phenomenon of spectral leakage is briefly reviewed in section II-B, and we discuss how it can be mitigated by data windowing. We then go on to describe a numerical experiment where mock wave data is generated and analysed with the methods in standard use for remote-sensing of currents from wave dispersion, in section III. Results are reported studying how the spurious current "measurements" depend on the method of Doppler shift extraction (section III-C), the angular width and peakedness of a directional (JONSWAP [30]) wave spectrum (sections VI-B and VI-C), the spatial and temporal resolution (sections VI-D and VI-D), as well as how the situation changes when a uniform background current is present, in section VI-E. We finally summarize and give a brief overview of ways whereby the detrimental effect of spectral leakage can be reduced in practical applications, in section VII.

II. Background

When remote sensing of sub-surface currents from wave dispersion is performed, the input spectrum is an observation of the motion of the water surface resolved in time and space. The method is based on linear wave theory, so only the phase of the waves is required, not the amplitude. The data is typically a monotonic function of the sea surface elevation or its derivative, as a function of position (x, y) and time t. A three dimensional Fourier transform is then applied in space and time to obtain a spectral signal as a function of wave numbers $\boldsymbol{k} = (k_x, k_y)$ and frequency ω. We assume the spatial area and duration of the observation are $L \times L$ and T, respectively, so that the resolution in wavenumber and frequency are, respectively, $\delta k = 2\pi/L$ and $\delta\omega = 2\pi/T$; we will refer to these as a pixel or bin in wavenumber and frequency, respectively. (Note that after we introduce nondimensional units in section III-A δk and $\delta\omega$ take the forms $1/L$ and $1/T$, respectively.) We will assume infinitely deep water for simplicity herein.

A. Theory

In a wave spectrum, the spectral signal is concentrated near the dispersion relation $\omega = \omega_{\text{DR}}(\boldsymbol{k})$. The methods for sensing the sub-surface current now extract a measured function $\omega(\boldsymbol{k})$. If a current with moderately strong depth-dependence $\boldsymbol{U}(z) = (U(z), V(z))$ is present, the dispersion relation for a wave with wave vector $\boldsymbol{k}$ is well approximated as $\omega = \omega_{\text{DR}}(\boldsymbol{k}; \tilde{\boldsymbol{c}})$ with the dispersion function

$$\omega_{\text{DR}}(\boldsymbol{k}; \tilde{\boldsymbol{c}}) = \omega_0(k) + \boldsymbol{k} \cdot \tilde{\boldsymbol{c}} \tag{1}$$

where $k = |\boldsymbol{k}|$, $\tilde{\boldsymbol{c}}$ is the Doppler shift velocity (DSV) due to the presence of a sub-surface current and the dispersion relation in deep, quiescent water is

$$\omega_0(k) = \sqrt{gk}. \tag{2}$$

Inversion methods to infer depth-dependent velocity profiles from the measured spectrum are based on the approximation [2], [31]

$$\tilde{\boldsymbol{c}} = 2k \int_{-\infty}^{0} \boldsymbol{U}(z) e^{2kz} dz. \tag{3}$$

If a current is present which is uniform in depth, the resulting Doppler shift will be independent of $\boldsymbol{k}$, while conversely, a Doppler shift which varies with $\boldsymbol{k}$ implies the presence of a current which varies as a function of z. We shall see that biases in the measured Doppler shift $\tilde{\boldsymbol{c}}$ due to spectral leakage typically vary significantly with $\boldsymbol{k}$, and hence the spurious currents which are "measured" will have a nontrivial depth dependence. We do not pursue this question in detail.

The presence of the current thus introduces an observable Doppler shift corresponding to the addition of a phase speed $\tilde{\boldsymbol{c}}(k)$ to the phase velocity. Remote sensing of the depth-varying current $\boldsymbol{U}(z)$ is then possible by measuring $\tilde{\boldsymbol{c}}$ and inverting equation (3) using one of several methods available as reviewed in [1]. Methods for extracting $\tilde{\boldsymbol{c}}$ from a measured spectrum are reviewed and compared in section III-C.

Following Smeltzer et al. [26] we define the instructive quantities $\delta c_{\delta\omega}$ and $\delta c_{\delta k}$ as

$$\delta c_{\delta\omega} = \frac{\delta\omega}{k}; \quad \delta c_{\delta k} = \frac{\partial\omega}{\partial k}\frac{\delta k}{k}, \tag{4}$$

which estimate the change in the predicted phase velocity c due to moving the dispersion surface (1) by δk along the wavenumber axis in the spectrum, or by $\delta\omega$ along the frequency axis. These are thus approximate measures of the uncertainty in velocity measurement introduced by limited wavenumber and frequency resolution, respectively. Further discussion may be found in section 4.2.1 of [26].

B. Spectral leakage and windowing

Assume a continuous signal (in space or time) $\tilde{P}_0(t)$, the "true" signal, is measured during a finite period of duration T. A sharp cut-off at the beginning and end of the measurement is equivalent to multiplying $\tilde{P}_0$ by a discontinuous top-hat function $w_{\text{box}}(t)$ which is 1 within a time interval of length T and zero outside this "window". Multiplication with such a window is equivalent to a convolution of the spectrum $P_0 = \mathcal{F}\{\tilde{P}_0\}$ with a sinc function in frequency space (e.g. [32]),

$$P_{\text{measured}}(f) = P_0(f) * T\,\text{sinc}(fT), \tag{5}$$

where $\text{sinc}(a) = \sin(\pi a)/\pi a$, which is the Fourier transform of the top hat function. The result is a blurring of the spectrum: "true" spectral components will appear as spectral intensity not only in the frequency bins closest to the actual frequency of said component, but also on neighbouring ones that are more than one bin away, with an intensity decreasing with distance. One can alleviate this by replacing the "box" window with a window of choice, simply by multiplying the acquired data $\tilde{P}(t) = \tilde{P}_0 w_{\text{box}}(t)$ with said window function $w(t)$. If the chosen $w(t)$ also vanishes outside the measurement interval, the window replaces the top-hat. The choice of the optimal window function much depends on the situation and data at hand.

The Fourier transforms $\mathcal{F}\{w\}(f)$ of some common window functions are shown in figure 1 (See e.g. [33] for a more comprehensive comparison). When taking a discrete Fourier transform (DFT) of $w(t)$ every real frequency component f will generate spectral intensity in frequency bins of width

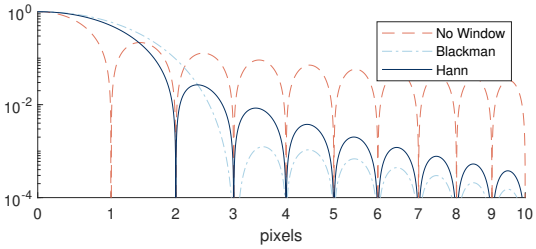

Fig. 1. Fourier transform $\mathcal{F}\{w\}(f)$ of a selection of common window functions $w(t)$. A frequency pixel is $\delta\omega = 2\pi/T$, normalized so that $\mathcal{F}\{w\}(0) = 1$. This illustrates how long-range spectral leakage can be mitigated by tapering the measured signal. The drawback of increased short-range leakage (1-2 pixels) is often negligible.

δf centered at $n\delta f$, $n \in Z$, with intensity $\mathcal{F}\{w\}(n\delta f - f)$. For example, for the *Blackman window* shown in figure 1, a frequency coinciding with a DFT frequency, i.e. $f = m\delta f$, one obtains non-zero spectral intensity only for $n - m = 0, 1, 2$, leading to no long-range leakage whatsoever. Only the central lobe is sampled in frequency space. For any real spectrum most frequencies will not coincide with a DFT frequency, and so the side-lobes give rise to long-range leakage. Now, the central lobe of the *No Window* (or top hat) case is only one pixel wide, but the leakage is very long-range, i.e. spectral intensity decays slowly and stays well above 1% for more than 20 pixels. In contrast to this, the *Blackman* window decays rapidly to 10^{-3}, at the cost of increasing spectral leakage into the two nearest bins, 1 and 2. The best choice of the windowing function is usually a compromise between suppressing long-range leakage and blurring the spectrum (short-range leakage). In this work, a Hann window, defined as

$$w_{\mathrm{H}}(t) = 0.5 - 0.5\,\cos\left(2\pi\, t/T\right), \tag{6}$$

is used, as it suppresses the long-range spectral leakage to less than 1% and leaks significantly into frequencies less than two pixels away. In appendix A an example of extracted DSVs with different windowing functions is given to illustrate how the choice affects the results.

The data in this work is surface elevation $\zeta(x, y, t)$ measured in three dimensions x, y and time t, which we pre-multiply by a 3D Hann window constructed as $w(x, y, t) = w_{\mathrm{H}}(x)w_{\mathrm{H}}(y)w_{\mathrm{H}}(t)$ prior to subjecting it to a discrete 3-dimensional fast-Fourier transform (3DFFT). The new signal $\zeta(x, y, t)w(x, y, t)$ goes smoothly to zero at the edges of the domain of observation, in our case the square area with sides L and time duration T.

III. Methods

We proceed by producing synthetic surface elevation data $\zeta(x, y, t)$ by superposing random linear plane waves of wave number k and direction θ from chosen spectra with varying properties, as detailed in section III-B. Each wave is given a uniformly distributed random initial phase, the frequency ω is found from equation (1), whereupon the waves are propagated in time.

These wave "observations" are of course idealized, since different methods for obtaining the actual surface elevation $\zeta(x, y, t)$ or true spectrum from field data each come with their individual challenges and limitations, an ongoing field of research in its own right. Taking such practical challenges into account is beyond the scope of this work, and we use the ideal data to isolate the effects of spectra leakage in the data analysis.

We mostly consider the case of quiescent water, i.e., there is no background current and any Doppler shifts "measured" from the spectrum are spurious and purely a consequence of spectral leakage. We also consider the case where a constant background current $\boldsymbol{U}_0$ is present, in section VI-E. Biases now manifest as deviations of the observed DSVs from the correct value.

A. Dimensional basis

Dimensional quantities will be denoted by a superscript asterisk, all other quantities are non-dimensionalized. The reference length-scale and time-scale are defined based on a characteristic wavenumber k_0^* and its corresponding angular frequency in quiescent water $\omega_0^* = \sqrt{gk_0^*}$. Thus, e.g. $T = T^*\omega_0^*/2\pi$, $L = L^*k_0^*/2\pi$, $k = k^*/k_0^*$, $\omega = \omega^*/\omega_0^*$, $U = U^*\sqrt{k_0^*/g}$. Unless specified otherwise, $\omega_0^*(k_0^*)$ is taken to be the location of the peak of the energy spectrum, hence the peak in wavenumber space is close to to $k = 1$.

B. Wave spectrum

We generate wave fields from commonly used realistic model spectra with varying directional broadness, assuming the form

$$\hat{S}(\omega, \theta) = S(\omega)f(\theta) \tag{7}$$

where θ is the angle between $\boldsymbol{k}$ and the x axis, $\cos\theta = \boldsymbol{k}\cdot\boldsymbol{e}_x/k$. We use the JONSWAP spectrum [30]

$$S(\omega) = \tilde{N}\omega^{-5}\exp\left[-\frac{5}{4}\omega^{-4}\right]\gamma^{r(\omega)} \tag{8}$$

with

$$r(\omega) = \exp\left[-\frac{1}{2}\left(\frac{\omega - 1}{\sigma}\right)^2\right]. \tag{9}$$

For our purposes the value of $\tilde{N}$ is not of importance, we set $\tilde{N} = 1$. The parameter σ is

$$\sigma = \begin{cases} 0.07, & \text{if } \omega \leq \omega_p, \\ 0.09, & \text{if } \omega > \omega_p \end{cases} \tag{10}$$

and the peakedness parameter γ is varied (see section VI-C). The energy spectrum for a selection of peakedness values γ is depicted in figure 2. The angular distribution is taken as a cosine-square with a full width (distance of first roots) of $\Delta\theta$, i.e.

$$f(\theta) = \begin{cases} \cos^2\left(\pi\frac{\theta - \theta_0}{\Delta\theta}\right) & , |\theta - \theta_0| \leq \Delta\theta/2 \\ 0 & \text{else} \end{cases} \tag{11}$$

We use this spectrum to prescribe the amplitudes $a(\boldsymbol{k})$ of the superposed wave components in accordance with [34] as

$$a(\boldsymbol{k}) = \sqrt{2\,k^{-3/2}\,\hat{S}(\omega(k), \theta)\delta k} \tag{12}$$

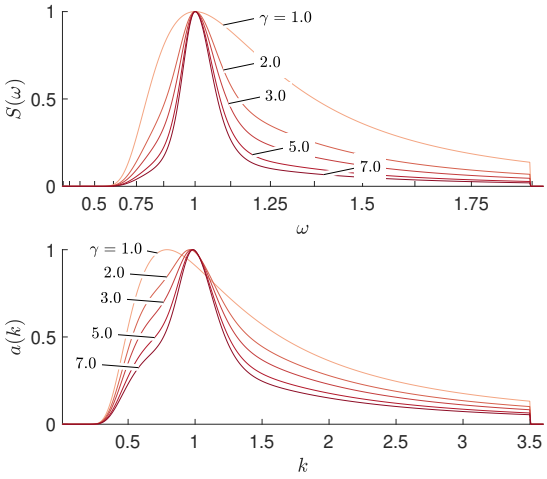

Fig. 2. Top: Energy spectrum $S(\omega)$ (equation 8) for a few values of the peakedness parameter γ. The ω axis is scaled quadratically to match the range of the bottom graph, as $k = \omega^2$. Bottom: amplitudes $a(k, \theta = \theta_0)$ (equation 12) of superposed wave components. The spectra are normalized with respect to their peak value.

on an evenly spaced grid in k_x-k_y, with spacing $\delta k_x = \delta k_y = \delta k$. Additionally, we set $a(\boldsymbol{k})$=0 for $k/k_p > 3.5$.

C. Normalized scalar product

Two methods are in common use for extracting Doppler shifts from the measured wave spectrum; least-squares (LS) methods (e.g. [4], [8], [27]) and the Normalized Scalar Product (NSP) method (e.g. [10], [13], [28]). While there exists a wide range of extensions and sophistications to LS methods, we focus our attention on the NSP method. However, since two of the most famous works on spectrum based current extraction ([4], [8]) use a simple form of the LS method we also give a brief comparison of their performance in appendix C.

We employ the DSV extraction method as implemented by Smeltzer et al. [26]; see [10], [13], [28] for details on the NSP method more generally.

The starting point in either method is a measured, spatio-temporally resolved free-surface $\eta(x, y, t)$ and its power spectrum obtained via a discrete Fourier transform, $P(\boldsymbol{k}, \omega) = |FFT[\eta(x, y, t)]|^2$. For each wavenumber k_i in a list, the spectral intensity on a cylindrical surface with radius k_i centered around the ω-axis is defined

$$F_i(\boldsymbol{k}, \omega) = \sqrt{P(k_i \cos\theta, k_i \sin\theta, \omega)}. \tag{13}$$

where θ is the azimuth angle in the k_x-k_y-plane. The implementation of the algorithms used are formulated in Cartesian coordinates; however, it is illustrative to use cylindrical coordinates for the following conceptual considerations. More details of the implementation are given in appendix B.

To find the effective DSV $\tilde{\boldsymbol{c}}_i = \tilde{\boldsymbol{c}}(k_i)$, first, a characteristic function G is defined that contains the components of $\tilde{\boldsymbol{c}}_i$ as free parameters:

$$G_i(\theta, \omega; \tilde{\boldsymbol{c}}_i) = G_i^+(\theta, \omega; \tilde{\boldsymbol{c}}_i) + G_i^-(\theta, \omega; \tilde{\boldsymbol{c}}_i) \tag{14}$$

where

$$G_i^{\pm}(\theta, \omega; \tilde{\boldsymbol{c}}_i) = \exp\left[-2\left(\frac{\omega \pm \omega_{\mathrm{DR}}(\theta; k_i, \tilde{\boldsymbol{c}}_i)}{a}\right)^2\right]. \tag{15}$$

The normalized scalar product N_i of the vectors F_i and G_i is now maximized for each value of i by varying the two components of $\tilde{\boldsymbol{c}}_i$; it is calculated as

$$N_i(\tilde{\boldsymbol{c}}) = \frac{\langle G_i F_i \rangle}{\langle G_i \rangle \langle F_i \rangle} \tag{16}$$

where $\langle ... \rangle$ refers to an integral over all θ and ω. In other words, G_i can be thought of as a cosine in θ (see figure 4) with offset $\omega_0(k_i)$ amplitude $k_i \tilde{c}$ and phase shift defined by the direction of $\tilde{\boldsymbol{c}}$; its overlap with the measured intensity on the cylinder surface is maximized to find the best DSV $\tilde{\boldsymbol{c}}(k_i)$. This optimization step is performed using the Nelder-Mead simplex method [35].

IV. The normalized scalar product method and spectral leakage

For multidimensional data, spectral leakage is most prominent in the directions parallel to the coordinate axes. Consider for example a 2D signal $\eta(x, y)$ on a rectangular domain and its Fourier transform $\tilde{\eta}(k_x, k_y) = \mathcal{F}\{\eta\}$. Since both x and t are within a finite range, the effective window $w(x, y)$ is a product of top-hat windows in the x and y directions, respectively, i.e. $w = w_1(x)w_2(y)$. The Fourier transform of such a product is the product of their respective Fourier transforms $\tilde{w}(k_x, k_y) = \mathcal{F}\{w_1(x)\}\mathcal{F}\{w_2(y)\} = \tilde{w}_1(k_x)\tilde{w}_2(k_y)$. Now, since the leakage for a top-hat window falls off as $1/k$, the product $\tilde{w}(k_x, k_y)$ is smallest for a given k when $|k_x| = |k_y|$ and largest when $k_x = 0$ or $k_y = 0$. An illustration of this can be seen in figure 3. The extension to 3 or more dimensions is straightforward.

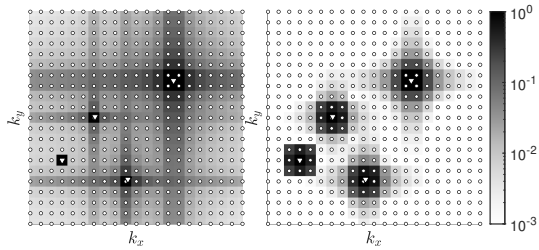

Fig. 3. An illustration of spectral leakage in two dimensions. Left: Logarithmic 2D FFT spectrum of a superposition of four sine-waves, with frequencies denoted by triangles. The circles denote the DFT frequencies, i.e. frequencies natural to the domain. From left to right, the leftmost spectral peak coincides with a DFT frequency, while the rightmost peak lies in the middle of DFT frequencies. Right: same as left, bit with a 2D Hann window applied before doing the FFT. Note how the Hann window removes the background and increases consistency between spectral peak, while broadening by roughly one bin in all directions.

This (mostly) axes-parallel leakage is helpful in understanding how leakage affects the DSV extraction using NSP.

A fundamental step in the NSP method is to pick out measured spectral intensity on a cylinder surface with radius k_i. One can think of the effect on the NSP as the spectral intensity

projecting itself in the principal directions onto the cylinder, with decreasing intensity the further the surface is from the originating spectral intensity. Now, as the NSP method essentially fits a function of the form $\omega_0(k_i) + A_f \cos(\theta - \theta_f)$, with free parameters A_f and θ_f, to the spectral intensity on the cylinder surface defined by k_i, as illustrated in figure 4, spurious intensity at $\omega \neq \omega_0(k_i)$ leads to non-zero values for $A_f = \boldsymbol{k} \cdot \tilde{\boldsymbol{c}}$, implying a background current even in the absence of one. In this work we consider spectra with a single peak at a given wave vector $\boldsymbol{k} = (k_x, k_y)$.

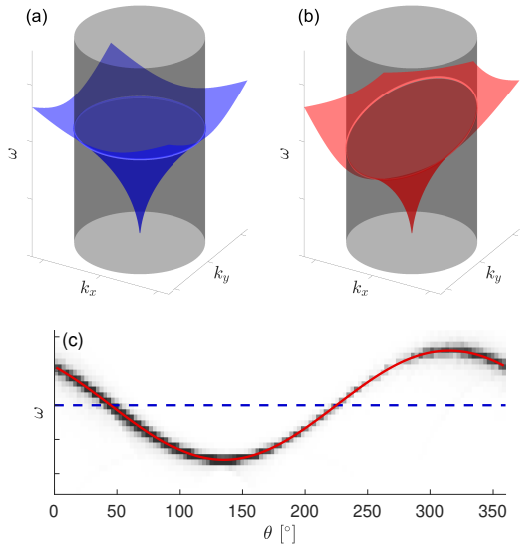

Fig. 4. Illustration of the dispersion relation $\omega = \omega_{\mathrm{DR}}(\boldsymbol{k}; \tilde{\boldsymbol{c}})$ in connection within the Nonlinear Scalar Product method. The top graphs show the dispersion relation in absence of a current, $\tilde{\boldsymbol{c}} = 0$ (a) and with a current, $\tilde{\boldsymbol{c}} = \boldsymbol{U}_0$ (b). The intersections with a cylinder with radius k_i is highlighted. In graph (c) the spectral intensity is indicated in greyscale, visible near the dispersion curve on the cylinder surface after unrolling it, together with the lines of intersection from the top figures: blue, dashed corresponds to quiescent water; red, solid is the best fit from the NSP method resulting in a non-vanishing Doppler shift velocity.

We now consider the effect of spectral leakage for two distinct cases, one (1) with the mean propagation direction θ_0 being parallel to the k_y-axis, and one (2) with θ_0 between $0°$ and $90°$.

A. *Leakage for* $\theta_0 = 90°$

Consider the extraction of the DSV for a wavenumber $k < 1$, i.e. below the peak of the spectrum. The spectral leakage for the cylinder with radius k will be dominated by short-range spectral leakage of wavenumbers close to k and long-range leakage from the spectral peak. the short-range spectral leakage for the most part will just blur the spectral intensity on the cylinder, while the long-range leakage from the spectral peak leads to a new, possibly dominating, spectral intensity spot on the cylinder, at the same angle, but a higher frequency. In other words right above the real spectral intensity. Depending on the ratio of intensities, distance, and width of the characteristic function G, the NSP algorithm may find the correct frequency, the frequency of the projected peak or a value in between these two to give the best fit. Therefore the returned DSV will be parallel to the spectrum propagation direction θ_0. Similarly, if $k > 1$ is considered, the projection from the spectral peak will be below the real spectral intensity, giving DSV antiparallel to the spectrum propagation direction θ_0.

B. *Leakage for* $0 < \theta_0 < 90°$

For $k < 1$, it is now possible for spectral leakage from the peak to have no axes-parallel projection onto the cylinder surface, thus not affecting the extracted DSV for this wavenumber. Short-range spectral leakage and leakage from lower wavenumbers now dominate, making the prediction of DSV direction difficult. For $k > 1$, one can still get an intuition for the effect of leakage. As the peak of the spectrum lies in the first quadrant of the $k_x - k_y$-plane, the shortest distance to a cylinder with radius k is to the quarter of the cylinder also lying in the first quadrant, and we can focus our consideration on that. The leakage is now being projected onto the cylinder at an angle relative to the mean propagation direction θ_0. Therefore, as the real spectral intensity now dominates for $\theta = \theta_0$, the frequency for wavenumbers along θ_0 is found correctly. The perpendicular component of the DSV, however is determined mostly by the position and relative magnitude of the spurious intensity appearing at angles $\theta \neq \theta_0$. in quiescent water, for example, one would obtain DSVs with directions $\theta \pm 90°$.

Note that these considerations hold true for very narrow spectra, but are to be understood as tendencies for spectra with considerable spectral width $\Delta\theta$, because, for any angle θ, real spectral intensity will mostly dominate over spectral leakage, if present.

V. Parameter Choice and Overview

For an overview and easier referencing table I contains the list of test cases presented in this paper. Apart from the parameters stated therein, the resolution of the input spectrum $\delta_{in}k$ and spatial resolution $\delta x = \delta y$ as well as temporal resolution δt had to be set. The spatial resolution was chosen such that waves of the highest wavenumbers, $k_{max} = 4$, would be well resolved, $\delta x = 1/28$. Similarly, time resolution was set to $\delta t = 1/14$. The resolution of the input spectrum was set to $\delta_{in}k \approx 0.341/L$, with L being the domain size. This was deemed small enough to mimic a continuous spectrum.

The domain size and video duration were chosen to be close to typical parameters found in airborne measurements [36]. The resulting videos in their work typically have a field of view of $L^* = 128 - 512\,\mathrm{m}$, durations of $T^* = 20 - 40\,\mathrm{s}$ and wavenumbers with usable spectral intensity from 0.2 to $2\,\mathrm{rad\,m^{-1}}$ (see figure 1 in [36]). Taking a reference wavenumber of $k_0^* = 0.4\,\mathrm{rad\,m^{-1}}$, this gives a parameter range of $T \approx 5 - 10$, $L \approx 8 - 32$.

Equation 14 contains one free parameter, a, that determines the width of the characteristic function. We set $a = 4\,\delta\omega$, with

	θ_0	$\Delta\theta$	γ	L	T	U	figure	section
case-NSP-LS	75°	60°	3.3	10	20	0	11	C
case-θ_0-$\Delta\theta$	60°, 90°	15°...60°	3.3	10	20	0	5	VI-A,VI-B
case-γ	60°	15°...60°	1...7	10	20	0	6	VI-C
case-L-T	90°	60°	3.3	5, 10, 20	10, 20, 80	0	7	VI-D
case-U	90°	60°	3.3	10	20	0...0.15	8, 9	VI-E

TABLE I

OVERVIEW OF PARAMETER COMBINATIONS. θ_0: MEAN PROPAGATION DIRECTION OF INPUT WAVENUMBER SPECTRUM, $\Delta\theta$: ANGULAR SPREAD OF INPUT WAVENUMBER SPECTRUM (SEE EQUATION 11), γ: PEAKEDNESS PARAMETER (SEE EQUATION 8), L: DOMAIN SPATIAL DOMAIN SIZE, T: VIDEO DURATION, U: BACKGROUND CURRENT. ALL PARAMETERS ARE NON-DIMENSIONAL, SEE SECTION III-A

$\delta\omega = 1/T$ being the frequency resolution (see appendix B for details).

The results shown in figures 5-9 display statistics of the extracted DSVs in terms of the average $\langle|\tilde{\boldsymbol{c}}|\rangle$ and the corresponding standard deviation $\sigma_{\tilde{c}}$ (times two for illustrative purposes), calculated from 100 realizations. These quantities are useful as they represent a mean bias and fluctuation that one has to expect from a single measurement. Additionally, where possible, the implied velocity resolutions $\delta c_{\delta\omega}$ and $\delta c_{\delta k}$ defined in equation (4) are shown for reference.

VI. RESULTS

In this section we consider the effects of wave-spectral properties, resolution and data tapering on the spurious Doppler shifts "measured" when no current is present, as well as the effect of a uniform current being present. An overview of the parameter combinations used to obtain the following results is given in section V.

A. Illustration of the effect of windowing (Hann window)

To see the influence of the angular spread $\Delta\theta$ of the wavenumber spectrum, simulations with variation both in $\Delta\theta$ and the mean propagation direction θ_0 were performed (see table I, case-θ_0-$\Delta\theta$, for all parameters). A selection of the results are shown in figure 5 (upper row). A more detailed discussion of the influence of $\Delta\theta$ and θ_0 is given in section VI-A below.

The propagation direction θ_0 shows a strong influence on both the mean bias and its variation. This behaviour is likely due to spectral leakage, because spectral leakage appears as "streaks" in the spectrum along the spectral axes k_x, k_y and ω (See illustration in figure 3). The second column in figure 5 shows the extracted DSVs of tapered surface elevation data. The mean and random bias is strongly suppressed in all cases and the dependency on θ_0 is significantly reduced, compared to the analysis without a Hann window. Note that $\Delta\theta = 15°$ represents a rare, very narrow spectrum, but the described effects are visible for all spectral widths, decreasing with increasing $\Delta\theta$.

We observe that for smaller wavenumbers ($k < 1$), using a Hann window does not mitigate the effects of spectral leakage as strongly as for $k > 1$. This is because the Hann window suppresses long-range spectral leakage (more than one-two pixels), while increasing the short-range spectra leakage (The central lobe of the Hann window has a width of 2 bins instead of 1 for no-window). The "steepness" $\partial\omega/\partial k$ grows with decreasing k, meaning that spectral intensity that leaks in the k-direction appears as a strong broadening in the ω-direction at neighbouring k-values. In our simulations the spectrum has a peak at $\omega = 1$ (thus close to $k = 1$) and quickly decreases towards $k \approx 0.5$. Therefore, the combined effects of a steep slope in the energy spectrum and the dispersion relation cause the short-range spectral leakage to be most prominent for $k < 1$.

The effect of a steep spectral slope — discussed further in section VI-C — can be illustrated by considering that at, say, $k = 0.6$ the spectrum shows intensity at $\omega_0(0.6)$, but also intensity leaked from $\omega_0(0.6+\delta k)$ and $\omega_0(0.6-\delta k)$, the latter of which is much less than the former. The algorithm therefore finds a frequency between $\omega_0(0.6)$ and $\omega_0(0.6+\delta k)$, which gives a non-zero DSV (see also section IV).

B. Influence of the mean propagation direction and angular spread

To study the influence of the angular width on the mean and random bias in the extracted DSVs, simulations were run with three propagation directions $\theta_0 \in \{90°, 75°, 60°\}$ and a range of spectral widths $\Delta\theta$, of which two representative examples, $(15°, 60°)$, are shown in figure 5 (see table I, case-θ_0-$\Delta\theta$, for all parameters).

All cases show that an increase in spectral width $\Delta\theta$ significantly decreases both mean and random biases across all wavenumbers. Results for $\Delta\theta > 60°$ are not shown here, as no notable further improvements were observed.

The reduction in angular spread $\Delta\theta$ leads to an increase in spurious DSVs $\tilde{\boldsymbol{c}}$, because the wave components of a narrow spectrum are mostly influenced by the current component parallel to the mean propagation direction θ_0. The narrower a spectrum is, the smaller an observable change in frequency due to the perpendicular current component $\tilde{\boldsymbol{c}}_\perp$ becomes. Therefore, the influence of false spectral intensity from any source (e.g. noise, aliasing, higher harmonics, spectral leakage) outside the real spectrum can lead to strong perpendicular DSV components when the spectrum is very narrow. For a more detailed explanation, see section 5. Here we see the combined influence of a noisy spectrum and spectral leakage.

Note, that all cases exhibit negligible spurious DSVs around $k \approx 1$. This is simply a consequence of the spectral peak lying near this value.

The dependency of results on the mean propagation direction θ_0 was also investigated in a second manner: The videos were rotated numerically by angles θ_{rot} up to $45°$ before repeating the DSV extraction. This is equivalent to rotating the camera in an experiment. Pairwise comparison of results with same values of $\theta_0 + \theta_{\text{rot}}$ show no significant difference.

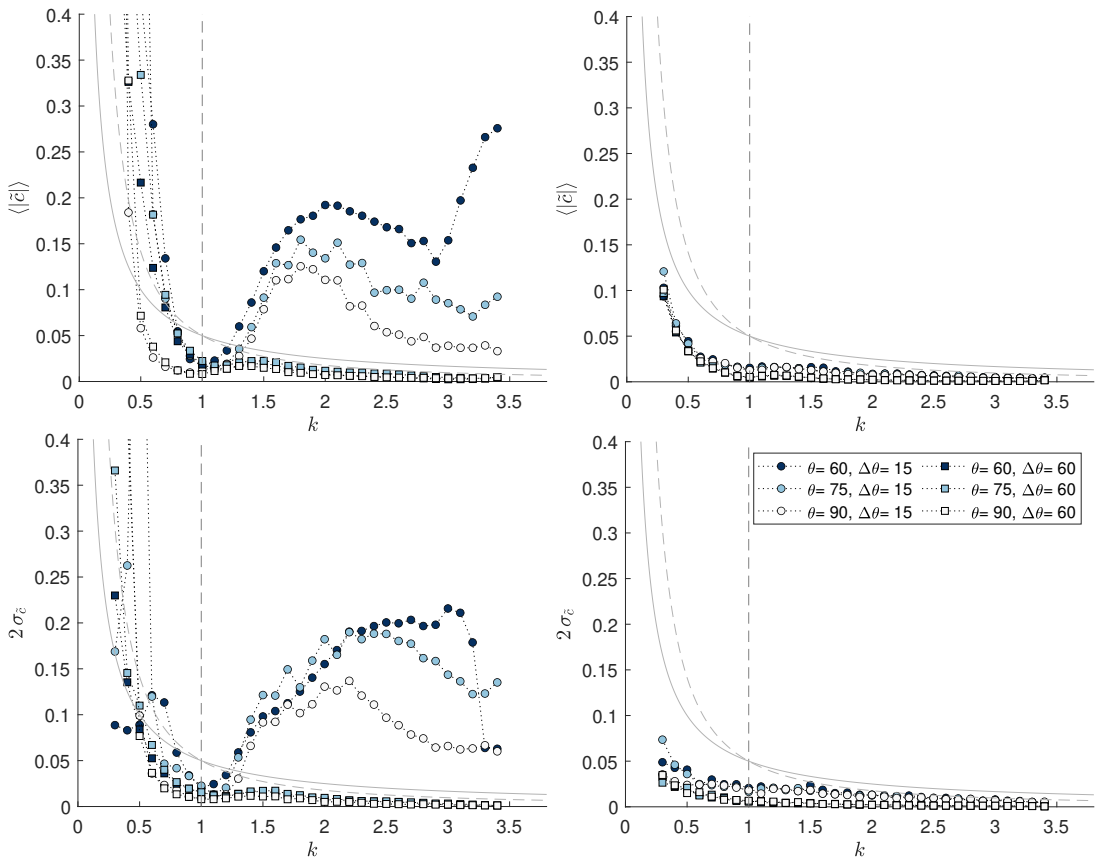

Fig. 5. Doppler shift velocities (DSV) $\bar{\mathbf{c}}$ for the parameter set case-θ_0-$\Delta\theta$ (see table I) extracted using the NSP method. The DSVs were extracted for 100 realizations with (right) and without (left) applying a Hann window beforehand. The top and bottom graphs show the biases in DSVs in terms of the average (top) and standard deviation (bottom) of the absolute value $\bar{c} = |\bar{\mathbf{c}}|$. The solid and dashed line correspond to the velocity resolutions implied by frequency and wavenumber resolution, respectively.

Two conclusions can be drawn: First, since the only reference direction is provided by the coordinate system in absence of a background current, θ_0-dependencies can be traced back to spectral leakage, which mainly occurs parallel to the axes, thus breaking rotational symmetry. Second, rotating the camera or data provides a useful check for spectral leakage.

The use of a Hann window prior to DSV extraction greatly mitigates the effects of spectral leakage, as discussed before, pushing even the narrow spectrum cases down to sub-resolution (with respect to implied velocity resolutions $\delta c_{\delta\omega}$ and $\delta c_{\delta k}$).

C. Influence of peakedness γ

Depending on how developed a sea is, the best fit for the frequency spectrum uses a peak enhancement factor γ between 1 and 7, where 3.3 is a commonly used value for most applications [37]. Recently, Mazzaretto et al. found that a global mean of $\gamma \approx 2.4$ is better suited [38].

Since the choice of γ only affects the spectrum in a small range around the peak, it also offers itself as a tool to examine the influence of steep gradients in the spectrum. We therefore compare the DSVs for $\gamma \in \{1...7\}$. (see table I, case-γ, for all parameters)

The results presented in figure 6 show that for spectra with small angular spread, a more strongly peaked spectrum (higher value for γ) causes increased biases (mean and random) across all wavenumbers except for a small range around the spectral peak at $k \approx 1$, where the relative increase in spectral intensity reduces the influence of spectral leakage from wavenumbers $k \neq 1$. A wider angular spread of the spectrum, on the other hand, mitigates this to a large degree, especially towards higher wavenumbers, where the influence of spectral leakage from the peak is nearly eliminated and sub-resolution biases are achieved. For angular spreads larger than $\Delta\theta > 45°$, the DSVs become independent of $\Delta\theta$, though this also changes with spectral resolution.

Towards lower wavenumbers ($k < 1$), without a Hann

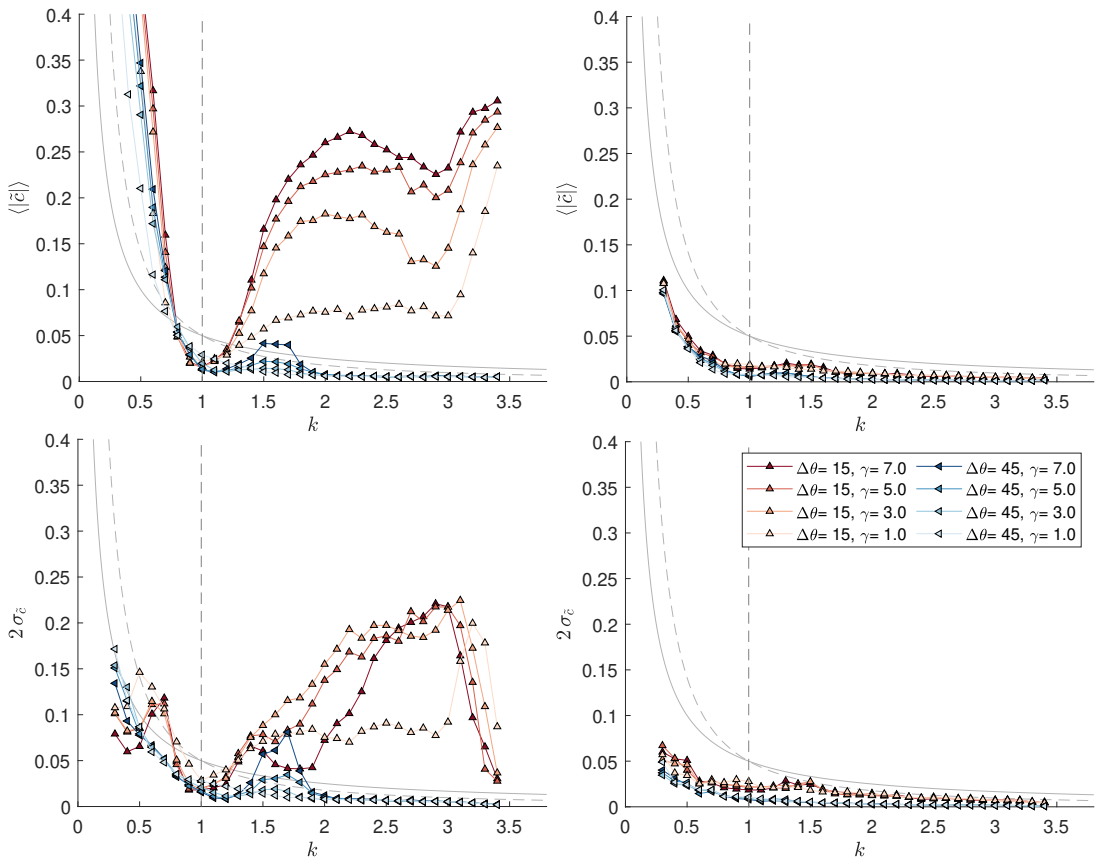

Fig. 6. Same as figure 5 but with parameter set case-γ (see table I).

window, any extracted DSV is unreliable, as spectral leakage dominates the result due to the exponential decrease of "real" spectral intensity towards $k = 0.5$ and the steepness of the dispersion relation (see previous discussion in section VI-A).

As for results before, the use of a Hann window improves the results so far that random and mean biases are sub-resolution even for strongly peaked ($\gamma = 7$), narrow ($\Delta\theta = 15°$) spectra, effectively eliminating the dependence on $\Delta\theta$, and to a degree, resolutions (see section VI-D).

D. Influence of resolutions δk, $\delta\omega$

The range of spectral leakage is constant in terms of pixels or bins, and thus the range in k (and ω) is determined by the resolution δk (and $\delta\omega$).

We therefore vary the spatial size L and temporal duration T of the videos to change the frequency resolution $\delta\omega = 1/T$ and wavenumber resolution $\delta k = 1/L$ to observe their influence on the DSV extraction (see table I, case-L-T, for all parameters).

For a spectrum with an angular spread of $\Delta\theta = 60°$ and a mean propagation direction of $\theta_0 = 90°$ simulations were performed with a range of video lengths $T = 5 - 80$ and domain sizes $L = 5 - 20$. The resulting DSVs are shown in figure 7. (Note that the results for $T < 10$ are not shown as they did not show relevant differences compared with results for $T = 10$)

Clearly, for untapered data, both improving δk or $\delta\omega$ reduces the biases in DSVs, albeit improving the wavenumber resolution δk has a stronger influence.

Note how the maximum in biases moves to higher k with decreasing T. This is due to the characteristic function G having a width a proportional to frequency resolution, $a = 4\delta\omega$. When this width is reduced, the intensity that leaks from the spectral peak onto the cylinder at $k > 1$ can fall outside the reach of the characteristic function, thus reducing or removing its influence.

When the data is tapered using a Hann window, this effect is mostly eliminated, as the long-range spectral leakage is heavily suppressed. Moreover, the influence of frequency resolution $\delta\omega$ is strongly reduced (graphs of same color group together).

An exception to rule of thumb that longer videos are always better can be seen for the longest videos $T = 80$ on the smallest domain $L = 5$. Here, the biases are actually greater

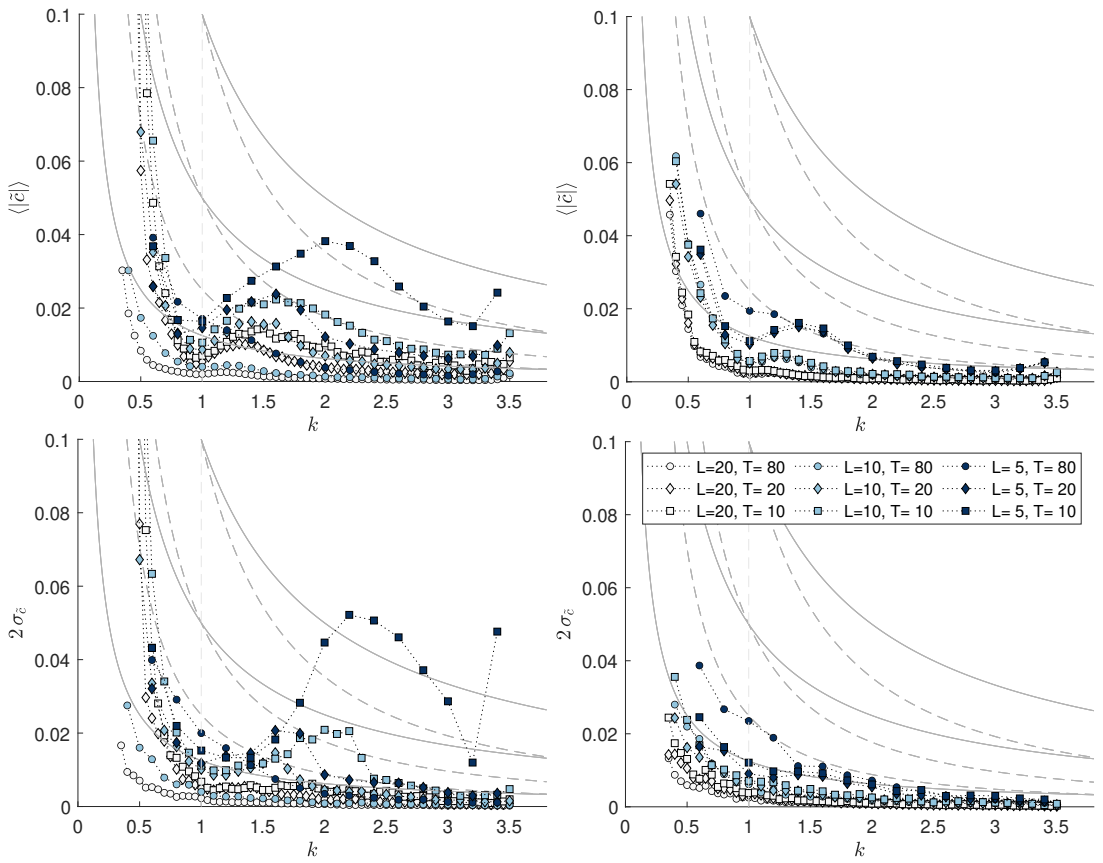

Fig. 7. Same as figure 5 but with parameter set case-L-T (see table I). As in figure 5 The solid and dashed lines correspond to the implied velocity resolutions from frequency and wavenumber resolution, respectively. From top to bottom the resolution increases, i.e. δw or δk become smaller.

than for the shorter cases with $T \leq 40$. This is due to the characteristic function becoming narrow enough to not encompass the width of spectral intensity in the ω-direction. In one dimension this would be proportional to $\delta\omega$, but in 2D or 3D can be dominated by leakage in k, as this effective broadening in ω scales with $\mathcal{O}(\partial\omega/\partial k\ \delta k) = \mathcal{O}(\delta k/\sqrt{k})$.

Note, however, that the results presented here all show biases well below the implied velocity resolutions, when the data is tapered using a Hann window. If one has to choose between increasing the domain size or the video duration, it is clear that an increase in domain size will give the most benefit.

E. Influence of a background current U_0

The cases shown above are without a background current. The presence of a uniform current $\boldsymbol{U} \neq 0$ breaks the rotational symmetry of the dispersion relation, because of the additional, angular dependent term $\boldsymbol{k} \cdot \boldsymbol{U}$.

To see the effect of a current on the biases in the extracted DSVs, we assume a (vertically and horizontally) constant current $\boldsymbol{U}$ with directions $\theta_U = 90°, 0°, -90°$ and current strengths in the range $|\boldsymbol{U}| = 0.025 - 0.15$. (see table I , case-$U$, for all parameters) The input wavenumber spectrum has an angular spread of $\Delta\theta = 60°$, and a peakedness of $\gamma = 3.3$, representing a realistic scenario. The mean propagation direction is held at $\theta_0 = 90°$, resulting in following, crossing and opposing current, respectively.

The extracted DSVs are shown in figure 8. For $k > 1$, we see a bias toward wave-opposing DSVs, while for $k < 1$, we see a bias toward wave-following DSVs. This can be seen from over-/underestimations for $\boldsymbol{U}$ antiparallel/parallel to the wave propagation direction, respectively. The absolute magnitude of errors is similar to the case of quiescent water (see section VI-D). In the case of a pure cross-current, however, this also results in a turning of the DSVs toward $\theta_{\tilde{c}} = \pm 90°$ for wavenumbers around the spectral peak $k \lesssim 1.5$, as can be seen in the third row of graphs in figure 8. Particularly, where the spectral intensity falls off to zero rapidly ($k \approx 0.5$), leakage from the peak of the spectrum can dominate the signal, biasing the direction of DSVs towards the propagation direction, i.e.

90°.

Tapering the data using a Hann window mitigates these biases in amplitude and direction as in the case of quiescent water. For a cross-current, however, the mean bias remains significant, i.e. on the order of 10% of the phase velocity at the spectral peak and unusually also in the vicinity of the spectral peak.

The error in the direction $\theta_{\tilde{c}}$ of DSVs for wavenumbers below the peak is also reduced significantly for following and opposing currents. In the case of a cross-current these errors remain significant, (10°-45°) if the current is relatively weak or the wavenumber goes toward $k = 0.5$.

As mentioned in section VI-B, turning the camera in an aerial measurement can reveal the influence of spectral leakage (one could also rotate the resulting images, bearing in mind that this is not in general a lossless operation and might also reduce the field of view). Figure 9 shows the extracted DSVs for a case with the same parameters as in figure 8, but with current and spectrum rotated by 30° (Similar results were obtained for 15-45°).

For the untapered data, we find even stronger mean biases after rotation, especially for a cross-current. Here the DSVs around the spectral peak at $k \approx 1$ drop below $50\,\%$ of the background current, usually an unacceptable level of error. However, the use of a Hann window again mitigates this, to the point where the results of different rotation angles become virtually indistinguishable.

VII. Conclusions

We have investigated biases from spectral leakage in remote sensing of currents from analysis of wave spectra. Apparent, spurious Doppler shifts in the phase velocity are observed even in the absence of a current, and we analyse how these depend on wave spectrum and the properties of the signal processing procedure. Synthetically generated surface elevation data were used to simulate a random sea state adhering to a JONSWAP wave spectrum [30] with a $\cos^2$ directional distribution, resulting in cubes of data (videos). These were subsequently analysed with different methods in common use to extract the Doppler-shift velocities (DSV). Following reference [26], an appropriate measure of random errors and biases are the "Doppler shift resolutions" corresponding to the change in inferred velocity due to a shift of one pixel in wavenumber or frequency.

A comparison of the normalized scalar product approach (e.g. [26]) and a least-squares method for extracting DSV showed that the former is preferable in all cases, and was therefore used for all subsequent analysis herein.

Assuming the simplest case of quiescent water (i.e. no current), a complex interplay is found between wave-spectrum width and peakedness, and the wave-vector and frequency resolution, together affecting the nature and extent of spurious Doppler-shift "measurements". Spectral leakage causes greater problems when the wave spectrum is strongly peaked and highly directional so that areas of the observed frequency-wave vector spectrum which are important to Doppler-shift extraction have very low signal. Conversely, when the angular spread is wide, $\Delta\theta > 60°$ ($\Delta\theta$: full width of angular distribution), spurious DSVs are small, i.e., sub-resolution. For strongly directional spectra $\Delta\theta < 60°$, severe biases emerge, with amplitudes on the order of the group velocity, depending on the JONSWAP peakedness parameter γ. The biases are sensitive to resolution in frequency and wave-number space, and especially in the absence of tapering (see below) poorer resolution rapidly leads to unusable data for narrow and strongly directional wave fields. Biases are most severe at low wavenumbers compared to the spectral peak.

Tapering the video cubes with a 3D Hann window (e.g. [33]) lowers the biases to the velocity resolution level implied by the wavevector and frequency resolutions — $\delta c_{\delta k}$ and $\delta c_{\delta\omega}$ as defined in equation (4) — or even below. Indeed, the effect of ω-resolution is mostly removed for tapered data (note that although biases are now sub-resolution, the resolution itself will eventually be too poor for purpose). This implies that in data acquisition one should prioritize large areas rather than longer time series if spectral leakage is a problem.

The effect of spectral leakage is most pronounced in the k_x and k_y directions in the spectrum, and hence depends on the angle of propagation relative to these. The biases increase towards an angle of $\theta_0 = 45°$ for all wavenumbers outside a small range around the spectral peak $k = k_p$. This dependence on θ_0 is also mostly removed by tapering the data. Clearly the observed current velocity cannot depend on which way the camera is held, meaning that comparison with results when the video is rotated 45° could give a simple indication of the severity of spectral leakage problems.

For the case of a constant background current $\boldsymbol{U}$ with strengths up to $0.15\,c_0(k_p)$ a strong dependence on the angle between the current and the waves is observed. While the magnitudes of the spurious DSVs are mostly beneath the implied velocity resolutions, we find a significant bias in the direction of the DSVs around $k = k_p$ when the waves propagate perpendicular to the current. This is also mitigated by tapering the data, but not removed in the case of a cross current.

A. Recommendations for mitigation

Summarising the outcome of our analysis from a practical viewpoint we offer the following considerations to mitigate the errors and biases related to spectral leakage in remote sensing of currents from observed wave spectra. In the extraction of Doppler shift velocities from the spectrum, the commonly used least-squares method is not recommended except if calculation cost is a severe restriction; a normalized scalar product procedure gives universally better results (other methods are also in use, but were not tested). Tapering the spatio-temporal data with a 3D Hann window greatly reduces the mean and random biases and greatly reduces the dependence these have on spectral shape, spectral resolution, and camera orientation. When errors due to spectral leakage are suspected, rotating the camera (either the actual camera or the resulting images) by a small angle before analysis (we used 30°) and comparing results could reveal whether long range spectral leakage is causing spurious results, because

leakage mainly occurs along the axes of the images. We find that the wavenumber resolution plays a more important role in the DSV biases than frequency resolution. The influence of the latter can be nearly eliminated by tapering the data. Increasing the spatial domain size to improve wavenumber resolution yields the largest improvement and should therefore be prioritized over longer time series if spectral leakage is a concern. The Doppler shift resolutions $\delta c_{\delta\omega}$ and $\delta c_{\delta k}$ defined in equation (4) are useful as conservative measures of errors and biases due to limited resolution and spectral leakage.

VIII. Acknowledgments

The authors would like to thank Drs. Susanne Støle-Hentschel, Luc Lenain and Nick Pizzo for discussions.

Appendix

A. Comparison of window functions

There exists a wide variety of window functions employed in all manners of fields, as discussed in e.g. [33]. The suppression of the long range spectral leakage is the most important beneficial effect of using a window function, but stronger suppression comes at the cost of increasing the short range leakage. For example, the Blackman window has a central lobe that is about 20% wider than that of the Hann window, as can be seen in figure 1. To examine its detrimental effect, the extraction of DSVs has been repeated with a selection of commonly used window functions. As the results are very similar we only show the results for the Hann window

$$w(t) = 0.5 - 0.5\,\cos\left(2\pi\, t/T\right), \tag{17}$$

the approximate Blackman window,

$$w(t) = 0.42 - 0.5\,\cos\left(2\pi\, t/T\right) + 0.08\,\cos\left(4\pi\, t/T\right), \tag{18}$$

and the Kaiser-Bessel window

$$w(t) = \frac{1}{T} I_0\left(b\sqrt{1-(2\pi\, t/T)^2}\right), \tag{19}$$

with I_0 being the zeroth order modified Bessel function of the first kind and b a free parameter controlling the width of the central lobe. In figure 10 the extraced DSVs in terms of their main and random bias are shown. The differences in the results are insignificant, except for the Blackman window showing systematically higher biases due to its wider central lobe.

B. Details of numerical implementation

Here follow further details on the implementation of the NSP method in section III-C.

1) NSP, LS and discretized data: Because of discretization, obtaining the spectral intensity P_i (equation 13) on a cylinder surface needs to be replaced with the spectral intensity in a volume around it, i.e. a cylinder shell, containing a wavenumber bin around k_i:

$$F_i(\mathbf{k},\omega) = \begin{cases} \sqrt{P(\mathbf{k},\omega)}, & \text{if } |k-k_i| \le \tilde{\Delta}k \\ 0, & \text{otherwise} \end{cases}. \tag{20}$$

This also renders the characteristic function G_i (equation (14)) a function of k. The integrals $\langle ... \rangle$ in equation 16 then imply an additional integration over k within the bin $k_i \pm \tilde{\Delta}k$.

The concept of the NSP method stays the same, with two details added: First, since the optimization parameter pair $\tilde{\mathbf{c}}$ is assumed constant within a wavenumber bin, the extracted DSV is a weighted average within that bin, effectively smoothing the function $\tilde{\mathbf{c}}(k)$. This also holds for the LS method, but does not change equation (21), as it only increases the number of triplets $(k_{x,j}, k_{y,j}, \omega_j)$. Second, a new free parameter is introduced with the bin width $2\tilde{\Delta}k$ that needs to be chosen carefully. In this work, we use $\tilde{\Delta}k = 2\delta k$, with $\delta k = 1/L$ the wavenumber resolution, which is a compromise between increased smoothing (too large $\tilde{\Delta}k$) and strong noise, occurring when too few pixels of the spectrum lie within a bin. (One could employ an interpolation scheme to circumvent this; the algorithm used herein simply masks the data, see equation 20)

Since the data is effectively averaged over k with a running average of width $2\tilde{\Delta}k$, the DSVs were extracted such that two consecutive shells have an overlap of $3/4$, i.e. $k_{i+1} - k_i = \delta k$.

2) Width of the characteristic function: As mentioned in section V the characteristic function G (equation 14) used when premultiplying with a Hann window, contains one free parameter that determines its width. The choice of this parameter is somewhat delicate, as too small a value causes single intensity pixels (often outliers) or small high intensity regions to dominate the determination of the best fit. This is especially problematic for small ($k < 1$) wavenumbers, when the spectral leakage from a noise-enhanced pixel near the spectral peak at $k \approx 1$ causes a small high-intensity region on the cylinder shell, whereas the "real" spectral intensity, not originating from spectral leakage, is strongly broadened, thus having a larger total intensity but a smaller maximum intensity. In this case, the algorithm effectively ignores the real spectral intensity and leads to huge biases. On the other hand, too large a value for a also leads to an increased influence of spectral leakage, as a too wide Gaussian is insensitive to shifts in its position. A shift with no, or only small penalty to the overlap with the real spectral intensity, that increases the overlap with intensity from leakage, is therefore more likely, also leading to biases.

To decide on a good compromise we fit the characteristic function to the Fourier transform of a Hann window, with a as a free parameter. The result is $a \approx 1.62\,\delta\omega$. To ensure the width is not too small this value is roughly doubled to $a = 4\,\delta\omega$. (Values for $a/\delta\omega$ between 2 and 6 were tried as well, but the results were most stable between 3 and 5.)

Note, that if spectral leakage occurred only in the ω direction, $a = \delta\omega$ would be the ideal choice. However, as this is not the case, broadening in the ω direction originates not only from leakage in the ω direction, but also from leakage in the k-direction. The steeper the dispersion relation ω_{DR}, the more this effective ω-leakage from k-leakage increases. A possible improvement of the used NSP algorithm would therefore be to use an adaptive a, that increases with $|\partial\omega/\partial k|$. In the interest of limiting the parameter space, it was deemed necessary to stick to a single value for a.

C. Comparison NSP and a basic LS algorithm

Simple least squares based methods have by now been discarded in most applications. However, their low computational cost and ease of implementation are benefits to consider. We therefore repeated the DSV extraction using LS and compare the results and performance. The least squares method used, like the NSP method described in section III-C, first singles out the spectral intensity on a cylinder surface with radius k. We discard data points with an intensity $P < 0.2$ (after normalization) and obtain a list of $(k_{x,j}, k_{y,j}, \omega_j)$. On these, the cost function

$$C(\tilde{\boldsymbol{c}}) = \sum_j (\omega_{DR}(\boldsymbol{k}_j; \tilde{\boldsymbol{c}}) - \omega_j)^2 \tag{21}$$

is minimized to obtain the DSV $\tilde{\boldsymbol{c}}$. Repeating this for a list of wavenumbers k yields the desired value of $\tilde{\boldsymbol{c}}$ for each value of k. As in the NSP method and, the minimization/optimization step is performed using the Nelder-Mead simplex method [35].

We find that the LS method runs significantly faster (up to a factor of 3); clearly the difference in cost will depend on the hardware used as well as the implementation. In terms of accuracy and precision, we find that the LS method performed consistently worse, and never better, than the NSP method. Figure 11 shows an example result for a test case in quiescent water (see table I, case-NSP-LS, for all parameters). As can be seen, the DSVs obtained via the LS method can show both a mean and random bias that exceed the implied velocity resolutions $\delta c_{\delta k}$ and $\delta c_{\delta \omega}$ for most wavenumbers, while the NSP method delivers sub-resolution DSVs for all $k > 1$. It is worth pointing out, that for wavenumbers $k < 1$ the NSP performs worse than the LS method. However, the random bias in that range is so large as to make both methods unusable. Note that a more advanced LS method may perform with similar accuracy and precision, as is indicated in e.g. [10]. This would, presumably, lead to a computational cost similar to that of the NSP method, eliminating the advantage. An iterative LS method has been compared with NSP by Huang et al. (2012). For waves on currents without vertical shear the methods performed similarly.

Data availability

The data that support the findings of this study are available from the authors upon reasonable request.

References

[1] B. K. Smeltzer and S. Å. Ellingsen, *Current mapping from the wave spectrum*. Institution of Engineering and Technology (IET), 2021, ch. 15, pp. 357–378. [Online]. Available: https://arxiv.org/abs/2205.05373

[2] R. H. Stewart and J. W. Joy, "HF radio measurements of surface currents," *Deep-Sea Res.*, vol. 21, pp. 1039–1049, 1974.

[3] E.-C. Ha, "Remote sension of ocean surface current and current shear by HF backscatter radar," Stanford University, Tech. Rep., 1979.

[4] I. R. Young and W. Rosenthal, "A three-dimensional analysis of marine radar images for the determination of ocean wave directionality and surface currents," *J. Geophys. Res.*, vol. 90, pp. 1049–1059, 1985.

[5] D. M. Fernandez, J. F. Vesecky, and C. Teague, "Measurements of upper ocean surface current shear with high-frequency radar," *J. Geophys. Res.*, vol. 101, no. C12, pp. 28,615–28,625, 1996.

[6] K.-W. Gurgel and H.-H. Essen, "On the performance of a shipborne current mapping hf radar," *IEEE journal of Oceanic Engineering*, vol. 25, no. 1, pp. 183–191, 2000.

[7] C. C. Teague, J. F. Vesecky, and Z. R. Hallock, "A comparison of multifrequency HF radar and ADCP measurements of near-surface currents during COPE-3," *IEEE J. Oceanic. Eng.*, vol. 26, pp. 399–405, 2001.

[8] R. Gangeskar, "Ocean current estimated from X-band radar sea surface images," *IEEE Trans. Geosci. Remote Sens.*, vol. 40, pp. 783–792, 2002.

[9] F. Ardhuin, L. Marié, N. Rascle, P. Forget, and A. Roland, "Observation and estimation of Lagrangian, Stokes, and Eulerian currents induced by wind and waves at the sea surface," *Journal of Physical Oceanography*, vol. 39, no. 11, pp. 2820–2838, 2009.

[10] W. Huang and E. Gill, "Surface current measurment under low sea state using dual polarized X-band nautical radar," *IEEE J. Sel. Topics Appl. Earth Observ. in Remote Sens.*, vol. 5, pp. 1868–1873, 2012.

[11] K. Hessner, K. Reichert, J. C. N. Borge, C. L. Stevens, and M. J. Smith, "High-resolution X-Band radar measurements of currents, bathymetry and sea state in highly inhomogeneous coastal areas," *Ocean Dyn.*, vol. 64, pp. 989–998, Jul. 2014.

[12] B. Lund, H. Graber, H. Tamura, C. C. III, and S. Varlamov, "A new technique for the retrieval of near-surface vertical current shear from marine X-band radar images," *J. Geophys. Res.*, vol. 120, pp. 8466–8484, 2015.

[13] W. Huang, R. Carrasco, C. Shen, E. W. Gill, and J. Horstmann, "Surface current measurements using x-band marine radar with vertical polarization," *IEEE Transactions on Geoscience and Remote Sensing*, vol. 54, no. 5, pp. 2988–2997, 2016.

[14] B. Lund, B. K. Haus, J. Horstmann, H. C. Graber, R. Carrasco, N. J. M. Laxague, G. Novelli, C. M. Guigand, and T. M. Özgökmen, "Near-surface current mapping by shipboard marine X-band radar: a validation," *J. Atmos. Oceanic Technol.*, vol. 35, pp. 1077–1090, 2018.

[15] R. Gangeskar, "Verifying high-accuracy ocean surface current measurements by X-band radar for fixed and moving installations," *IEEE Transactions on Geoscience and Remote Sensing*, vol. 56, no. 8, pp. 4845–4855, 2018.

[16] S. Støle-Hentschel, B. K. Smeltzer, and Y. Toledo, "On the measurement of the dispersion relation by a radar and the implication on the current retrieval," 2023, Submitted manuscript. [Online]. Available: https://arxiv.org/abs/2303.12181

[17] J. P. Dugan, H. H. Suzukawa, C. P. Forsyth, and M. S. Farber, "Ocean wave dispersion surface measured with airborne ir imaging system," *IEEE Transactions on Geoscience and Remote Sensing*, vol. 34, no. 5, pp. 1282–1284, 1996.

[18] C. J. Zappa, M. L. Banner, H. Schultz, J. R. Gemmrich, R. P. Morison, D. A. LeBel, and T. Dickey, "An overview of sea state conditions and air-sea fluxes during radyo," *Journal of Geophysical Research: Oceans*, vol. 117, no. C7, 2012.

[19] N. J. M. Laxague, B. K. Haus, D. G. Ortiz-Suslow, C. J. Smith, G. Novelli, H. Dai, T. Özgökmen, and H. C. Graber, "Passive optical sensing of the near-surface wind-driven current profile," *J. Atmos. Oceanic Technol.*, vol. 34, pp. 1097–1111, 2017.

[20] M. Streßer, R. Carrasco, and J. Horstmann, "Video-based estimation of surface currents using a low-cost quadcopter," *IEEE Geoscience and Remote Sensing Letters*, vol. 14, no. 11, pp. 2027–2031, 2017.

[21] J. P. Dugan, C. C. Piotrowski, and J. Z. Williams, "Water depth and surface current retrievals from airborne optical measurements of surface gravity wave dispersion," *J. Geophys. Res.*, vol. 106, pp. 16 903–16 915, 2001.

[22] J. P. Dugan and C. C. Piotrowski, "Surface current measurements using airborne visible image time series," *Remote Sens. Environ.*, vol. 84, pp. 309–319, 2003.

[23] M. Yurovskaya, N. Rascle, V. Kudryavtsev, B. Chapron, L. Marié, and J. Molemaker, "Wave spectrum retrieval from airborne sunglitter images," *Remote sensing of Environment*, vol. 217, pp. 61–71, 2018.

[24] L. Lenain, B. K. Smeltzer, N. Pizzo, M. Freilich, L. Colosi, S. A. Ellingsen, L. Grare, H. Peyriere, and N. M. Statom, "Airborne observations of surface winds, waves and currents from meso to submesoscales," *Geophys. Res. Lett*, vol. 50, p. e2022GL102468, 2023.

[25] J. Campana, E. J. Terrill, and T. de Paolo, "A new inversion method to obtain upper-ocean current-depth profiles using X-band observations of deep water waves," *J. Atmos. Oceanic Technol.*, vol. 34, pp. 957–970, 2017.

[26] B. K. Smeltzer, E. Æsøy, A. Ådnøy, and S. Å. Ellingsen, "An improved method for determining near-surface currents from wave dispersion measurements," *J. Geophys. Res.: Oceans*, vol. 124, pp. 8832–8851, 2019.

[27] C. M. Senet, J. Seeman, and F. Ziemer, "The near-surface current velocity determined from image sequences of the sea surface," *IEEE Trans. Geosci. Remote Sens.*, vol. 39, no. 3, pp. 492–505, 2001.

[28] F. Serafino, C. Lugni, and F. Soldovieri, "A novel strategy for the surface current determination from marine X-band radar data," *IEEE Geosci. Remote Sens. Lett.*, vol. 7, pp. 231–235, 2010.

[29] B. Lund, B. Haus, H. Graber, J. Horstmann, R. Carrasco, G. Novelli, C. Guigand, S. Mehta, N. Laxague, and T. Özgökmen, "Marine x-band radar currents and bathymetry: An argument for a wave number-dependent retrieval method," *Journal of Geophysical Research: Oceans*, vol. 125, no. 2, p. e2019JC015618, 2020.

[30] K. F. Hasselmann, T. P. Barnett, E. Bouws, H. Carlson, D. E. Cartwright, K. Eake, J. Euring, A. Gicnapp, D. Hasselmann, and P. Kruseman, "Measurements of wind-wave growth and swell decay during the joint north sea wave project (JONSWAP)," *Ergänzungsheft zur Deutschen Hydrographischen Zeitschrift, Reihe A*, pp. 1–95, 01 1973.

[31] S. A. Ellingsen and Y. Li, "Approximate dispersion relations for waves on arbitrary shear flows," *J. Geophys. Res.: Oceans*, vol. 122, pp. 9889–9905, 2017.

[32] D. A. Lyon, "The discrete Fourier transform, part 4: spectral leakage," *Journal of object technology*, vol. 8, no. 7, 2009.

[33] A. Nuttall, "Some windows with very good sidelobe behavior," *IEEE Transactions on Acoustics, Speech, and Signal Processing*, vol. 29, no. 1, pp. 84–91, 1981.

[34] H. Socquet-Juglard, K. Dysthe, K. Trulsen, H. E. Krogstad, and J. Liu, "Probability distributions of surface gravity waves during spectral changes," *Journal of Fluid Mechanics*, vol. 542, p. 195–216, 2005.

[35] J. C. Lagarias, J. A. Reeds, M. H. Wright, and P. E. Wright, "Convergence properties of the nelder-mead simplex method in low dimensions," *SIAM J. Optim.*, vol. 9, pp. 112–147, 1998.

[36] L. Lenain, B. K. Smeltzer, N. Pizzo, M. Freilich, L. Colosi, S. A. Ellingsen, L. Grare, H. Peyriere, and N. Statom, "Airborne remote sensing of upper-ocean and surface properties, currents and their gradients from meso to submesoscales," *Geophysical Research Letters*, vol. 50, no. 8, p. e2022GL102468, 2023, e2022GL102468 2022GL102468. [Online]. Available: https://agupubs.onlinelibrary.wiley.com/doi/abs/10.1029/2022GL102468

[37] Y. Goda, *Random seas and design of maritime structures*. World Scientific Publishing Company, 2010, vol. 33.

[38] O. M. Mazzaretto, M. Menéndez, and H. Lobeto, "A global evaluation of the JONSWAP spectra suitability on coastal areas," *Ocean Engn.*, vol. 266, p. 112756, 2022.

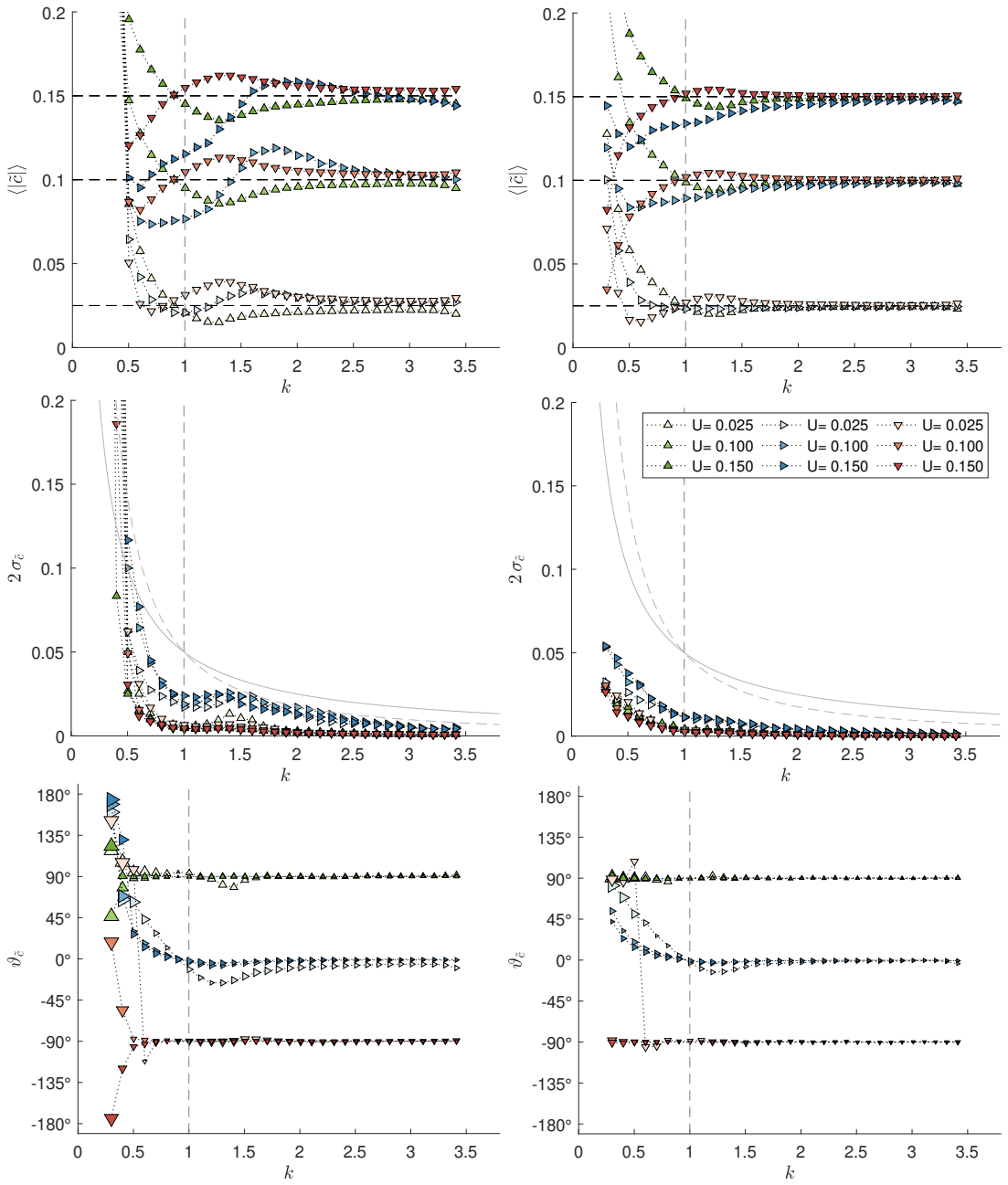

Fig. 8. Same as figure 5 but with parameter set case-U (see table I). The dashed horizontal lines represent the three background velocity values. Deviations from these are spurious. The third row shows the direction $\theta_{\tilde{c}}$ of the average Doppler shift velocity.

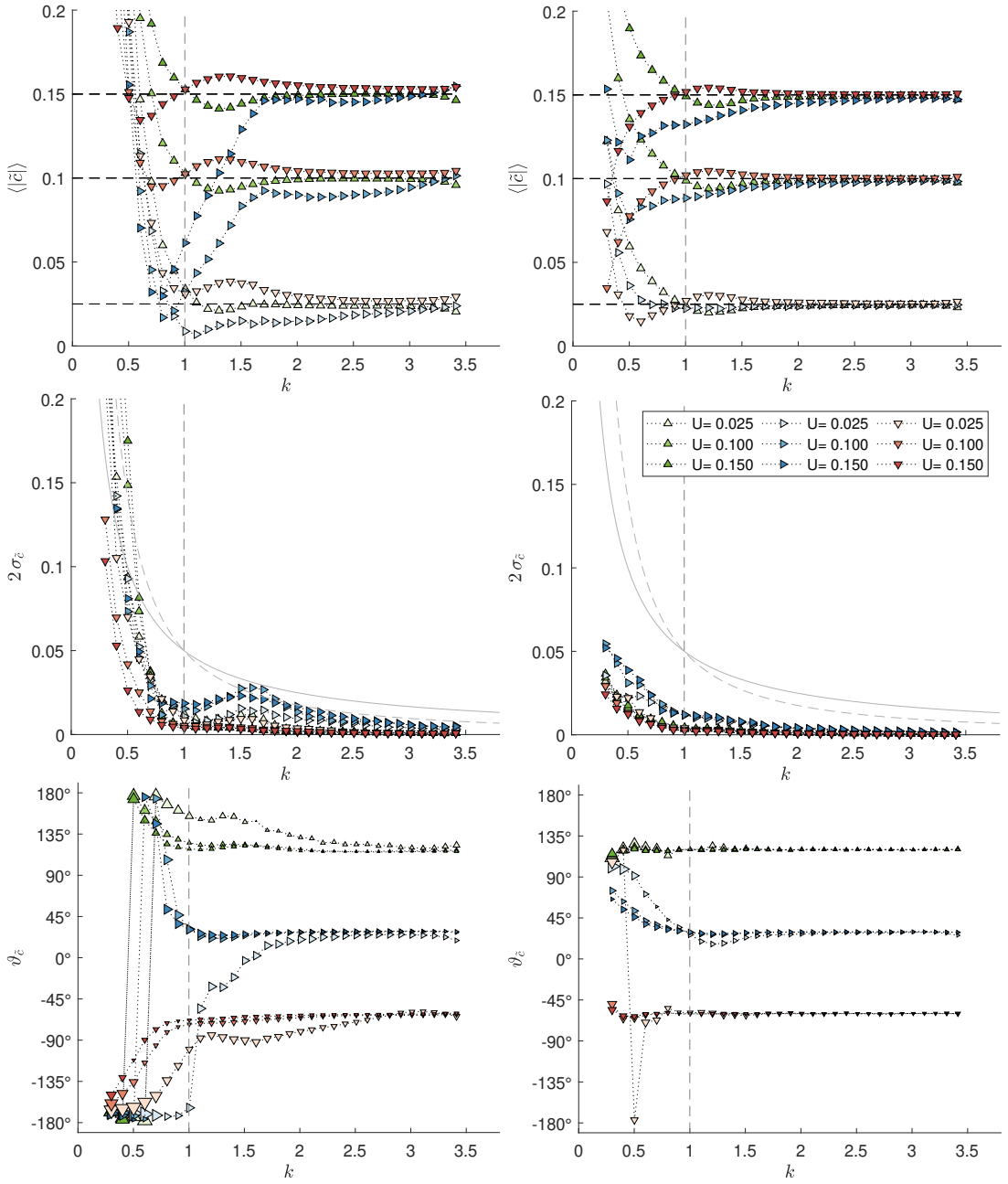

Fig. 9. Same as figure 8 but with a 30° rotated video. Note, how the case of cross currents (blue right facing triangles) result in unusable DSVs $\tilde{\boldsymbol{c}}$ especially around the spectral peak, when the data is untapered. (top left)

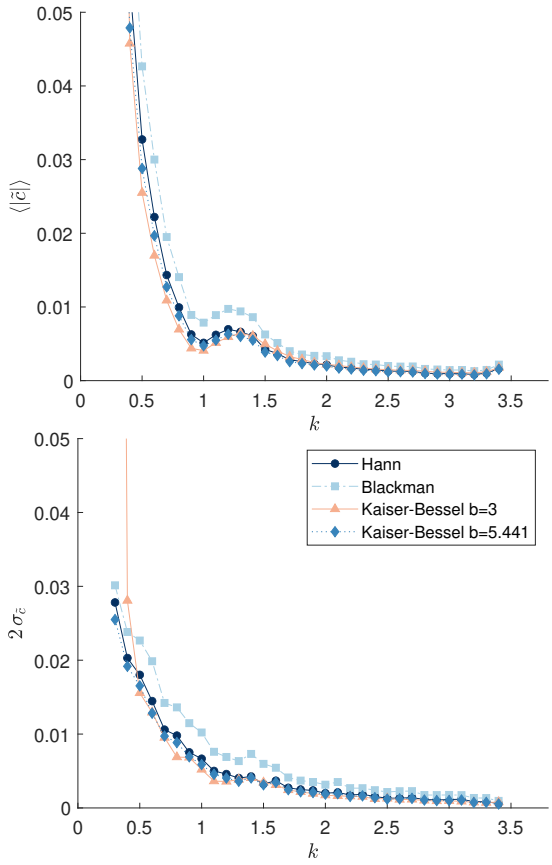

Fig. 10. Doppler shift velocities (DSV) for a normal parameter combination ($\theta_0 = 90°$, $\Delta\theta = 60°$, $\gamma = 3.3$, $L = 10$, $T = 20$, $U = 0$) obtained using the NSP method after tapering the data with different window functions. The top and bottom graph show the DSVs $\tilde{\boldsymbol{c}}$ in terms of the mean (top) and standard deviation (bottom), respectively.

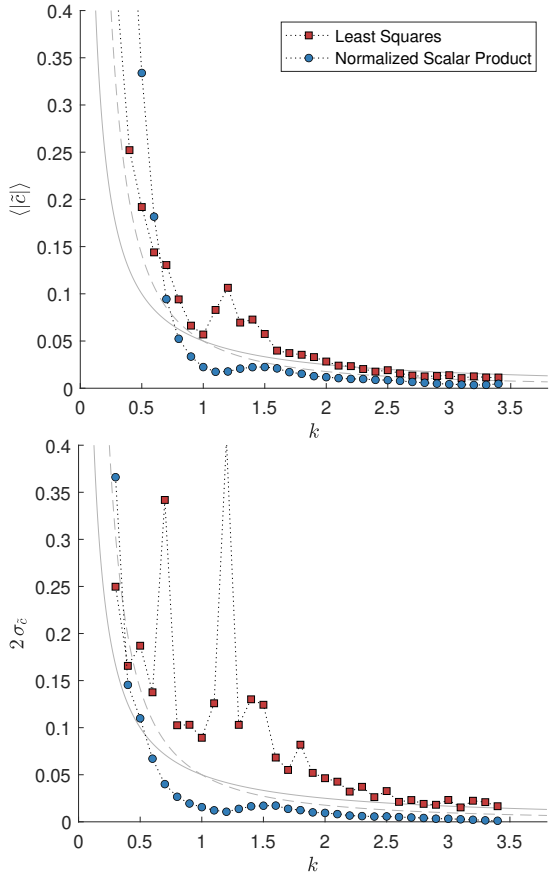

Fig. 11. Doppler shift velocities (DSV) for the parameter set case-NSP-LS (see table I) extracted using the NSP and a least square method. The top and bottom graph show the DSVs $\tilde{\boldsymbol{c}}$ for quiescent water in terms of the mean (top) and standard deviation (bottom). The solid and dashed line correspond to the velocity resolutions implied by frequency and wavenumber resolution, respectively.

Article III

The effect of horizontal shear in extracting near-surface currents from wave data

Stefan Weichert, Benjamin K. Smeltzer and Simen Å. Ellingsen

Submitted to
IEEE Transactions on Geoscience and Remote Sensing

This paper is submitted for publication and is therefore not included.

ISBN 978-82-326-8080-1 (printed ver.)
ISBN 978-82-326-8079-5 (electronic ver.)
ISSN 1503-8181 (printed ver.)
ISSN 2703-8084 (online ver.)

NTNU
Norwegian University of
Science and Technology